Nonlinear quantum optics with Josephson meta-materials

Arpit Ranadive

▶ **To cite this version:**

Arpit Ranadive. Nonlinear quantum optics with Josephson meta-materials. Physics [physics]. Université Grenoble Alpes [2020-..], 2022. English. NNT : 2022GRALY090 . tel-04086842

HAL Id: tel-04086842

https://theses.hal.science/tel-04086842v1

Submitted on 2 May 2023

HAL is a multi-disciplinary open access archive for the deposit and dissemination of scientific research documents, whether they are published or not. The documents may come from teaching and research institutions in France or abroad, or from public or private research centers.

L'archive ouverte pluridisciplinaire **HAL**, est destinée au dépôt et à la diffusion de documents scientifiques de niveau recherche, publiés ou non, émanant des établissements d'enseignement et de recherche français ou étrangers, des laboratoires publics ou privés.

THÈSE

Pour obtenir le grade de

DOCTEUR DE L'UNIVERSITÉ GRENOBLE ALPES

École doctorale : PHYS - Physique
Spécialité : Physique de la Matière Condensée et du Rayonnement
Unité de recherche : Institut Néel

Optique quantique non linéaire avec les méta-matériaux Josephson

Nonlinear quantum optics with Josephson meta-materials

Présentée par :

Arpit RANADIVE

Direction de thèse :

Wiebke GUICHARD PROFESSEUR DES UNIVERSITES, Université Grenoble Alpes	Directrice de thèse
Nicolas ROCH CHARGE DE RECHERCHE, Université Grenoble Alpes	Co-encadrant de thèse

Rapporteurs :

BENJAMIN HUARD
Professeur des Universités, ENS DE LYON
GERHARD KIRCHMAIR
Professeur, Universität Innsbruck

Thèse soutenue publiquement le **7 novembre 2022**, devant le jury composé de :

BENJAMIN HUARD Professeur des Universités, ENS DE LYON	Rapporteur
GERHARD KIRCHMAIR Professeur, Universität Innsbruck	Rapporteur
FRANCK BALESTRO Professeur des Universités, UNIVERSITE GRENOBLE ALPES	Président
JEAN-PHILIPPE POIZAT Directeur de recherche, CNRS DELEGATION ALPES	Examinateur
ARCHANA KAMAL Professeur assistant, UMass Lowell	Examinatrice
MATTHEW BELL Professeur associé, UMass Boston	Examinateur

Nonlinear quantum optics with Josephson metamaterials

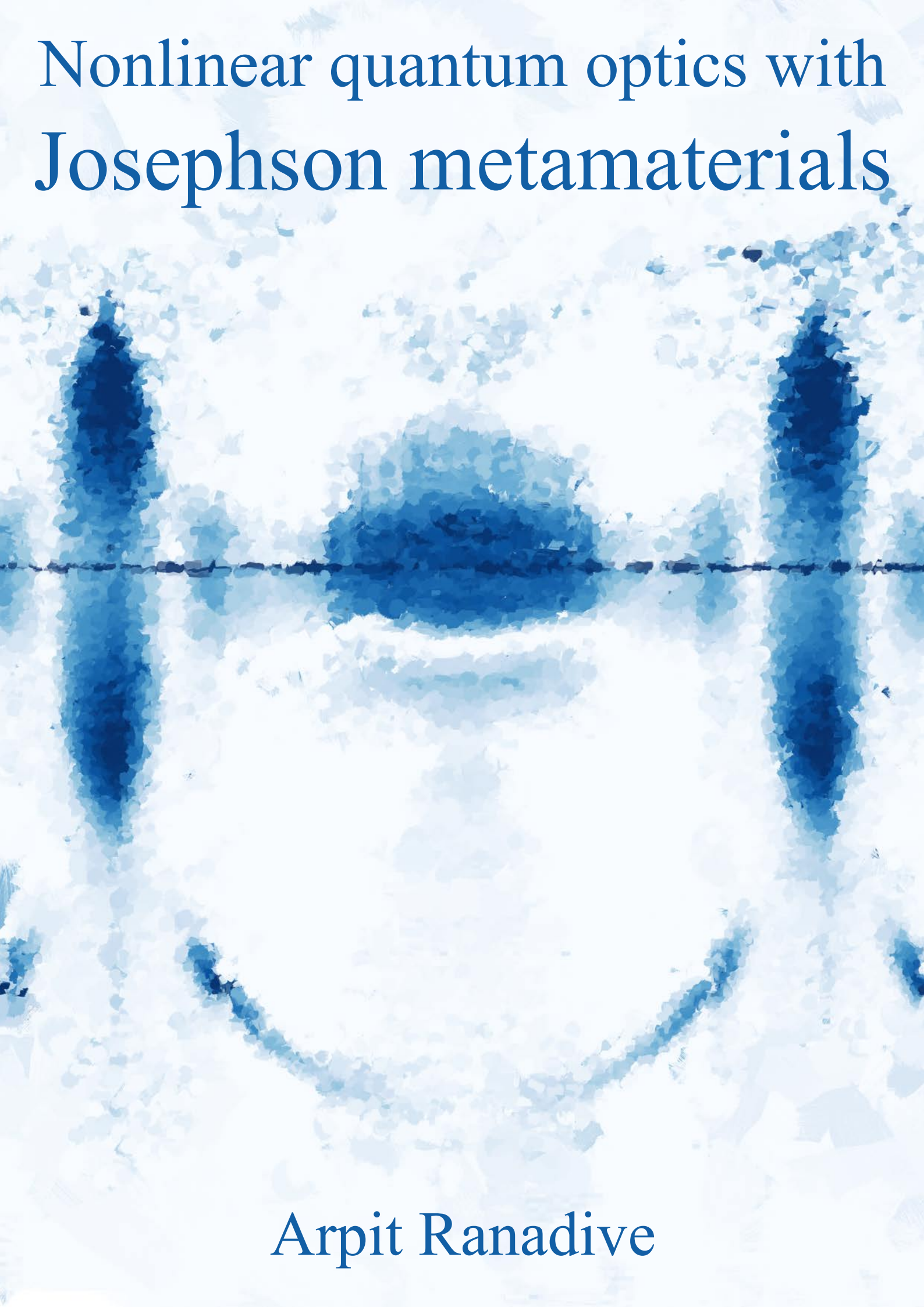

Arpit Ranadive

NONLINEAR QUANTUM OPTICS WITH JOSEPHSON METAMATERIALS

ARPIT RANADIVE

Feb 2023 – v1.0[1]

[1] Latest version available at https://arpitranadive.com/phdthesis

mail@arpitranadive.com

ACKNOWLEDGMENTS

Numerous people have contributed to the success of the works described in this thesis. A few words can not justly describe all the support that I received but I'll do my best to acknowledge their contributions.

I would like to express my deep gratitude to the jury members for taking time from their busy lives to constitute the committee. I thoroughly enjoyed the lively discussion with all of you, learned a lot, and your comments helped in improving the thesis. Thanks a lot for your enthusiastic comments, broad perspective, and interest in this work. Thanks, Dr. Benjamin Huard and Dr. Gerhard Kirchmair for your detailed read and compilation of the thesis report. Dr. Archana Kamal, thanks for your detailed annotations and constructive comments on the manuscript. Thanks to Dr. Matthew Bell, Dr. Jean-Philippe Poizat, and Dr. Franck Balestro for your very interesting questions and comments and enjoyable discussions that they generated.

The work was carried out in Institute Neel, supported by various experimental services and the administration. I would like to thank the members of the nano-fabrication facility, Thierry Crozes, Bruno Fernandez, Jean-François Motte, Gwénaëlle Julie, and Latifa Abbassi for their help in the fabrication of the devices in the clean-room, Laurent Cagnon for support with the ALD setup and Irène Pheng for help with the careful dicing of fragile devices. The mechanical workshop members helped with the design and fabrication of the sample holders, special thanks to Julien Jarreau and Laurent Del-Rey for useful discussions and training on the machines. Eric Eyraud, I can not even imagine using SionludiXL without your help, thanks a lot for always being available for support and help with all the improvements. Special thanks to the members of the liquefier facility for maintaining a steady supply of liquid helium for the cryostat. Thanks, Julien Minet for your continued help with the programming of the RFSoC, squeezing experiment would not have been possible without it. I would like to thank the administrative staff of the institute for all the help, especially Florence Pois and Angélique Simoes for the help with managing the administrative tasks

and finances. I'm very very grateful for all your patience with my beginner French and all your efforts towards meeting me halfway with English.

I have been very fortunate in receiving support and insights from some great collaborators. Thanks to François Lefloch and Julien Renard for being external thesis advisors and bringing in a new perspective on the work. I really enjoyed our numerous discussions. I'm grateful to Peter Leek and James (Oxford), Michael Stern (BIU), Dorian and Vladimir (Neel) for being beta testers of the TWPAs and for a thorough exploration of the devices. I benefited a lot from the insights gained from our discussions. Joe Aumentado and Florent Lecocq, thanks a lot for the SNTJ noise source, and especially all the tips and notes on the noise measurements. Anja Metelmann and Sina, thanks for all your insights on the squeezing experiment, working with you has been an absolute pleasure.

A big thank you to all the past and present superconducting circuiteers for your help with the work and for making life interesting. Martina, working with you has been just amazing and I'm very happy that it still continues. Thanks for all your support, kindness, and encouragement over the years, and thanks for being a great friend, your absence in the lab is indeed felt. Luca, thanks a lot for patiently showing me the ropes when I arrived and welcoming me to the TWPA project, I'm very grateful to call you a friend. I would wish you luck with the SW but I know you don't need it. Katia, your optimism and positivity never ceased to amaze me, thanks for being a great friend and for your support in my early Grenoble days. Giulio, Gwen, and Nicolo thanks for all the fun memories, I look forward to making many more. Guilliam, it has been a pleasure, I'm happy that you are on the TWPA side now. Bekim, your calm seems exactly the opposite of le chef, looking forward to working closely with you. Anuj, thanks for all the charged discussions. Vlad, only you can top your adventure stories, life will never be humdrum for you. Seb, I could always count on you for something unexpected. Jovian, thanks for all the fun hangouts, good luck with pétanque.

Thanks to QuMaC friends and Vijay for introducing me to the curious world of superconducting circuits.

Thanks to the PIs of the superconducting circuits group, Cécile Naud, Wiebke Guichard, Olivier Buisson, and Nicolas Roch for graciously accepting me to the group. Wiebke, thank you for always following up on the thesis progress despite the difficulties. Olivier, thanks for all the amazing discussions on work but also on life, music, and politics. And Nico, it's hard to restrict to only a few sentences to express all the gratitude I feel towards you, but let me try anyway. Throughout the years you gave me a perfect environment to grow as a physicist, always being there when I need it while giving me ample freedom to explore on my own. I've learned a lot from you, not just about physics but also about how to be a well-rounded experimentalist. Anyone who has worked with you will completely agree that you set the standard as a scientific supervisor and manager.

Finally, I would like to thank my whole family, and friends for their unwavering support through the years. To my parents, thanks for always being supportive while demanding and motivating me. Thanks to my brother for always being in my corner. Thanks to my friends (who have become my family) RMS, SB, PK, AS, RP, PN, and NRJ for always being there.

CONTENTS

Back to contents

Back to contents

Part I

JOSEPHSON METAMATERIALS

1 INTRODUCTION

1.1 SUPERCONDUCTING META-MATERIALS

Meta-materials are artificially designed materials exhibiting properties not available in natural materials. Such feat is achieved by engineering the constituting elements of the meta-material at sub-wavelength scales, enabling unique interactions of matter with electromagnetic waves or coupling modes of electromagnetic waves. Some important novel optics phenomenons include negative index of refraction, cloaking, and super-resolution imaging [1]. The study of meta-materials [2, 3] has recently generated large interest in the framework of quantum technologies due to wide range of direct applications, e.g. exploration of novel quantum optics phenomena [4–7], non-destructive quantum sensing [8], quantum limited amplification [9–11] or quantum information processing [12–14]. Due to a wide range of applications, superconducting metamaterials realizations have been demonstrated from DC to the ultra-violet frequencies [15]; however, we will focus our discussions on microwave frequencies in the few GHz range.

In contrast to their normal metal and semiconducting counterparts, superconducting metamaterials offer some unique advantages. Most relevant of these for our discussions are low losses, flux quantization, and Josephson effects [1, 16]. Introducing SQUID (superconducting quantum interference device) structures in the meta-materials allow in-situ tuning of their properties while introducing extraordinarily strong and tunable nonlinearities [3]. Such meta-materials are theoretically investigated and experimentally demonstrated to exhibit exciting new phenomena in the classical and quantum regimes [17].

Josephson meta-materials are constructed by embedding an array of Josephson junctions or loops containing Josephson junctions in a transmission line. A composite structure of more than two Josephson junctions in a loop, an asymmetric SQUID, can be designed to exact more control over the nonlinearities of the meta-material [18, 19]. Initial implementation of such elements

was demonstrated to construct three-wave mixing devices [19, 20]. However, by carefully designing these devices, the sign of the nonlinearities can also be controlled by applying a magnetic field to the device. The work discussed in this thesis was started with the aim of developing Josephson junction based metamaterials with in-situ tunability of second-order and third-order (Kerr) nonlinearities, and demonstrating their efficacy as a versatile platform for microwave quantum optics experiments and applications.

The metamaterial, fabricated in transmission geometry, can be used as a broadband and low noise amplifier out of the box, and hence this use case is naturally well suited for initial demonstration of its efficacy.

1.2 TRAVELING WAVE PARAMETRIC AMPLIFICATION

Recently, low noise parametric amplifiers underwent an enormous development, especially due to their remarkable impact in the field of superconducting quantum computation and information technologies [21]. Resonant parametric amplifiers based on Josephson junctions embedded in microwave resonators (JPAs) [22, 23] provide quantum-limited amplification [24–27] and are widely used for quantum-noise limited microwave readout [28]. The resonant nature of JPAs sets a limit on their bandwidth and hence on their applications. Recently, this limitation has been overcome by traveling wave parametric amplifiers (TWPAs). These devices consist of non-resonant nonlinear transmission lines exhibiting amplification bandwidth up to a few GHz [21]. The nonlinearity required for parametric coupling of modes in these devices is provided either by the kinetic inductance of superconducting material (KTWPAs) [29] or by a Josephson meta-material (JTWPAs) [9–11]. TWPAs are very appealing tools for a variety of applications dealing with broadband quantum-noise limited amplification [30], ranging from the multiplexed readout of solid-state qubits [31–33] to microwave kinetic inductance detectors [34] and dark matter detectors [35] [36] for astrophysics, and microwave photonics experiments [13].

Amplification in TWPAs is implemented with a wave-mixing process arising from a coupling between traveling modes in the nonlinear meta-material: the medium is excited with a strong

Back to contents

pump field at frequency ω_p, causing the amplification of a weaker signal field at frequency ω_s, and the creation of an idler field, at frequency ω_i [37]. Depending on the order of the nonlinearity, the nonlinear process can be either a three-wave mixing process, involving three photons ($\hbar\omega_p = \hbar\omega_s + \hbar\omega_i$), or a four-wave mixing process, involving four photons ($2\hbar\omega_p = \hbar\omega_s + \hbar\omega_i$). Both these processes require specific phase-matching conditions, which have been realized so far by employing rather complicated dispersion engineering of the device operating in the microwave domain. In the case of three-wave mixing TWPAs, implementation of dispersion engineering is required to suppress undesired second-order nonlinear processes, which would otherwise dominate over the parametric amplification process[38]. And in the case of four-wave mixing TWPAs, dispersion engineering is implemented to maintain the phase-matching condition between pump, signal, and idler modes across the nonlinear metamaterial, that would otherwise be degraded due to third-order phase modulation processes [9–11, 29]. In the TWPA devices demonstrated so far [9, 11, 29, 38], an asymptote in the dispersion is engineered either by using a photonic-crystal like approach (a photonic gap is opened in the dispersion by periodically modulating the transmission line [11, 29, 38]) or by using a resonant phase matching approach (a stop band gap is opened in the dispersion by introducing resonant elements in the transmission line [9, 10, 39]).

The dispersion-engineered TWPAs suffer from two major disadvantages. First, the presence of a gap in the dispersion typically produces a discontinuous amplification band with significant ripples in the gain profile caused by impedance mismatch [9, 11, 29]. And second, the dispersion engineering method only guarantees the optimal amplification conditions when the TWPA is pumped at a fixed design frequency [9, 11, 29, 38], making the amplification band fixed by design.

As a first use case of the Josephson meta-material, we demonstrate a four-wave mixing TWPA with a novel phase-matching technique based on the sign reversal of the third-order (Kerr) nonlinearity and with no need for dispersion engineering [18]. Due to the absence of any dispersion engineering, the metamaterial doesn't have gaps in the transmission and a nearly flat impedance profile across the amplification band, which can significantly reduce the gain ripples. The sign reversal of

Back to contents

Kerr nonlinearity is not frequency-dependent; hence the phase-matching mechanism functions across a wide range of pump frequencies. And by changing the pump frequency, the amplification band can be dynamically tuned in situ.

The meta-material, operated as reversed Kerr amplifier, exhibits up to 4 GHz (fixed) combined bandwidth, 8 GHz in-situ tunability of the amplification band (by changing the pump frequency), -98 dBm saturation (1 dB compression point) around 20 dB gain and added noise near the standard quantum limit.

These performance metrics serve as a qualifier of the efficacy of the nonlinear meta-materials constructed from Josephson junctions. To demonstrate their versatility, and further emphasize their potential in the general framework of nonlinear microwave quantum optics, in the next experiments, we investigated the generation of broadband entanglement generation using a driven(pumped) meta-material.

1.3 BROADBAND ENTANGLEMENT GENERATION

Josephson meta-materials can be efficiently deployed to generate quantum (non-classical) states of microwave radiation. These non-classical states of light have emerged as useful tools for enhancing precision measurements. A broadband source of non-classical illumination in microwave finds a wide array of application ranging from potential novel implementations for quantum sensing [40, 41], quantum enhanced detection [42], quantum teleportation with propagating waves [43] to emerging field of quantum information with continuous variables [44–46].

Two-mode squeezing in superconducting circuits has been demonstrated in resonant Josephson parametric amplifiers [47–54], semi infinite transmission lines via Dynamical Casimir Effect [55–57] and surface acoustic wave hybrid systems [58]. The use of broadband meta-materials as a source of entanglement and two-mode squeezing would bring the advantage of large instantaneous bandwidth and customizable nonlinearities, with potential novel applications for quantum sensing [40, 41], quantum-enhanced detection [42], quantum teleportation with propagating waves [43] and quantum information with continu-

Back to contents

ous variables [44–46].

Two key challenges in using the broadband meta-materials are: the presence of loss [59–61] and the activation of spurious nonlinear processes, such as harmonics [39] and frequency up-conversion [62]. For the initial proof-of-principle demonstration, we reduced the length of the meta-material to mitigate losses. With such an optimized device operated in a four-wave mixing regime, we observed two-mode squeezing generation in the meta-material between 1.5 and 2.1 dB for signal and idler modes separated by up to 400 MHz.

These findings experimentally demonstrate the vast potential of Josephson junction based nonlinear meta-materials in the framework of microwave quantum optics.

1.4 SUMMARY OF THE THESIS

The thesis is divided into three parts; the first part, chapters 1 to 3 deals with the introduction of Josephson junction based meta-materials, optimization of the nonlinearity, and their fabrication. In the second part, chapters 4 to 6, we discuss the efficacy of such meta-materials by demonstrating a use case as a traveling wave amplifier with a novel phase-matching technique involving sign reversal of Kerr nonlinearity. And finally, in chapters 7 and 8, we further highlight the versatility of these meta-materials by demonstrating the generation of two-mode squeezing.

1.4.1 *Overview*

In chapter 2, we describe how different kinds of tunable nonlinear elements can be constructed utilizing the Josephson effect and then used as building blocks to design traveling wave nonlinear metamaterials.

In chapter 3, we discuss the details of the fabrication process, design choices, and relevant tricks used for good yield of devices, followed by the exact recipes.

Chapter 4 introduces traveling wave parametric amplification. We start the discussion with the quantum limit of noise added by the amplifier in non-degenerate mode of operation, introduce the semi-classical framework for quantifying traveling

Back to contents

wave parametric amplification in Josephson metamaterials and pre-existing approaches to the phase-matching problem, and then finally discuss utilization of the in-situ Kerr reversal for phase matching.

In chapter 5, we start with the description of the measurement setup, discuss characterization of the device in linear regime, build a realistic model for gain simulation, followed by a discussion on the amplification performance of the device.

In chapter 6, we discuss the measurement of noise added by the reversed Kerr TWPA along with a theoretical model to describe its origins. We also present the noise performance of the whole measurement system, as this is the most relevant figure of merit for typical users, which depends upon both noise and gain performance of the amplifier.

We start the discussion in chapter 7 with squeezing of light, the potential of Josephson junction based nonlinear meta-material for generation of broadband two-mode squeezed state of microwave radiation, and finally describe a simple theoretical description for the same.

In chapter 8 we start with the description of an optimized Josephson meta-material device designed to utilize four-wave mixing for quantum illumination, then present a broadband time-resolved measurement setup, along with its calibration, used for simultaneous measurement of the two-mode entangled microwave radiation generated by such device; followed by a discussion on the measurements, elaborating on the quantification of entanglement and the stability of entanglement generation.

And finally, in chapter 9, we discuss the key conclusions of the discussed results followed by prospectives along with some of the ongoing efforts in the group to better understand the nonlinear physics at the heart of these devices, exploring novel applications and improvement of the device performances in the aforementioned demonstrations.

1.4.2 *Key results presented in the thesis*

We discuss two experiments in the thesis, first dealing with the use case of Josephson meta-material as a TWPA with a novel

Back to contents

phase-matching technique involving sign reversal of Kerr nonlinearity [63]. The metamaterial operated as reversed Kerr traveling wave amplifier exhibits a combined bandwidth of up to 4 GHz, in situ tunability of the amplification band up to 8 GHz, -98 dBm saturation (1 dB compression point) around 20 dB gain, and input-referred added noise near the standard quantum limit. In contrast with the previously demonstrated TWPAs, the absence of gaps in transmission can provide a nearly continuous amplification band with significantly lower gain ripples. It also provides in-situ tunability of the amplification band over an unprecedented range by simply changing the pump frequency (gain larger than 15 dB is observed in the entire 4-12 GHz range by pumping between 6-10 GHz); a significant advantage with respect to the previous state of the art TWPAs, where the pump frequency is fixed by dispersion engineering.

And the second experiment demonstrates the generation and observation of two-mode squeezing in Josephson meta-materials [64]. With a meta-material optimized for the experiment, we observed broadband entanglement generation between two modes separated by up to 400 MHz by measuring logarithmic negativity between 0.27 and 0.51 and collective quadrature squeezing below the vacuum limit between 1.5 and 2.1 dB.

1.4.3 *Experiments, author contributions and publications*[1]

The cryostat, a dilution refrigerator, used to perform the experiments discussed in the thesis, was fabricated in the cryogenic workshop of Institute Neel. This cryostat was installed in the lab by Nicolas Roch (thesis supervisor) with the help of Eric Eyraud. The microwave and DC cables were installed in the cryostat by thesis author and Martina Esposito with the help of Nicolas Roch. The microwave switches and their controller was installed by the author with the help of Martina Esposito and Nicolas Roch. The FPGA module consisting of Xilinx RFSoC platform at the heart of the measurement setup for the squeezing experiment was designed and fabricated at the electronics workshop at Institute Neel by Julien Minet with the help of Nicolas Roch and contributions from the author and Sebastien Leger.

[1] In this section, author refers to the thesis author.

Back to contents

The work discussed in the thesis led to two publications. The first article describes the tunable metamaterial and its use case as a near quantum-limited traveling wave parametric amplifier, appeared in Nature Communications 13 (2022) [65]. The experiment was conceptualized by the author of the thesis with Nicolas Roch and Luca Planat. The devices were fabricated (in the clean room facility of Institute Neel) and measured by the author with the help of Martina Esposito. The data analysis and result interpretation was carried out by the author with the help of Martina Esposito, Luca Planat, and Nicolas Roch. The instrumentation control (drivers and scripts) was implemented by the author and Martina Esposito with the help of Luca Planat and Nicolas Roch. The thermal noise source used for the calibration of amplifiers was designed and installed by the author with the help of Martina Esposito and Nicolas Roch.

A follow-up article to further emphasize the potential of the presented meta-material in the general framework of nonlinear microwave quantum optics, describing the generation of two-mode entanglement, appeared in Physical Review Letters 128 (2022). The experiment was conceptualized by Martina Esposito and Nicolas Roch with contributions from the author, Luca Planat, and Vincent Jouanny. The devices were fabricated (in the clean room facility of Institute Neel) by the author and Martina Esposito. The data analysis and result interpretation was carried out by the author and Martina Esposito with the help of Luca Planat and Nicolas Roch. The instrumentation for the RFSoC module (drivers, scripts, and UI) was implemented by the author and Martina Esposito with the help of Nicolas Roch.

Apart from the aforementioned two publications, the author contributed to four publications in the capacity of second author and to two publications in the capacity of contributing author. These publications include an invited prospective on traveling wave parametric amplifiers appeared in Applied Physics Letters 119 (2021) [30], photonic-crystal (dispersion engineered) Josephson traveling-wave parametric amplifier appeared in Physical Review X 10 (2020) [11], a gate-tunable graphene Josephson parametric amplifier (under review, 2022) [66], exploration of mesoscopic thermodynamics in mechanical oscillators (in preparation, 2022). Recently, traveling wave parametric amplifiers have been identified as convenient tools for increasing the ef-

Back to contents

ficiency of dark matter detection experiments, and the TWPA group in Grenoble is collaborating and providing them to astrophysics researchers across Europe. The author contributed to the integration of TWPA in an experiment involving a haloscope amplification chain (in review, 2022) [67], and to the integration of the TWPA in a simulation of dielectric axion haloscopes appeared in Journal of Cosmology and Astroparticle Physics (2021) [68]. In addition, the TWPA group in Grenoble is collaborating and has provided devices across the globe to researchers working on quantum sciences and quantum computation/information technologies. These multifaceted collaborations highlight the importance of nonlinear meta-materials in state-of-the-art microwave experiments.

Back to contents

2

DESIGNING NONLINEARITY

The versatility of the engineered nonlinear meta-materials depends upon careful selection of the nonlinear elements used as building blocks. Ideally, these building blocks should present a wide range of easily tunable properties and very low loss. Josephson junctions are a prime candidate for constructing nonlinear devices as they offer easy engineering of nonlinear properties with potentially lossless performance. In recent decades, superconducting circuits with Josephson junctions have been identified and very widely adapted as building blocks for quantum processors for the same reason.

In this chapter, we describe how different kinds of tunable nonlinear elements can be constructed utilizing the Josephson effect and then used as building blocks to design traveling wave nonlinear metamaterials.

2.1 THE NON-LINEAR ELEMENT

The Josephson effect, a phenomenon of supercurrent, is observed at weak electrical contact between two superconductors, and is a direct consequence of the quantum coherence of the superconducting condensate [69]. A Josephson junction is a device that exhibits the Josephson effect, and can be constructed with various weak links, for example, insulators, normal metals, or small points of contact. For the works discussed in this thesis, the Josephson junctions were constructed by sandwiching a thin layer of insulating barrier between two superconductors, fabrication of these devices is discussed in chapter 3.

The supercurrent flowing through the Josephson junction can be described by the current phase relation,

$$I = I_c \sin(\phi), \tag{2.1}$$

where I_c is the critical current of the junction, and ϕ is the phase difference between Ginzburg-Landau order parameters of

the two superconducting islands making the Josephson junction.

This behavior of the Josephson junction can also be modeled as a nonlinear inductor with a phase-dependent inductance,

$$L(\phi) = \frac{\phi_0}{I_c \cos(\phi)} \qquad ; \qquad \phi_0 = \frac{\hbar}{2e}. \tag{2.2}$$

This nonlinear inductor can be used to construct a wide range of devices, including nonlinear oscillators and nonlinear transmission lines.

2.2 IN-SITU TUNABILITY

A superconducting quantum interference device (SQUID) is constructed by introducing one or more Josephson junctions in a loop. Initially, these devices were developed as very sensitive magnetometers, which are extensively used these days for various applications [70].

In the context of circuit quantum electrodynamics (cQED), SQUIDs are commonly used as nonlinear inductors offering in-situ tunability of the nonlinearity by applying a magnetic field to the device. Consider two Josephson junctions in a loop, as depicted in Fig. 2.1, placed in magnetic field. Denoting the phase difference across the small junction as ϕ and using the flux quantization for the loop we get,

$$\phi_L = \phi - \phi_{ext}, \qquad ; \qquad \phi_{ext} = \frac{2\pi\Phi_{ext}}{\Phi_0} \tag{2.3}$$

where ϕ_L is the phase difference across the large junctions, and ϕ_{ext} is the reduced external flux due to the applied magnetic flux (Φ_{ext}) on the device. The current phase relation for the device under a magnetic field can be expressed as,

$$I(\phi) = r I_0 \sin\phi + I_0 \sin(\phi - \phi_{ext}), \tag{2.4}$$

where I_0 is the large junction critical current and $r < 1$ is the ratio between critical currents of the small and large junction. (The junctions referred to as large have a larger cross-section and hence, higher critical current compared to smaller junctions.)

Back to contents

We can perform a Taylor expansion about a flux ϕ^* at steady state, i.e $I(\phi^*) = 0$,

$$\frac{I(\phi^* + \phi)}{I_o} = \frac{dI}{d\phi}\Big|_{\phi^*}\phi + \frac{1}{2}\frac{d^2I}{d\phi^2}\Big|_{\phi^*}\phi^2 + \frac{1}{6}\frac{d^3I}{d\phi^3}\Big|_{\phi^*}\phi^3 + \dots \quad (2.5)$$

We then obtain the following expression,

$$\frac{I(\phi^* + \phi)}{I_o} \approx \widetilde{\alpha}\,\phi - \widetilde{\gamma}\phi^3 + \dots \quad (2.6)$$

where,

$$\widetilde{\alpha} = r\cos\phi^* + \cos(\phi^* - \phi_{ext}) \quad , \quad \widetilde{\gamma} = \frac{1}{6}[r\cos\phi^* + \sin(\phi^* - \phi_{ext})]. \quad (2.7)$$

The nonlinear coefficient $\widetilde{\gamma}$ in the above equation depends on the magnetic flux applied to the loop, introducing the possibility of its in-situ tuning. It should be noted that for a SQUID, only odd terms in the nonlinear expansion of the current phase relation are non-zero, irrespective of the critical current of the two Josephson junctions.

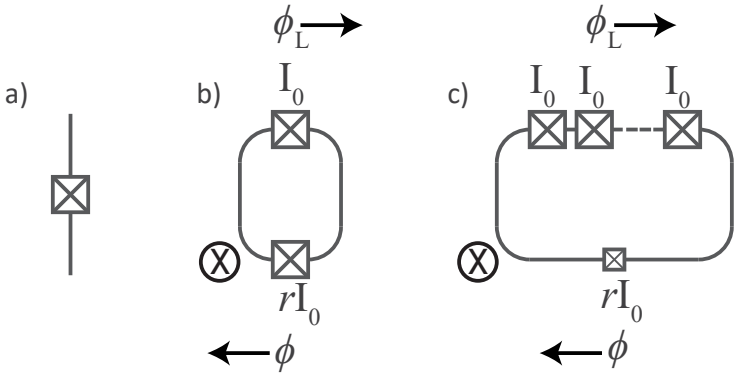

Figure 2.1: a) Circuit symbol for the Josephson junction. b) Schematic for an asymmetric SQUID. c) Schematic for a SNAIL element with one small and n large junctions.

2.3 CONTROLLING NON-LINEARITIES

A composite structure of more than two Josephson junctions in a loop can be designed to exact more control over the nonlinearities of the constructed device [18, 19]. Initial implementation of

Back to contents

such elements was demonstrated to construct three-wave mixing devices [19, 20]. However, by carefully designing these devices, the sign of the nonlinearities can also be controlled by applying a magnetic field to the device.

Consider a loop containing one low and n high critical current Josephson junctions, as depicted in Fig. 2.1, placed in a magnetic field. Denoting the phase difference across the small junction as ϕ and using the flux quantization for the loop we get,

$$\phi_L = \frac{\phi - \phi_{\text{ext}}}{n}, \tag{2.8}$$

where ϕ_L is the phase difference across one large junction, and ϕ_{ext} is the reduced external flux due to the applied magnetic flux (Φ_{ext}) on the device. This simplistic flux quantization is valid when the charging energy of the islands between Josephson junctions can be ignored in comparison to the Josephson energy; i.e. $E_J \gg E_C$ for the junctions, with, $E_J = \Phi_o I_c / 2\pi$, and $E_C = e^2/2C_J$, where C_J is the Josephson capacitance. The current phase relation for the device under a magnetic field can then be expressed as,

$$I(\phi) = rI_o \sin\phi + I_o \sin\left(\frac{\phi - \phi_{ext}}{n}\right), \tag{2.9}$$

where I_o is the large junction critical current and $r < 1$ is the ratio between critical currents of the small and large junction. We can perform a Taylor expansion about a flux ϕ^* at steady state, i.e $I(\phi^*) = 0$,

$$\frac{I(\phi^* + \phi)}{I_o} = \frac{dI}{d\phi}\Big|_{\phi^*}\phi + \frac{1}{2}\frac{d^2I}{d\phi^2}\Big|_{\phi^*}\phi^2 + \frac{1}{6}\frac{d^3I}{d\phi^3}\Big|_{\phi^*}\phi^3 + \dots \tag{2.10}$$

We then obtain the following expression,

$$\frac{I(\phi^* + \phi)}{I_o} \approx \widetilde{\alpha}\,\phi - \widetilde{\beta}\phi^2 - \widetilde{\gamma}\phi^3 + \dots \tag{2.11}$$

where,

Back to contents

$$\begin{aligned}\widetilde{\alpha} &= r\cos\phi^* + \frac{1}{n}\cos\left(\frac{\phi^* - \phi_{\text{ext}}}{n}\right),\\ \widetilde{\beta} &= \frac{1}{2}\left[r\sin\phi^* + \frac{1}{n^2}\sin\left(\frac{\phi^* - \varphi_{\text{ext}}}{n}\right)\right],\\ \widetilde{\gamma} &= \frac{1}{6}\left[r\cos\phi^* + \frac{1}{n^3}\sin\left(\frac{\phi^* - \phi_{\text{ext}}}{n}\right)\right].\end{aligned} \tag{2.12}$$

In practice, the value of ϕ^* can be computed by numerically solving for the roots of the steady-state equation, $I(\phi^*) = 0$. In terms of coupling rates g_3 and g_4, for three-wave and four-wave mixing interactions when embedded in a transmission line,

$$I(\phi) \approx \frac{\Phi_o}{2\pi L}\phi - 3\Phi_o\sqrt{\frac{R_Q}{\pi^3 Z^3}}g_3\phi^2 - 4\Phi_o\frac{R_Q}{\pi^2 Z^2}g_4\phi^3 + \ldots, \tag{2.13}$$

where, Φ_o the magnetic flux quantum, $R_Q = h/4e^2$, Z (defined as $\sqrt{L/C_g}$) is the characteristic impedance of the transmission line, with C_g the ground capacitance per unit cell and L the effective flux-tunable inductance of the element given as,

$$L = \frac{\Phi_o}{2\pi I_o \widetilde{\alpha}} \tag{2.14}$$

and,

$$\hbar g_3 = \frac{\widetilde{\beta}}{3\widetilde{\alpha}}\sqrt{E_C\hbar\omega_o}, \qquad \hbar g_4 = \frac{\widetilde{\gamma}}{2\widetilde{\alpha}}E_C. \tag{2.15}$$

A similar element, exhibiting even order ($\chi^{(2)}$) nonlinearities and sign reversal of Kerr nonlinearity, can also be constructed using a loop containing a Josephson junction along with a linear inductor [71].

2.4 TRAVELING WAVE META-MATERIAL

The versatile element described in the previous section is commonly known as superconducting nonlinear asymmetric inductive element (SNAIL) in the superconducting circuits community.

Back to contents

One of its simple implementations contains three large Josephson junctions in one arm and one small Josephson junction in the second arm (see chapter 3 for fabrication details). Traveling wave nonlinear meta-materials can be constructed by embedding these nonlinear elements into a transmission line. A unique aspect of these meta-materials constructed for microwave photonics is that the wavelength of the traveling wave in the medium is much larger ($\approx$ 100 times) than the footprint of a unit cell. This enables engineering the dispersion of waves in the medium and introduce optimizations at sub-wavelength scales.

The circuit schematic of the SNAIL-based four-wave mixing nonlinear meta-material is depicted in Fig. 2.2. A key challenge to fabrication of such transmission lines is realizing high ground capacitance (C_g), needed to match the impedance of the transmission line to the 50Ω microwave environment. To fabricate these ground capacitors, we use the top ground technique previously developed at the institute for easily customizable fabrication of nonlinear transmission lines [72]. This technique involves deposition of a thin dielectric on top of the Josephson junction, followed by deposition of metallic ground. Thus, a parallel plate capacitor is formed between the electrode of the Josephson junction and the top metal layer (see chapter 3 for detailed description). This capacitance can be tuned by changing the thickness of the dielectric or by adding capacitor pads to the transmission line along with Josephson junctions. For the optimized SNAIL parameters, the junction area alone was not sufficient to form desired capacitance, and capacitive fins were added to the device to ensure impedance matching.

2.5 OPTIMIZING NON-LINEARITY

Optimizing Gradients and Sign Inversion

The two leading order nonlinear coupling rates expressed in Eq. 2.12 as g_3 and g_4 can be utilized for engineering three-wave mixing and four-wave mixing interactions, respectively. Their behavior as a function of applied magnetic flux can be tuned using the ratio of critical currents (r). Fig. 2.3 depicts second order (g_3) and third order (g_4) non-linearities as function of external flux for various values of critical current ratio.

Back to contents

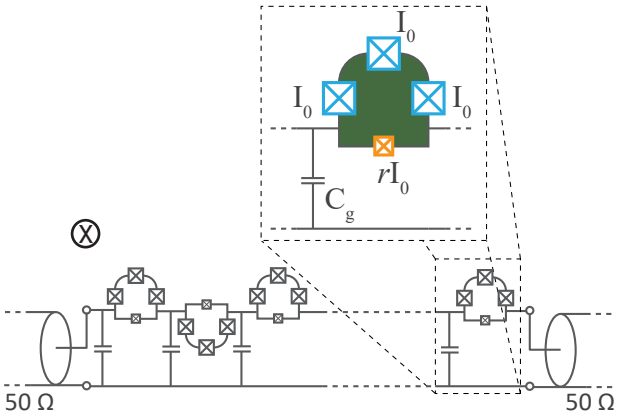

Figure 2.2: A circuit schematic of the four-wave mixing non-linear meta-material. I_o is the critical current of the large junction, rI_o is the critical current of the small junction and C_g is the ground capacitance per unit cell. A global magnetic field is applied to the device, hence, the alternating loop geometry results in an alternating magnetic flux polarity.

Depending upon the desired application, this ratio is chosen to yield optimal nonlinear coefficients with minimum gradient. Designing devices to be used at the local extrema of the nonlinearity provides passive protection against fluctuations due to variation in magnetic flux.

Suppressing Second-Order Non-linearity

The meta-material presented in the next chapters consists of SNAILs with alternating flux polarity, as depicted in Fig. 2.2. This results in neighboring cells experiencing induced flux reactions with opposite polarity. As the second-order nonlinear coefficient is an odd function of flux, this leads to adjacent cells exhibiting second-order nonlinearity with an opposite sign; and its effective suppression over meta-material [73]. Second-harmonic generation, a dominant three-wave mixing process involving the conversion of two probe photons into one at twice the probe frequency, is proportional to the modulus of the second-order nonlinear coefficient in the medium [74]. This makes it a reliable measure for quantifying the presence of second-order nonlinearity in the meta-material. Fig 2.4 shows a simulated

Back to contents

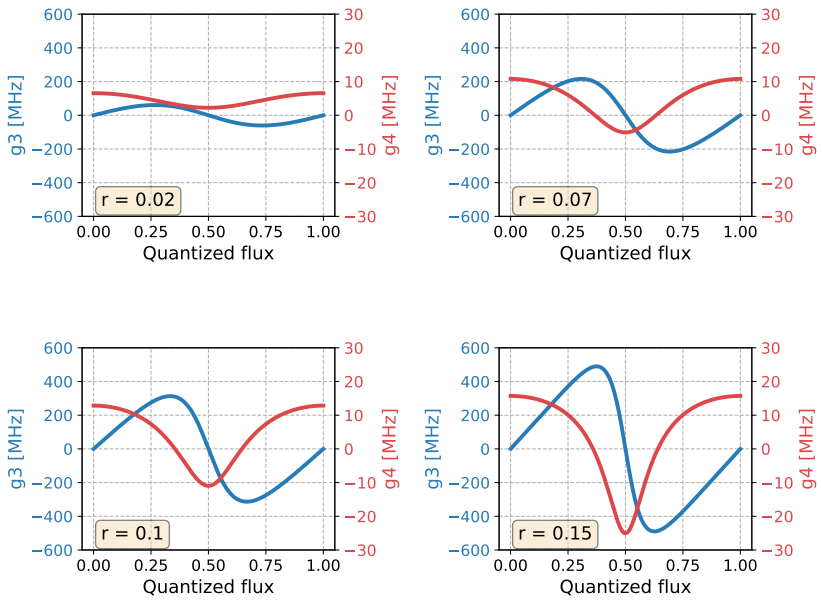

Figure 2.3: The behavior of coupling rates g_3 and g_4 as a function of applied magnetic flux for various asymmetry parameters (r).

comparison of output between meta-material with and without alternating flux polarity when a -90dBm probe tone is applied at 4 GHz at the input. As expected, the absence of significant second harmonic generation is observed when second-order nonlinearity is suppressed. The simulation was computed using transient analysis in wrspice tool [75, 76] for meta-material with 700 SNAILs and Josephson junction parameters similar to the device used to obtain reversed Kerr amplification discussed in the next chapters.

The experiments described in the next chapters utilize the four-wave mixing nonlinearity in the metamaterial, and spurious three-wave mixing processes degrade the performance of the device. Hence, this effective suppression of the three-wave mixing nonlinearity is crucial to achieving high performances, and is utilized in the presented devices.

Back to contents

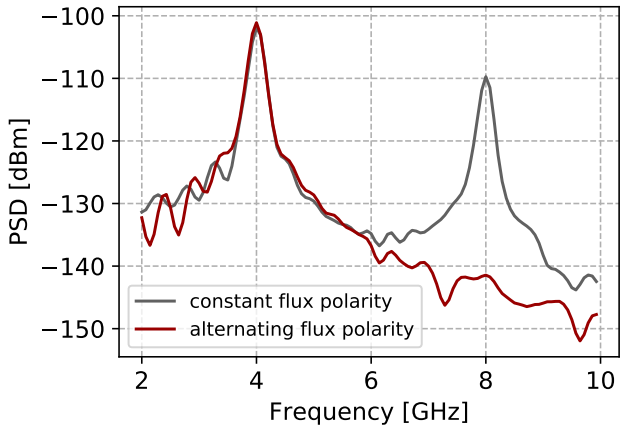

Figure 2.4: Simulated comparison between second harmonic generation in meta-materials with and without flux polarity inversion. The absence of second harmonic generation in the case of alternating flux polarity indicates adequate suppression of second order non-linearity.

Back to contents

3

FABRICATION AND SAMPLE PREPARATION

The nonlinear meta-materials used in experiments described in this thesis were fabricated in the NanoFab facility at Institute Neel, Grenoble. These devices utilize, and build upon, the inverted fabrication, i.e., a top ground technique previously developed at the institute for easily customizable fabrication of impedance-matched nonlinear transmission lines[72]. The fabrication can be largely divided into four steps, substrate preparation with markers for alignment, e-beam lithography and double angle deposition of Josephson meta-material, dielectric (alumina) atomic layer deposition (ALD), and finally, e-beam lithography and deposition of top ground. An overview of these steps is depicted in Fig. 3.1.

Although most of the methods used for fabrication have been already developed and are used regularly for the fabrication of superconducting circuits, achieving high-quality sample production requires a good deal of patience and attention to detail. In the following sections, we discuss the details of the fabrication process, design choices, and relevant tricks used for good yield of devices; and finally describe the exact recipes.

3.1 TUNABLE NON-LINEARITY FROM JOSEPHSON JUNCTIONS

Asymmetric SQUID loops are the building blocks of the tunable nonlinear meta-material and hence require a good deal of consideration to yield desired tunability [77, 78]. In principle, any squid loop containing more than two junctions can exhibit tunable second and third-order non-linearities [79]. However, fabrication constraints can pose certain limitations on the simplest feasible unit cell. We utilize standard double angle evaporation with e-beam lithography for the fabrication of Josephson junctions; this restricts that the two arms of the loop have identical parity, i.e., both have either an odd or an even number of Josephson junctions. With this restriction, the simplest unit cell that can be fabricated contains four Josephson junctions, three in the first arm and one in the second.

Two commonly used fabrication technique for Josephson junctions involve utilizing a Dolan bridge [80] or bridge free technique [81]. The bridge-free technique enables easy and consistent fabrication of a wide range of junction sizes and is very widely employed to make devices containing from a single Josephson junction to thousands of Josephson junctions [72, 82]. We use it for fabricating Josephson meta-material with single Josephson junction or symmetric SQUID in a unit cell. However, the ledge used for breaking metal deposition angle symmetry in this technique is very sensitive to secondary exposure. As described in chapter 2, to make a 50Ω impedance-matched transmission line with SNAILs, we need to introduce capacitive fins along with the SNAILs to the unit cell. This introduces significant secondary exposure close to the Josephson junctions rendering bridge free fabrication technique inadequate.

3.2 ELECTRON-BEAM LITHOGRAPHY

All the samples described in the thesis were fabricated using electron-beam(e-beam) lithography for defining structures. E-beam lithography is a common technique used for high-resolution patterning of small structures. It involves coating the substrate with a special chemical called resist and then selectively exposing desired patterns with a focused electron beam. Depending on the properties of the resist used, exposure with an electron beam can damage the resist bonds or strengthen them (by polymerization or cross-linking), differentiating its solubility in special solvents, called developers, from unexposed resist. Commercial e-beam lithography system nB5 from Nanobeam Ltd. was used to pattern structures on the resist, which allows automation and remote control permitting easy fabrication of multiple devices.

The current and acceleration potential used to create the electron beam poses a limitation on the resolution of the patterns to be exposed. High acceleration potentials minimize the spread of electrons when they scatter in the resist (usually referred to as back-scattering). Thus, lower currents with higher acceleration potentials lead to narrower beam exposure profiles [83]. A high-resolution beam is necessary for fabricating a large number of sensitive patterns with high consistency; hence 80 kV acceleration potential was used, which is towards the higher end of the capability of commercial lithography systems. Various beam

Back to contents

currents ranging from 1 nA to 50 nA were used for exposing the resist, depending on the desired resolution to speed up the exposure.

The selection of an appropriate resist is very important for optimizing the lithography process. For patterning small structures like a transmission line with Josephson junctions, it is faster to use a positive resist, i.e., a resist in which chemical bonds can be damaged by exposure. In contrast, for patterning large structures like a ground plane that covers most of the substrate surface, a negative resist, in which exposure strengthens the bonds, is more suitable. The markers used for alignment of patterns across subsequent exposures were patterned on a thin (150 *nm*) polymethyl methacrylate (PMMA 3%) resist to achieve high precision. For patterning transmission lines with Josephson junctions, a bi-layer stack of positive resists constituted from methyl methacrylate and polymethyl methacrylate (PMMA/-MAA 9%, PMMA 4%), with different sensitivity to electron beam was used to create hanging structures. For patterning the top ground plane, a mono-layer of proprietary negative resist (ARN 7700-18) from Allresist GmbH was used.

After exposure to e-beam, the unwanted resist needs to be removed by dissolving it in an appropriate solvent called developer, in a process commonly referred to as development. The process of patterning with the resist needs to be optimized separately for different resist stacks. This includes calibration of exposure with e-beam, selection of an appropriate developer, time of wash with the developer, and temperature of the developer. Lowering the temperature of the developer can slow down the process of dissolving, needing higher e-beam exposure; this can be utilized to minimize the effects of secondary (unwanted) exposure. However, this optimization was skipped for the fabrication of devices presented in this thesis, as development at room temperature was sufficient to obtain the required consistency.

3.3 LITHOGRAPHY ALIGNMENT AND OPTIMIZATION

The fabrication process described in this chapter involves multiple lithography steps. Hence, it is very critical to achieve high precision alignment of structures across the lithography steps to

Back to contents

fabricate samples with high efficacy. A pattern of 8x8 μm gold squares on 2-inch wafers was used to define aligning markers along with features defining the boundary of the samples on the wafer to help with dicing.

Along with position alignment, high-precision predefined structures on the substrate can also be used to optimize the focusing of the electron beam and calculate skew and scaling factors for the pattern originating from small tilts and rotation in the placement of the substrate in the lithography system. Focusing on the four corners of the device to be fabricated is used to calculate the plane of the substrate in three dimensions and apply necessary transformations to the exposure patterns. This step is very important for optimizing beam profile throughout the exposure, leading to high precision and reproducibility.

The region on the substrate that can be exposed by tilting the electron beam without moving the substrate is known as the write-field of the lithography. The write-field used for lithography also determines the smallest step the beam can take, i.e., the precision of exposing the pattern. Typical write field sizes needed to maintain the required precision for fabricating the devices under discussion are much smaller than the device size. This necessitates movement of the substrate during patterning and precise stitching at the borders. Careful placement of these stitches away from sensitive elements like the Josephson junctions is very important for achieving high-quality fabrication.

3.4 METAL DEPOSITION

After the development of the exposed resist, metal needs to be deposited to form desired structures. Electron beam / thermal evaporation and sputtering are some commonly used methods of deposition of metals in vacuum. Thermal and electron beam evaporation involves melting and evaporating the metal and can be utilized to achieve directional deposition, needed for fabrication of Josephson junction using double angle method. In contrast, sputtering involves hitting the target metal with energetic ions, forming a cloud and isotropic deposition of the metal.

A commercial electron beam evaporator from Plassys was used for all metal depositions. The evaporator featured two

Back to contents

chambers connected by a large gate valve, load lock, and main evaporation chamber. The load lock allows faster loading and unloading of samples and controlled exposure of deposited metal to gases; while maintaining a high vacuum at the crucibles in the main chamber containing metal targets, preserving their purity.

Josephson junction composite

Aluminum Josephson junctions can be fabricated in one lithography step using the double-angle deposition technique. The two common double angle techniques, bridge free and with Dolan bridges, involve utilizing shadows of the hanging structures made with bi-layer resist to break the continuity of the deposited metal.

First, a thin layer of aluminum is deposited at an angle. The second step involves controlled oxidation of this deposited layer to form aluminum oxide that acts as the barrier between two superconducting Aluminum layers at low temperatures. To form this oxide layer, the freshly deposited aluminum is exposed to a controlled oxygen environment for a fixed time. The time of exposure and partial pressure of oxygen gas used for the oxidation determines the thickness of the oxide. This thickness controls the critical current of the fabricated Josephson junction and needs to be carefully controlled. After the controlled oxidation, the second layer of aluminum is deposited at an angle to form the structures containing Josephson junctions.

The double-angle method used for the fabrication of Josephson junctions can lead to the creation of spurious junctions. However, for most applications, it is easy to design samples ensuring negligible contribution of these spurious junctions to the desired nonlinear interaction.

The recipes described in this chapter are tested to yield a consistent fabrication for junction sizes from 0.2 to 3 μm^2 for the Dolan bridge and from 1.4 to 15 μm^2 for bridge free technique.

The top ground

The top metal layer forms the active ground plane for the nonlinear transmission line and covers the device as depicted in

Fig. 3.1. Devices consisting of unit cells with a loop containing Josephson junctions are tuned by applying a magnetic field. This requirement prohibits the use of superconducting ground planes. Hence, for the devices discussed in this thesis, the ground plane was fabricated with copper (or gold), which remains metallic at cryogenic temperatures. Using a metallic ground plane, in contrast to a superconducting one, does increase conductor losses of the transmission line. However, as the dominant contribution to the transmission losses in the device comes from the dielectric layer, using metallic ground does not impact device performance significantly [84]. A detailed analysis of losses in these devices is presented in chapter 6.

Alignment and focus markers

High precision markers on the substrate are essential for consistent multi-layer fabrication. For electron beam lithography, gold markers are very commonly used as the high atomic mass of gold leads to large electron scattering and high contrast imaging. As a first step in the process, gold markers were fabricated on the substrate.

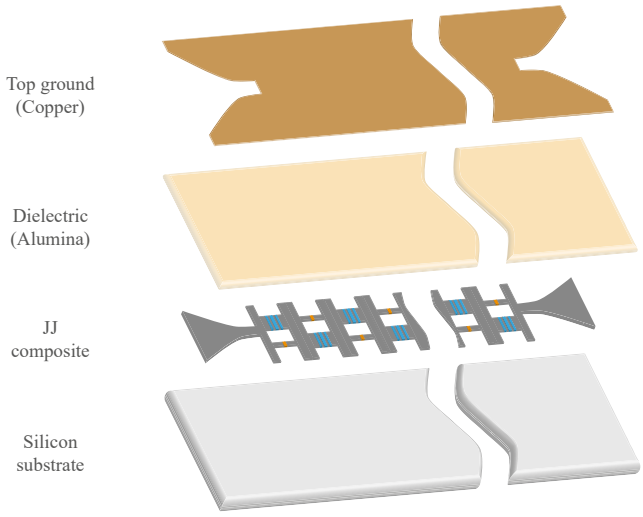

Figure 3.1: **Fabrication steps** The device is fabricated with double angle aluminum Josephson junction array deposition on silicon substrate, followed by atomic layer deposition of dielectric (alumina) and finally by copper top ground deposition.

Back to contents

3.5 EXCESS METAL LIFT-OFF

During the deposition, metal is deposited uniformly on the sample; however, the substrate is metalized as dictated by the pattern of the developed resist. Rest of the metal lands on top of the resist, which needs to be removed. This is accomplished by dissolving the resist in a strong solvent, often heated to speed up the process. Depending on the resist, solvent, temperature, and pattern, this process, commonly known as lift-off, can take from several minutes to hours. Ultrasonic treatment of the sample after lift-off helps in achieving clean metal edges. However, it needs to be avoided when adhesion between deposited layers in the sample is weak.

3.6 OXYGEN PLASMA CLEANING

Developing the resist after electron beam patterning (exposure) dissolves it in places where the metal is to be deposited. Even an optimized development procedure still leaves trace amounts of resist on the substrate. This leftover resist, if left untreated, can lead to additional losses in the device at cryogenic temperatures. To mitigate these additional losses, oxygen plasma cleaning is employed after development to remove the trace amounts of leftover resist. The cleaning intensity needs to be carefully optimized to remove unwanted resist without damaging the intended resist pattern. Similarly, trace amounts of resist are left on the sample after the lift-off process. A strong oxygen plasma cleaning was used to remove the same.

3.7 IMPEDANCE OPTIMIZATION

The performance of the fabricated nonlinear transmission line critically depends on its impedance matching to the microwave environment. This impedance is determined by the inductance provided by the Josephson junctions and the capacitance provided by the capacitor formed between the nonlinear transmission line and the top ground. As the dielectric layer between the nonlinear transmission line and the top ground is very thin, capacitance can be adequately approximated by a parallel-plate model considering the area of the metalized nonlinear transmission line. We fabricated test structures containing a varying number of Josephson junctions along with the device to allow room temperature characterization of junction resistance. The

Back to contents

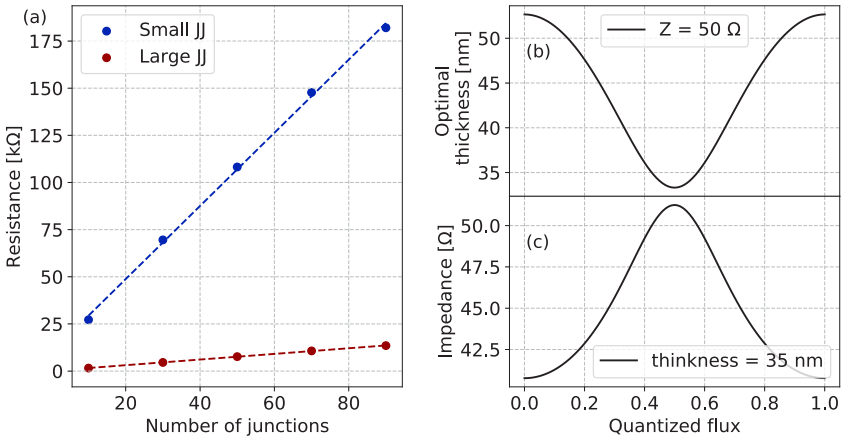

Figure 3.2: Panel (a) shows the measured resistance of small and large junctions in a typical device containing SNAIL cells as a function number of cells along with the fit to obtain resistance of one junction. In this case, the resistance of one small junction was 2 kΩ, and one large was 150 Ω. (b) The optimal thickness of dielectric (aluminum oxide) to obtain 50 Ω impedance line as a function of external magnetic flux applied to the loop. (c) The impedance of the transmission line fabricated with 35 nm thick dielectric as a function of external magnetic flux applied to the loop.

Back to contents

junction resistance was obtained by measuring the resistance of the test chains and then calculating the slope for the linear fit. Ambegaokar-Baratoff relation can be used to map the resistance of the Josephson junction to its critical current. It should be noted that the resistance of the junction depends on the temperature; we use a correction factor of 30% to account for the change in the resistance as the device is cooled down [85]. Magnetic flux dependent inductance of the cells constituting the nonlinear transmission line can be then calculated, as described in chapter 2. The thickness of the dielectric is then optimized to yield impedance matching to the environment at desired flux point. Fig. 3.2 depicts the resistance of the test chains as a function of the number of junctions in it and optimized impedance as a function of applied magnetic field for a typical device with SNAIL cells.

The wave traveling through the device encounters two critical transitions, from coaxial waveguide to co-planar waveguide (CPW) on printed circuit board (PCB) and from CPW to microstrip in the device. The geometry of these transitions was optimized using finite element simulation tools.

3.8 DIELECTRIC DEPOSITION

The thin dielectric layer that enables the fabrication of these low impedance nonlinear transmission lines can also be a significant source of losses. The effect of these losses on the device performance is discussed in chapter 6. Due to this critical dependence of performance on the dielectric layer, it is important to carefully select the dielectric material as well as the method of deposition. Aluminum oxide deposited using atomic layer deposition (ALD) was used as the top dielectric for all the devices described in this thesis. The process utilized allowed conformal fabrication of layers as thin as 20 nm, which prescribes a limit for specific capacitance. When necessary, extra metal pads were added to the nonlinear transmission line to overcome this limitation on capacitance.

During the process of ALD, the substrate containing the Josephson junctions is heated up to $200^{\circ}C$. Approximately 10% reduction in critical currents of the junctions was observed between measurements just before and after the deposition.

Back to contents

In chapter 9 and appendix A.1, we briefly describes some ongoing efforts towards optimizing dielectric performance.

3.9 PACKAGING THE SAMPLES

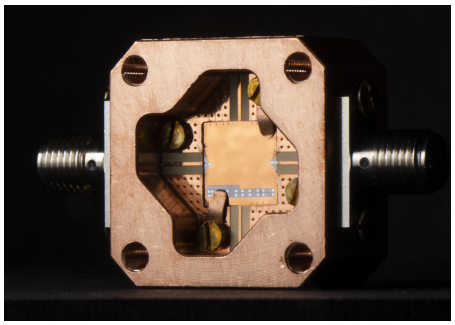

Figure 3.3: **Packaging.** A typical nonlinear transmission line fabricated on silicon substrate, wire bonded to the PCB of sample box with SMA connector for microwave input and output.

In each fabrication run, sixteen 8x8 mm devices were fabricated on a two-inch wafer in a 4x4 matrix. At the end of the fabrication cycle, the devices were diced with a diamond saw. The harsh action of the saw and the coolant was observed to cause significant damage to the top ground. To protect the samples against the same, the wafer was spin-coated with a thick resist and then applied with a thin PVC tape with acrylic adhesive. A standard acetone wash was used to remove these protective layers.

After dicing, the device needs to be wire bonded to the PCB in the sample box. Fig. 3.3 depicts a sample mounted in the sample box and wire bonded to the PCB. The dielectric layer is conformally deposited on the whole sample, including the bonding pads of the transmission line. The ultrasonic action of the bonder was observed to penetrate the dielectric layer as thick as 40 nm; however, an appropriate etching was needed for wire bonding samples with thicker dielectric layers.

Back to contents

3.10 RECIPES

Markers

Step	Description
Cleaning	RIE with O_2 at 20W for 120 s Baking at 180°C for 120 s
Resist spin coating	PMMA 3%; 4000 rpm @ 4000 rpm/s for 30 s Baking at 180°C for 300 s
e-beam exposure	Dose : 10 C/m^2 @ 80 kV and 40 nA
Development	Bath 1: MIBK:IPA 1:3 for 60 s Bath 2: IPA for 30 s Rinse : ethanol N_2 blow dry
Metal deposition	Titanium : 5 nm @ 0.1 nm/s Gold : 200 nm @ 0.1 nm/s
Lift-off	Bath : NMP for 4 hours at 80°C Rinse : acetone, ethanol, IPA N_2 blow dry [No ultrasonic]

Table 3.1: Fabrication process for markers.

Back to contents

JJ composite

Step	Description
Cleaning	RIE with O_2 at 20W for 120 s Baking at 180°C for 120 s
Resist spin coating	PMMA/MAA 9%; 4000 rpm @ 4000 rpm/s for 30 s Baking at 200°C for 600 s PMMA 4%; 5000 rpm @ 5000 rpm/s for 30 s Baking at 180°C for 300 s
e-beam exposure	Dose for pads : 10-12C/m^2 @ 80 kV and 40 nA Dose for central line (JJ) : 8-10 C/m^2 @ 80 kV and 1.5 nA Dose for undercuts : 1-3 C/m^2 @ 80 kV and 1.5 nA
Development	Bath 1: MIBK:IPA 1:3 for 60 s Bath 2: IPA for 30 s Rinse : ethanol N_2 blow dry
Cleaning	RIE with O_2 at 10W for 15 s
Double angle evaporation	Aluminum : 20 nm @ 0.1 nm/s ; at -35° Oxidation : 1.5 mbar O_2 for 300 s Aluminum : 50 nm @ 0.1 nm/s ; at +35°
Lift-off	Bath : NMP for 24 hours at 80°C Mild ultrasonic for 60 s Rinse : acetone, ethanol, IPA N_2 blow dry

Table 3.2: Fabrication process for central transmission line containing Josephson junction composite.

Back to contents

Top dielectric

Step	Description
Cleaning	RIE with O_2 at 20W for 120 s
Chamber preparation	Heating : 250°C N_2 flow at 5 sccm
ALD cycle	Trimethylaluminum pulse : 15 ms Wait : 10 s Water pulse : 15 ms Wait : 10 s [number of cycles : thickness in Å]

Table 3.3: Fabrication process for top dielectric layer.

Back to contents

Top ground

Step	Description
Cleaning	RIE with O_2 at 20W for 120 s
Resist spin coating	ARN 7700-18; 750 rpm @ 500 rpm/s for 90 s Baking at 85°C for 90 s
e-beam exposure	Dose : 10 C/m^2 @ 80 kV and 40 nA
Heat treatment	Baking at 105°C for 120 s
Development	Bath 1: AR-300-46 for 180 s Bath 2: DI water for 30 s Rinse : DI water N_2 blow dry
Cleaning	RIE with O_2 at 10W for 15 s
Metal evaporation	Titanium : 10 nm @ 0.1 nm/s ; at 0° Copper : 400 nm @ 0.5 nm/s ; at 0°
Lift-off	Bath : AR 300-76 for 24 hours at 80°C Rinse : acetone, ethanol, IPA N_2 blow dry [No ultrasonic]

Table 3.4: Fabrication process for top ground.

Back to contents

Part II

BROADBAND AMPLIFICATION NEAR QUANTUM LIMIT

4

TRAVELING WAVE PARAMETRIC AMPLIFICATION

Low-noise broadband amplification of microwave signals is a critical segment of low-temperature instrumentation. Nonlinear wave mixing processes can be utilized to implement low-noise parametric amplification. These parametric amplifiers underwent an enormous development in recent decades, particularly due to their direct applications and ease of integration to the rapidly evolving field of superconducting circuits based quantum information processing [86, 87].

Parametric amplifiers constructed with resonant structures constituted of Josephson junctions (JPAs) [22, 23] have been demonstrated to provide quantum-limited amplification [24–27]. These amplifiers are widely used for low-noise amplification of microwave signals [28]. However, the resonant nature of the amplifier constrains their bandwidth and saturation. These constraints have been individually resolved by engineering the resonant structure constituting the amplifier [88, 89]. Recently, these limitations have been simultaneously overcome by traveling wave parametric amplifiers (TWPAs) consisting of non-resonant nonlinear transmission lines [30].

In this chapter, we start the discussion with the quantum limit of noise added by the amplifier in the non-degenerate mode of operation, introduce the semi-classical framework for quantifying traveling wave parametric amplification in Josephson metamaterials, and pre-existing approaches to the phase-matching problem; and then finally discuss the utilization of in-situ Kerr reversal for phase matching.

4.1 QUANTUM LIMIT ON AMPLIFIER NOISE

When an amplifier amplifies a signal, it also adds some noise during the process of amplification. The seminal work by C. M. Caves [24] published in 1982 explains that laws of quantum mechanics constrain this added noise to non-vanishing quantities. Consider a parametric amplifier operating in non-degenerate

mode i.e. preserving the phase of the input signal $a^\dagger_{\text{in}}$, with amplification G,

$$a^\dagger_{\text{out}} = \sqrt{G} a^\dagger_{\text{in}}, \tag{4.1}$$

where $a^\dagger_{\text{out}}$ is the amplified output. As both $a^\dagger_{\text{in}}$ and $a^\dagger_{\text{out}}$ are quantum operators, they must obey commutation relations,

$$[a_{\text{in/out}}, a^\dagger_{\text{in/out}}] = 1. \tag{4.2}$$

Operators related by Eq. 4.1 violate these commutation relations. To ensure their fulfillment, it is necessary to add an extra degree of freedom, commonly referred to as idler mode, which interacts with the signal mode to generate output,

$$a^\dagger_{\text{out}} = \sqrt{G} a^\dagger_{\text{in}} + \sqrt{G-1} b_{\text{in}}, \tag{4.3}$$

where operator b_{in} denotes the input at idler mode. In general, the quantum fluctuations of input signal and idler mode are not correlated. Assuming no input at the idler mode, i.e. b_{in} is in quantum ground state, the mixing of signal and idler mode adds

$$\frac{1}{2}\sqrt{G-1} \tag{4.4}$$

noise photons to the signal output, during the process of amplification. In large gain limit ($G \gg 1$), an ideal amplifier adds at least half a quanta of noise per unit gain, which is commonly known as input refered added noise of the amplifier. In the following chapters, we refer to this as the noise added by the amplifier. Adding this to the quantum fluctuations of the signal mode, we get the standard quantum limit on total noise, which we also refer to as the system noise of the amplification. Often, we will refer to the amplification noise in temperature units as this makes it easier to compare it to the thermodynamic temperature of the experimental setups.

Quantum-limited amplification chain

Practically, the experimental setup for the measurement of low-power signals is implemented using a chain of amplifiers. The noise added by an amplification chain can be expressed as,

Back to contents

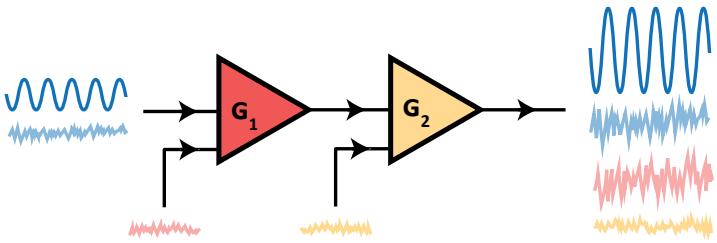

Figure 4.1: Amplification chain with two amplifiers and their added noise.

$$N_{\text{total}} = N_1 + \frac{N_2}{G_1} + \frac{N_3}{G_1 G_2} + \ldots, \tag{4.5}$$

where (N_i, G_i) are the added noise and gain of i^{th} amplifier in the chain. This indicates that the noise temperature of the first amplifier makes the largest contribution to the noise temperature of the chain; hence, it needs to be as low as possible. The noise added by the second amplifier and onward is suppressed by the gain of the preceding amplifiers. High-electron-mobility transistor (HEMT) amplifiers are well suited for use as the second amplifier in the amplification chain. A power gain factor of around 100 (20 dB) of the first amplifier can effectively suppress the noise added by the HEMT amplifier as depicted in Fig. 4.2.

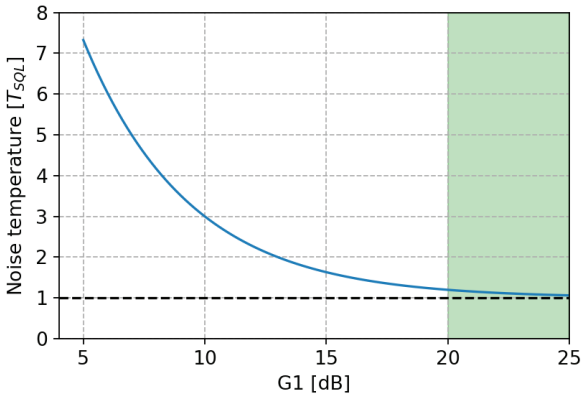

Figure 4.2: Noise temperature of the amplification chain in units of standard quantum limit, as a function of gain of first amplifier followed by a typical HEMT amplifier. The noise temperature of the measurement setup approaches quantum limit for gains above 20 dB.

Back to contents

Hence, to construct a near quantum-limited amplification chain, the first amplifier should have noise performance as close to the quantum limit as possible and a gain of about 20 dB to suppress noise added by amplifiers further down the chain. This sets the performance targets for the traveling wave parametric amplifier to be utilized as the first amplifier in the amplification chain.

4.2 TRAVELING MODES IN NON-LINEAR MEDIUM

Following the methods described in [71, 91], a field ϕ traveling in transmission line constructed with SNAIL cells (presented in chapter 2), as depicted in Fig. 4.3, can be described by,

$$\frac{\partial^2\phi}{\partial x^2} - \frac{1}{\omega_o^2}\frac{\partial^2\phi}{\partial t^2} + \frac{1}{\omega_J^2}\frac{\partial^4\phi}{\partial x^2\partial t^2} + 6g_3\sqrt{\frac{R_Q}{\pi\omega_o^2 Z}}\frac{\partial}{\partial x}\left[\left(\frac{\partial\phi}{\partial x}\right)^2\right] - 8g_4\frac{R_Q}{\pi\omega_o Z}\frac{\partial}{\partial x}\left[\left(\frac{\partial\phi}{\partial x}\right)^3\right] = 0, \tag{4.6}$$

where $R_Q = h/4e^2$, Z (defined as $\sqrt{L/C_g}$) is the characteristic impedance of the transmission line, $\omega_J = \sqrt{1/LC_J}$, $\omega_o = \sqrt{1/LC_g}$, denote the plasma frequency and the characteristic frequency of the transmission line, respectively. The coupling rates g_3 and g_4, for three-wave and four-wave mixing interactions are defined in Eq. 2.15.

The first three terms of the equation describe the dispersion of the traveling mode in the medium; the fourth term describes second-order ($\chi^{(2)}$) nonlinearity resulting in three-wave mixing processes, and the last describes third-order ($\chi^{(3)}$) nonlinearity resulting in four-wave mixing processes. Low power dispersion in the medium can be obtained by solving Eq. 4.6 in the limit of vanishing nonlinear couplings [91],

$$k_m = \frac{\omega_m}{\omega_0\sqrt{1-\omega_m^2/\omega_J^2}} \tag{4.7}$$

where k_m is the dimensionless wave vector, and ω_m is the frequency of the described mode.

Back to contents

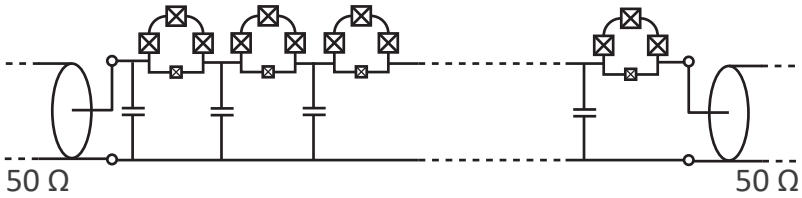

Figure 4.3: A nonlinear transmission line constituted from SNAILs (Superconducting Nonlinear Asymmetric Inductive eLements).

4.3 FOUR WAVE MIXING PROCESS FOR AMPLIFICATION

These nonlinearities can be exploited to couple a weak mode with a highly populated mode in the medium, and engineer coherent energy exchange, resulting in amplification of the weak mode. We will restrict the main discussion in this thesis to non-degenerate amplification due to four-wave mixing. However, other amplification schemes can be realized utilizing the presented nonlinear platform. In practice, we use techniques discussed in section 2.5 to suppress three-wave mixing processes in the device, which can degrade its performance.

The process of non-degenerate four-wave mixing amplification involves the conversion of 2 quantas of energy from highly populated (pump) mode to 1 quantum at weak mode to be amplified (signal) mode and leftover energy to 1 quantum at auxiliary (idler) mode. Ansatz for these three modes (signal, idler, pump),

$$\phi(x,t) = \sum_{m=s,i,p} \frac{1}{2}\left[A_m(x)e^{i(k_m x-\omega_m t)} + c.c.\right], \tag{4.8}$$

where $A_m(x)$ is the position-dependent complex amplitude, can be used in field Eq. 4.6 and dropping off-resonant terms to obtain coupled differential equations describing the four-wave mixing amplification process. Which can be further simplified with strong pump ($A_p \ll A_{s,i}$) and WKB approximation,

$$\left|\frac{\partial^2 A_m}{\partial x^2}\right| \ll k_m \left|\frac{\partial A_m}{\partial x}\right| \ll k_m^2 |A_m|, \tag{4.9}$$

to yield coupled mode equations,

$$\left(\partial_x + \frac{i\Delta k}{2}\right) A_\mathrm{s} = i\frac{k_\mathrm{i}}{2k_\mathrm{s}}\eta_\mathrm{s} A_\mathrm{i}^* - k_\mathrm{s}'' A_\mathrm{s}, \tag{4.10}$$

Back to contents

$$\left(\partial_x - \frac{i\Delta k}{2}\right) A_{\mathrm{i}}^* = -i\frac{k_{\mathrm{s}}}{2k_{\mathrm{i}}}\eta_{\mathrm{i}} A_{\mathrm{s}} - k_{\mathrm{i}}'' A_{\mathrm{i}}^*, \tag{4.11}$$

$$\eta_{\mathrm{s,i}} = \frac{6g_4 R_Q}{\pi\omega_0 Z\widetilde{\omega}_{\mathrm{s,i}}} k_{\mathrm{p}}^2 k_{\mathrm{s,i}} |A_p|^2, \quad \eta_p = \frac{3g_4 R_Q}{\pi\omega_0 Z\widetilde{\omega}_p} k_{\mathrm{p}}^3 |A_p|^2, \qquad \widetilde{\omega}_m = \left(1 - \frac{\omega_{\mathrm{m}}^2}{\omega_{\mathrm{J}}^2}\right) \tag{4.12}$$

where $k_{\mathrm{s,i}}$ are the real component of signal and idler wavevectors, Δk (Eq. 4.15, described in following subsection) is the total phase mismatch, and $k_{\mathrm{s,i}}''$ are the imaginary component of signal and idler wavevectors. $\eta_{\mathrm{s,i}}$ are coupling constants dependent on Kerr strength (g_4).

If the nonlinear medium is lossless ($k_{\mathrm{s,i}}'' = 0$) and treating $A_{\mathrm{s,i}}$ as semi-classical fields with zero initial idler boundary condition, we get the familiar expression [9, 11, 39, 91] for the non-degenerate four wave mixing power gain,

$$G_{\mathrm{power}} = \cosh^2(gx) + \frac{\Delta k^2}{4g^2}\sinh^2(gx), \tag{4.13}$$

where x is position along the TWPA and g is the reduced gain coefficient,

$$g = \sqrt{\left(\frac{k_s^2 k_i^2 \left(2k_p - k_s\right)\left(2k_p - k_i\right)\omega_p^4}{k_p^6 \omega_i^2 \omega_s^2}\right)\eta_p^2 - \left(\frac{\Delta k}{2}\right)^2}. \tag{4.14}$$

Phase mismatch in traveling modes

The term Δk in Eq. 4.13 corresponds to the phase mismatch between the three modes involved in the process of amplification. This total phase mismatch can be expressed as the sum of two contributions,

$$\Delta k = \Delta k_{\mathrm{dispersion}} + \Delta k_{\mathrm{Kerr}}. \tag{4.15}$$

The first term denotes the phase mismatch contributed by curvature of the dispersion relation in Eq. 4.7, arising from frequency dependence of phase velocities in the nonlinear medium,

Back to contents

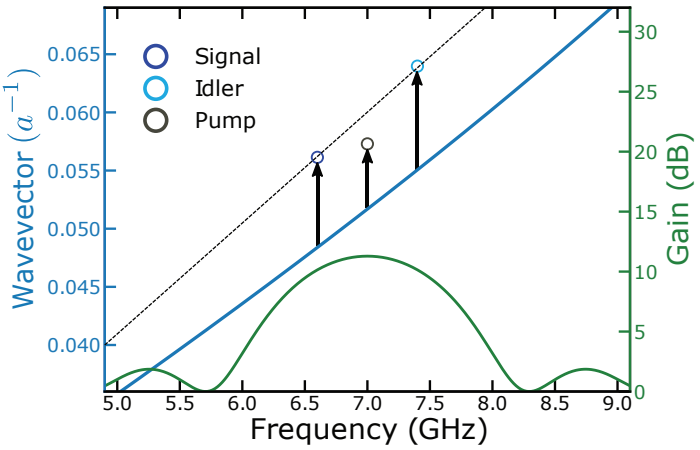

Figure 4.4: Origin of phase mismatch for 4WM amplification, exaggerated for clear visualization. The solid blue line indicates the curvature of the dispersion due to the plasma frequency of the Josephson junctions. The black arrows indicate the modification of the signal, idler, and pump wavevectors due to the Kerr effect. The dashed black line indicates the 4WM phase matching condition for these modes. This deviation from the phase-matching condition results in sub-optimal gain performance, as depicted by the green curve.

Back to contents

$$\Delta k_{\text{dispersion}} = k_s + k_i - 2k_p. \tag{4.16}$$

Second term denotes the mismatch arising due to unequal Kerr effect experienced by the modes,

$$\Delta k_{\text{Kerr}} = \eta_s + \eta_i - 2\eta_p. \tag{4.17}$$

In a typical nonlinear medium, these two contributions have the same sign and add up, as depicted in Fig. 4.4. Power gain described by Eq. 4.13 indicates that the phase mismatch between traveling modes involved in the process of amplification (Δk) will suppress the amplification. Which makes practical implementation of the amplifier meeting desired performance targets described in section 4.1 difficult and necessitates implementation of phase-matching solutions.

Dispersion engineering for phase matching

The Josephson junction based nonlinear medium under discussion is fabricated using cellular meta-material, i.e., a typical device has thousands of unit cells containing Josephson junctions, with the size of each cell orders of magnitude smaller than the operating wavelength [72]. This allows for a unique opportunity to easily modify the properties of the medium at sub-wavelength scales.

One approach to solving the problem of phase matching (Eq. 4.15) is to modify the dispersion contribution ($\Delta k_{\text{dispersion}}$) to the total phase mismatch (Δk) in a manner that it vanishes in the intended amplification band. This can be achieved by opening a gap in the dispersion relation and utilizing the curvature close to the gap to reverse the sign of dispersion phase mismatch. This technique, known as dispersion engineering, has been demonstrated by opening a gap using resonant couplers [9, 93] and using a photonic crystal approach [11] to solve the problem of phase matching in traveling wave parametric amplifiers in the frequency range of several GHz. The basic operational idea of this approach is depicted in Fig. 4.5.

Although this approach to phase matching can deliver sufficient gain to implement a near quantum-limited amplification

Back to contents

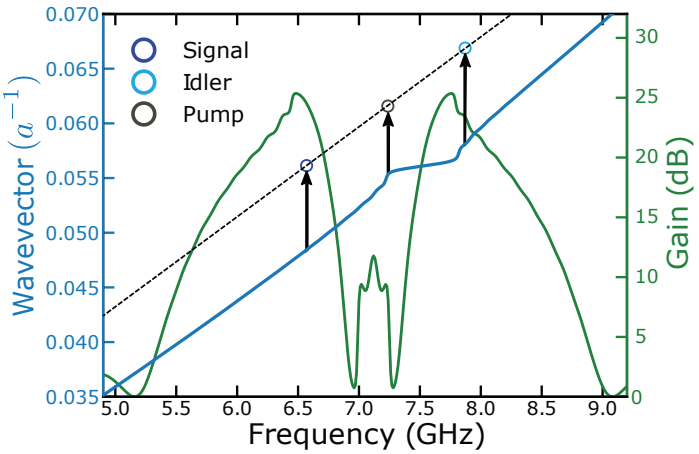

Figure 4.5: Dispersion engineering to achieve phase matching for 4WM amplification process. The blue curve indicates the wavevector modified by the presence of the gap feature close to 7 GHz. By placing the pump mode close to the kink in the dispersion due to this gap, the phase-matching condition (dashed black line) can be satisfied; and the desired gain performance can be attained, as depicted by the green curve.

chain over a bandwidth of several GHz, it also imposes some limitations and disadvantages. The dispersion feature in these phase-matched devices leads to a gap in the middle of the amplification band; and poor impedance matching in its proximity. Such impedance mismatches lead to gain ripples, as depicted in Fig 4.6, and minimization of these ripples is highly desirable. See appendix A.2 for estimation of gain ripples. The gap feature in the dispersion is design dependent, which limits the in-situ tunability of the amplification band. These limitations encourage the exploration of alternative schemes.

Back to contents

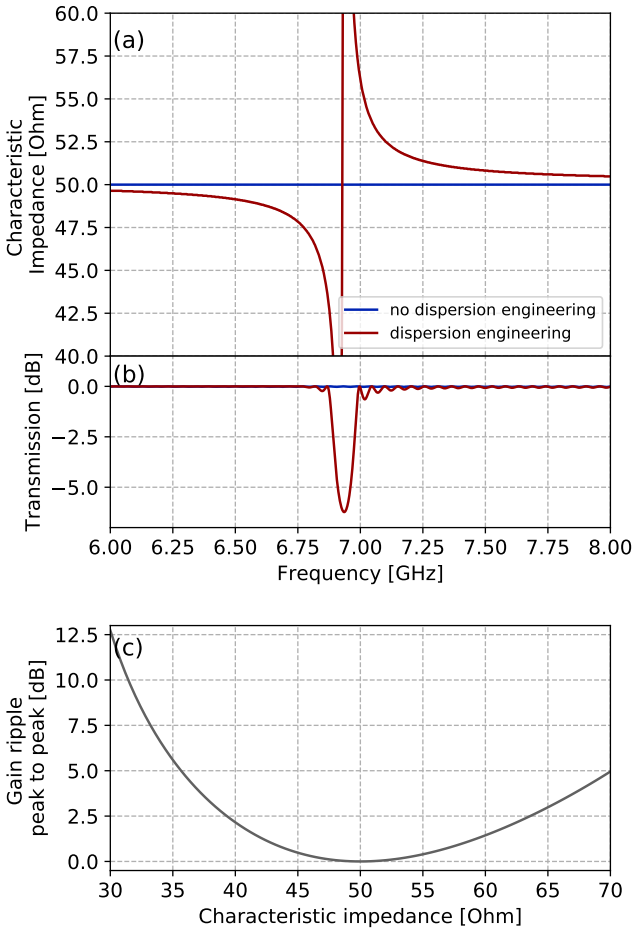

Figure 4.6: Ripples in gain profile due to impedance mismatches. (a) The simulated characteristic impedance of a transmission line with and without dispersion engineering. (b) The gap in the transmission created by the modulation. (c) Simulated peak-to-peak gain ripples versus characteristic impedance of the TWPA with 20 dB gain. Gain ripples are minimized when the TWPA impedance matches 50 Ω environment impedance.

Back to contents

Kerr reversal for phase matching

An alternative to the modification of dispersion of the waves in the nonlinear medium is to modify the Kerr contribution (Δk_{Kerr}) to the total phase mismatch (Δk, Eq. 4.15) in a manner that it vanishes in the intended amplification band, as explained in Fig. 4.7.

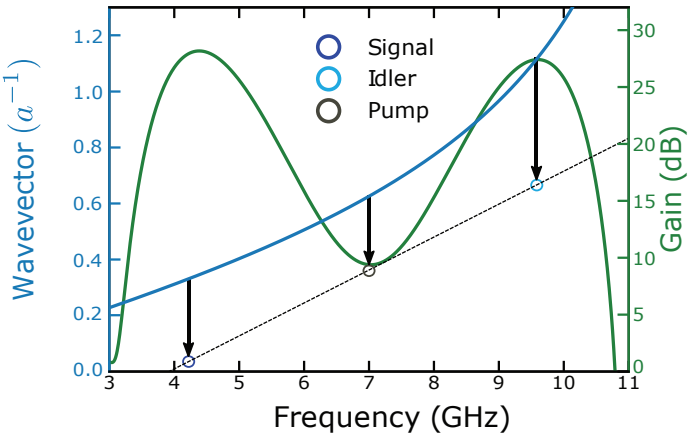

Figure 4.7: Kerr reversal to achieve phase matching for 4WM amplification process. The solid blue line indicates the curvature of the dispersion due to the plasma frequency of the Josephson junctions. The black arrows indicate the modification of the signal, idler, and pump wavevectors due to the Kerr effect. By reversing the direction of these arrows. i.e., Kerr contribution, phase-matching condition (dashed black line) can be satisfied; and the desired gain performance can be attained, as depicted by the green curve.

Using Eq. 4.12 and Eq. 4.17,

$$\Delta k_{\text{Kerr}} \propto g_4 |A_p|^2. \tag{4.18}$$

This implies that reversing the Kerr contribution to phase mismatch translates to a sign reversal of the Kerr nonlinearity in the medium. This can be accomplished by appropriately designing the nonlinearity constituting the medium, as described in chapter 2.

Back to contents

The modeling and experimental characterization of the reversed Kerr traveling wave parametric amplifier thus constructed is discussed in the next chapters.

Back to contents

5

A REVERSED KERR TRAVELING WAVE PARAMETRIC AMPLIFIER

In this chapter, we start with the description of the measurement setup, discuss the characterization of the device in the linear regime, build a realistic model for gain simulation and finally describe the amplification performance of the device.

5.1 MEASUREMENT SETUP

The device is experimentally characterized in a dilution refrigerator at 20 mK with microwave electronics setup as depicted in Fig 5.1. The cryostat dubbed "SionludiXL" (dilution, reversed) was designed and manufactured in-house at the Institute Neel workshop, and features a large (30 cm) base plate with rapid (10 hours) cool-down capability. The implementation of microwave switches was instrumental in making the measurement setup remotely operable and easing the measurements during the (COVID) pandemic times.

The input line contains attenuators placed at various temperature stages of the cryostat to gradually cool down the microwave environment presented by the transmission line. At the base plate (20 mK), a directional coupler is used to connect the device with a thermal noise source at the direct insertion port and input line at the (20 dB) coupled port. Microwave switches[1] were employed to switch between the device and a bypass for in-situ linear and noise characterization of the device. The output line is decoupled from higher temperatures in the frequency band of interest using isolators to avoid attenuation and maintain a higher signal-to-noise ratio (SNR). The first amplifier in the measurement setup, a high electron mobility transistor (HEMT) amplifier, rests at the 4K stage of the cryostat and is followed by low noise amplifiers at room temperature. A superconducting coil is mounted to the device holder allowing control over mag-

[1] We observed no discernible issues arising from the use of microwave switches in the measurement setup, over several hundred switching operations.

netic flux threading the SNAILs.

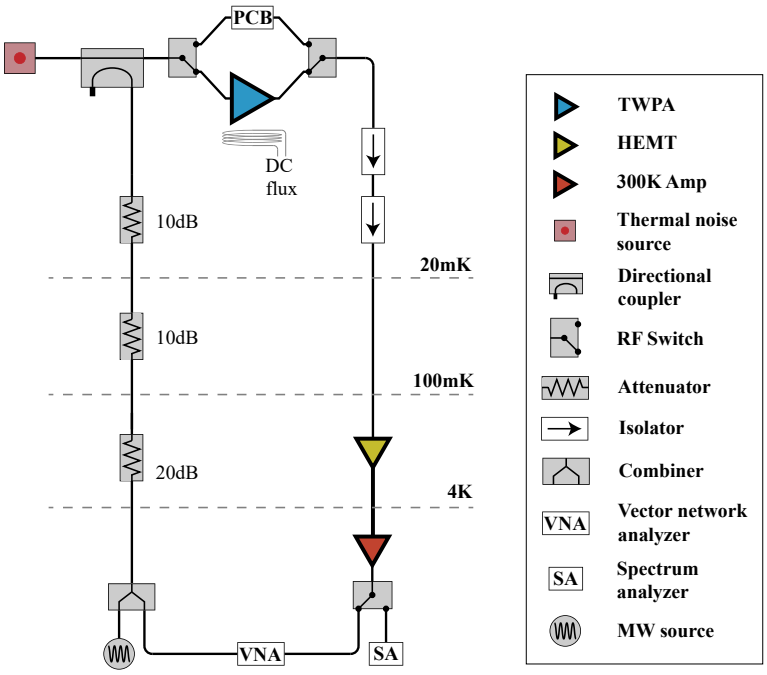

Figure 5.1: Sketch of the experimental setup.

At room temperature, the output of a vector network analyzer (VNA) was combined with that of a microwave source (used to pump the device), to be fed into the input of the cryostat. At the output of the cryostat, a microwave switch was used to direct the amplified signal towards either the VNA or the spectrum analyzer.

5.2 THE DEVICE

The Josephson meta-material device designed for use as a reversed-Kerr amplifier consists of 700 SNAIL cells. Each cell spans about 6 mm and contains a loop with three large (high critical current, I_o) and one small (low critical current, rI_o) Josephson junctions in either arm. The cells also feature fin-like capacitive pads to fix the impedance of the transmission line to 50 Ω. The SNAIL cells were fabricated with alternating flux polarity to suppress three-wave mixing processes, as discussed in chapter 2. Fig 5.2 depicts a circuit schematic of the reversed-Kerr TWPA.

Back to contents

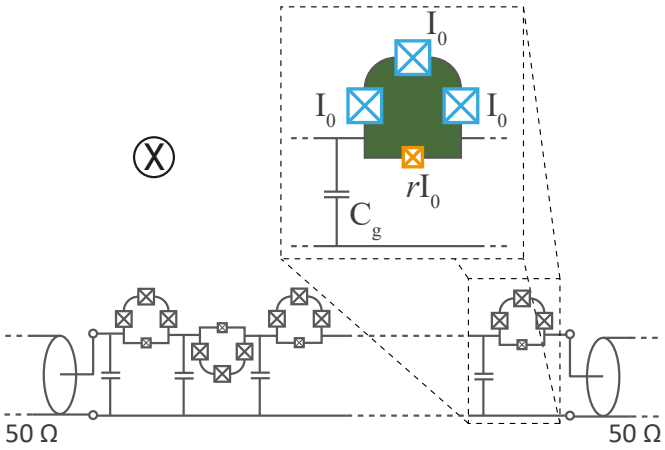

Figure 5.2: Circuit schematic of the reversed-Kerr TWPA; I_o is the critical current of the large junction, rI_o is the critical current of the small junction and C_g is the ground capacitance per unit cell. Global magnetic field is used to tine the nonlinearity to optimal value. The alternated loop geometry results in an alternated magnetic flux polarity, suppressing three-wave mixing processes.

5.3 LINEAR CHARACTERIZATION OF THE MEDIUM

Before we can explore the alluring regime of nonlinear behavior exhibited by the device, it is important to characterize it in the linear regime, i.e., with probe powers low enough to avoid activation of nonlinear processes. To facilitate these characterizations in-situ, we included a bypass (dummy) device, as mentioned in the previous section. The bypass has identical packaging to that of the actual device, with the substrate chip containing the device replaced by a coplanar waveguide (CPW) on a printed circuit board (PCB) with copper cladding.

The PCB is effectively lossless compared to the device under investigation. This allows direct comparison of transmission through the device with that through the bypass to infer losses present in the device. Normalized transmission through the device is depicted in Fig. 5.3(a) as a function of applied flux and frequency. The two vertical cuts, corresponding to zero and half quanta of flux, are also shown in the inset. The losses through the device vary significantly with applied flux; flux-dependent electrical length and impedance of the device contribute to this

Back to contents

variation.

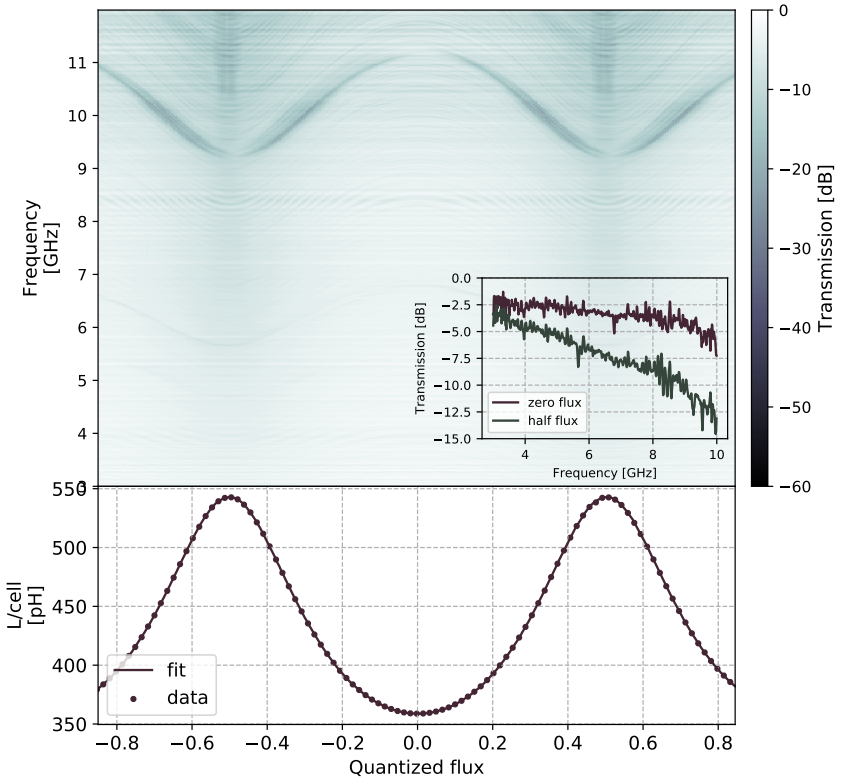

Figure 5.3: (a) Calibrated transmission through the device as function of the frequency and applied magnetic flux. (inset) Calibrated transmission through the device for two extreme flux values, $\Phi_{ext}/\Phi_0 = 0$ and $\Phi_{ext}/\Phi_0 = 0.5$. (b) Inductance L of one unit cell as function of flux obtained by fitting the dispersion relation. This can be fitted to the theoretical expression of L as a function of the external magnetic flux to obtain ratio of critical currents (r).

At the optimal flux point for reversed-Kerr phase matching, i.e., half quanta of flux through the SNAILs, we find that the transmission losses are roughly 1 dB per GHz. These values are comparable with previously demonstrated Josephson metamaterials [9, 84]. This frequency dependence of loss can be used to obtain the loss tangent of the dielectric medium and the conductor losses, which are essential for modeling the device performance. The evolution of a signal A in a lossy medium can be described as [94],

Back to contents

$$A = A_0 e^{-\alpha_d - \alpha_c}, \tag{5.1}$$

where α_d and α_c are attenuation originating from dielectric and conductor losses, respectively. For the devices discussed in this thesis, conductor loss is negligible compared to dielectric loss [84], hence, we can safely approximate losses focusing only on the dielectric,

$$\alpha_d = k \tan(\delta)/2 \tag{5.2}$$

where $\tan(\delta)$ is the loss tangent, defined as the ratio of imaginary and real parts of the permittivity of the medium. Fitting the frequency dependence of the losses, we obtain the loss tangent of the device for various powers between 2.1×10^{-3} ($\sim$100 photons) to 2.6×10^{-3} ($\sim$1 photon).

The electrical length of the bypass PCB is negligible compared to the device, as speed travels much (100x) slower in the Josephson meta-material. Thus, by comparing the transmission phase of the device with that of the bypass, we can obtain the phase acquired by the wave traveling in the device as a function of frequency. This measured phase is directly linked to the dispersion relation, $k(\omega) = \theta_{\text{device}}(\omega)/N$, where N is the number of SNAILs in the device. At a fixed applied flux, the frequency dependent phase evolution can be fitted to the linear dispersion relation,

$$\theta_{\text{device}} = \theta_0 + N \frac{\sqrt{LC_g}\,\omega}{\sqrt{1 - \frac{\omega^2}{(LC_J)}}}, \tag{5.3}$$

using the SNAIL inductance, L, as fit parameter, and fixing the other parameters with the design/fabrication values: $N = 700$, $C_g = 250$ fF and $C_J = 50$ fF. The intercept θ_0 added to the model accounts for the $2n\pi$ uncertainty introduced by phase wrapping. The fitted values of inductance can also be used to compute the plasma frequency, $\omega_J = 1/\sqrt{LC_J}$, which varies between 30.5 GHz at half flux and 37.5 GHz at zero flux.

The values of SNAIL inductance obtained for various flux points from the fits are shown in Fig. 5.3(b) (dotted curve).

Back to contents

This flux dependence of inductance can then be fitted using its expression (2.14),

$$L(\Phi_{\text{ext}}) = \frac{\Phi_0}{2\pi I_0 \widetilde{\alpha}(\Phi_{\text{ext}})}, \tag{5.4}$$

with $\widetilde{\alpha}(\Phi_{\text{ext}})$ defined in Eq. 2.12, and using the asymmetry ratio r and the critical current I_0 as fit parameters. From the best fit we obtain $I_0 = 2.19\,\mu\text{A}$ and $r = 0.07$, comparable with the values expected from design and fabrication.

5.4 GAIN SIMULATION

The amplification performance of the reversed-Kerr TWPA, ignoring noise, can be simulated using the device parameters obtained from linear characterization in the coupled differential equations describing the four wave mixing process; Eq. 4.10 and 4.11,

$$\left(\partial_x + \frac{i\Delta k}{2}\right) A_{\text{s}} = i\frac{k_{\text{i}}}{2k_{\text{s}}}\eta_{\text{s}} A_{\text{i}}^* - \kappa_{\text{s}}'' A_{\text{s}}, \tag{5.5}$$

$$\left(\partial_x - \frac{i\Delta k}{2}\right) A_{\text{i}}^* = -i\frac{k_{\text{s}}}{2k_{\text{i}}}\eta_{\text{i}} A_{\text{s}} - \kappa_{\text{i}}'' A_{\text{i}}^*. \tag{5.6}$$

These equations can be expresses in matrix form as [9, 95],

$$\hat{A}'(x) = \Phi\hat{A}(x), \tag{5.7}$$

where $\hat{A} = [A_s, A_i^*]^T$ and the coordinate x is normalized to number of SNAILs. The matrix $\Phi(x)$ is defined as follows,

$$\Phi = \begin{bmatrix} -i\frac{\Delta k}{2} - \kappa_{\text{s}}'' & i\frac{k_{\text{i}}}{2k_{\text{s}}}\eta_{\text{s}} \\ -i\frac{k_{\text{s}}}{2k_{\text{i}}}\eta_{\text{i}} & i\frac{\Delta k}{2} - \kappa_{\text{i}}'' \end{bmatrix}. \tag{5.8}$$

The solution of the matrix differential equation, eq. (5.7), can be expressed as,

$$\hat{A}(x) = S(x)\hat{A}(0)\,, \qquad S(x) = e^{\Phi x}\,. \tag{5.9}$$

Back to contents

We use the $S(x)$ matrix to numerically simulate the gain of the amplifier. The effect of pump attenuation can be approximated as a position independent amplitude reduction, resulting in reduced coupling constant, $|A_p| = A_{po} \exp\left(-\kappa_p'' N/2\right)$ [9]. It is crucial to include the transmission losses of the device into the gain modeling for accurate quantitative simulation of the gain. See appendix A.4 for a comparison between simulated gain obtained from lossless approximation and complete model accounting for dielectric losses.

5.5 4WM GAIN CHARACTERIZATION

In this section, we focus on the amplification performance of the device operated at half flux (in the reversed-Kerr regime). A key feature of the reversed-Kerr TWPA is that the pump frequency is not fixed by design and can be tuned over a large range to tune the amplification band dynamically. To demonstrate this tunability, we operate the device at three pump frequencies, 6, 8, and 10 GHz. Fig. 5.4 (a) depicts the gain profiles thus obtained, along with the gain simulated using the model described in the previous section. The gain is measured as the difference in transmission when the pump is on and when the pump is off. When a pump is applied to the device at 6 GHz, it exhibits a gain of around 15 dB over a 5 GHz combined bandwidth; when pumped at 8 GHz, it exhibits a gain of around 18 dB over a 3.5 GHz combined bandwidth; when pumped at 10 GHz, it exhibits a gain larger than 20 dB over a combined bandwidth larger than 4 GHz. Here, we mention the combined bandwidth of the two gain peaks on either side of the pump, as this is the most relevant quantity for most of the intended amplification applications. Josephson TWPAs can very efficiently convert the pump power to signal mode and hence, need low pump powers to operate. Similar pump power ($\sim$ -75 dBm) was used at the input of the TWPA to obtain optimal gain profiles at these frequencies.

The double lobe gain curves results from the fact that phase mismatch vanishes on either side of the pump, as depicted in Fig. 5.4 (b). See appendix A.3 for more details about reversed-Kerr gain profile and a comparison with the dispersion engineered gain profile. It can be noted that the gain increases at higher pump frequencies without sacrificing the bandwidth. This effect is expected, as the electrical length of the device is directly proportional to the frequency, a change further intensified by

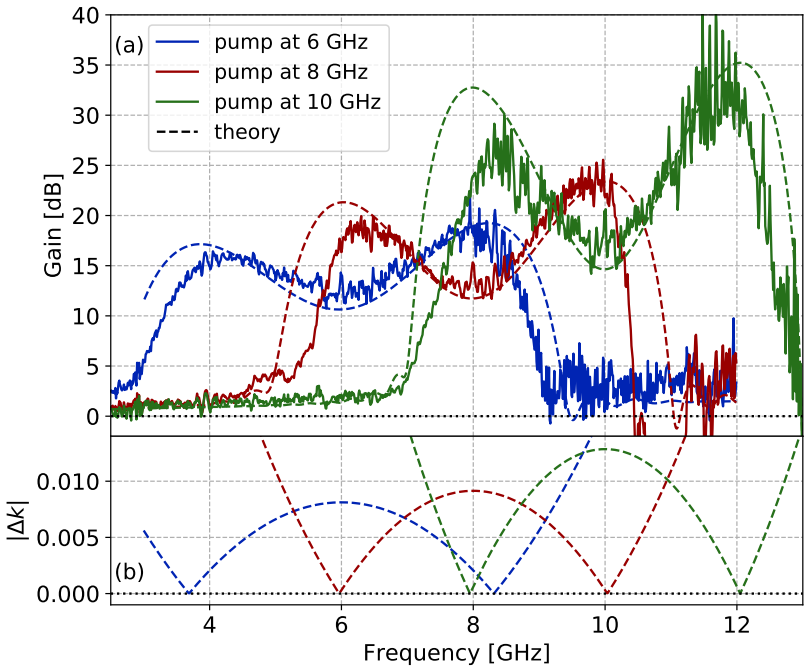

Figure 5.4: (a) Gain profiles obtained with same device pumped at 6, 8 and 10 GHz and tuned to operate at external magnetic flux $\Phi_{ext}/\Phi_o = 0.5$. Dashed lines indicate the gain simulated using the theoretical model. (b) Simulated phase mismatch corresponding to the three pump configurations. The gain is maximal when the phase mismatch vanishes.

Back to contents

the curvature of the dispersion. Thus, at higher frequencies, the effective length of the device is longer, increasing the interaction time of the modes in the amplifier leading to higher gains. The same is also evident from the form of the coupling constant η_p in reduced gain coefficient (Eq. 4.14), which has a strong dependence on pump wavevector; as wavevectors of traveling modes in the device are proportional to their frequencies, and diverge at the plasma frequency, higher gain is observed at higher frequencies.

The simulated plots corresponding to the experimental gain are plotted with dashed lines in Fig 5.4. The measured gain is in good qualitative agreement with the theoretical model. We highlight that the model has no fitting parameters but only utilizes the values of C_J (Josephson capacitance per unit cell) and C_g (ground capacitance per unit cell) obtained from design, the values of r and I_0 obtained from the device characterization in the linear regime as described in section 5.3, and the experimental values for the pump power. It can be noted that the amplification at higher frequencies for a similar pump power is consistently higher. Due to the nature of the four-wave mixing process, the gain measured at pairs of frequencies equidistant from the pump should be identical in an ideal lossless reversed-Kerr TWPA. However, in practice, the asymmetric loss experienced by modes traveling at different frequencies breaks this gain symmetry. This effect is well captured by the distributed gain model used for simulations. We highlight that this model has no fitting parameters, and it utilizes the values of C_J (Josephson capacitance per unit cell) and C_g (ground capacitance per unit cell) obtained from design, the values of r and I_0 obtained from the device characterization in linear regime (as described in section 5.3) and the experimental values for the pump power. We neglect the stray linear inductance in the transmission line, which could be one possible explanation for the narrowing of the amplification band with respect to the model predictions. To summarize, we observed a combined dynamical bandwidth[2] larger than 10 GHz with a gain higher than 15 dB, a distinguishing feature of this device. Furthermore, the reported dynamic band is limited by the measurement setup; in principle, the device can amplify over an even larger range of frequencies.

[2]Tunable bandwidth, adjusted by changing pump frequency.

Back to contents

Gain ripples

Another significant merit of the reversed-Kerr TWPA is the reduction in gain ripples, owed to the absence of dispersion engineering (and the gaps) in the transmission band, as discussed in section 4.3. Panel (a) in Fig. 5.5 compares the gain profile of the reversed-Kerr TWPA pumped at 8 GHz and an equivalent band-engineered TWPA utilizing a similar fabrication technique and pumped at 7 GHz [11]. Panel (b) in Fig. 5.5 depicts the comparison of gain variance, evaluated over 100 MHz bins, arising due to the presence of ripples. Both samples we measured using identical packaging (sample holders and connectors). Lower gain ripples also contribute to improving gain stability discussed towards the end of this chapter.

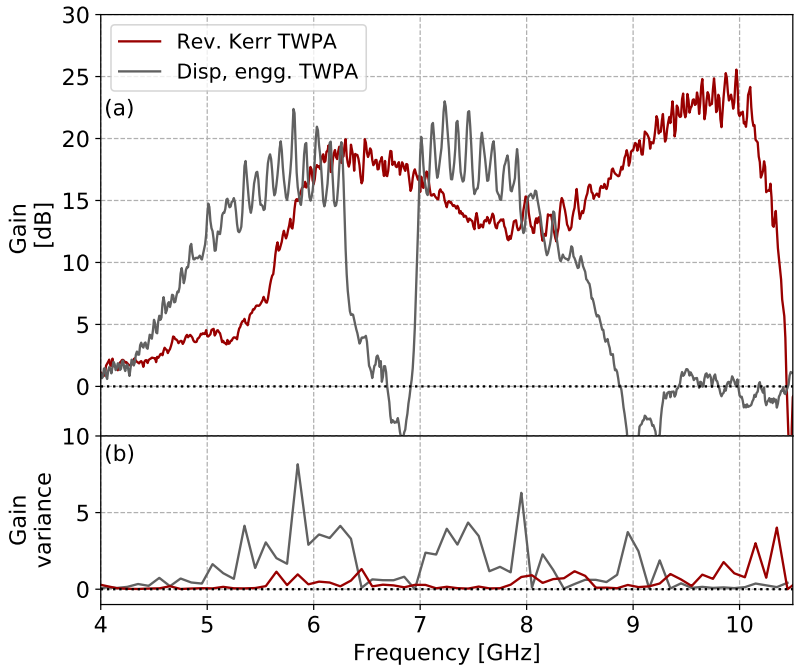

Figure 5.5: Comparison of the gain and gain variance of reversed-Kerr TWPA pumped at 8 GHz with a dispersion engineered TWPA with a stop band [11] pumped at 6.635 GHz. The variance is evaluated over bins of 100 MHz.

Back to contents

Saturation

The saturation power of an amplifier, defined as the signal power at which the gain drops by 1 dB compared to the optimal/maximum value, indicates the power handling capacity of the device. We investigated the saturation power of the reversed-Kerr TWPA by measuring the gain as a function of the input signal power. Fig. 5.6 depicts the saturation of the device when pumped at 8 GHz. We observed a 1 dB reduction in the 20 dB gain (saturation point) at signal power -97.7 $\pm$ 0.5 dBm. This is comparable to state of the art in JTWPAs [9, 11]. The microwave transmission calibration used for obtaining these results is described in the next chapter.

Josephson TWPAs are very efficient at transferring power from pump mode to signal mode. The saturation power of the amplifier is limited by the losses and the power carrying capacity of the Josephson meta-material. Improvement in both, peak gain and saturation can be achieved by reduction of losses utilizing dielectric with a lower loss tangent, for example, SiNx or a:SiH [96]. Or by increasing the power handling capacity of the device, which would involve increasing the critical current of the Josephson junctions.

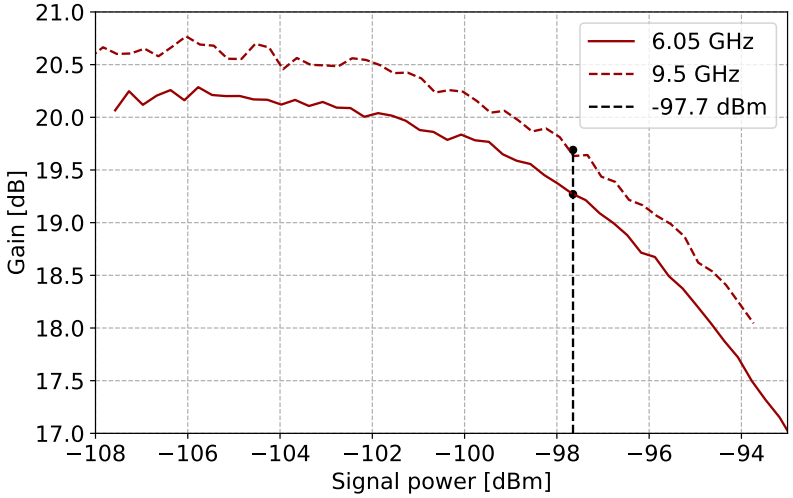

Figure 5.6: Gain as a function of input signal power at the input of the reversed-Kerr TWPA pumped at 8 GHz. The 1 dB compression of 20 dB gain for -97.7 dBm signal power is indicated with a dashed line.

Back to contents

Gain stability

The optimal operating point of reversed-Kerr TWPA corresponds to an extremum of the third-order nonlinearity with respect to the magnetic flux applied to the SNAIL loop; this makes it (g_4) and phase matching condition first-order insensitive to magnetic flux variations, offering natural protection against magnetic field instabilities. We measured time-domain gain variance between 0.5-1 dB, evaluated over 12 hours of continuous amplification as depicted in Fig. 5.7. The variance saturated to around 2 dB over measurement windows longer than 36 hours. These measurements were performed using commercially available standard microwave generators and detectors without any magnetic shielding of the device. By implementing conventional magnetic shielding, the stability can be further improved. Additionally, active feedback can also be implemented to stabilize the gain.

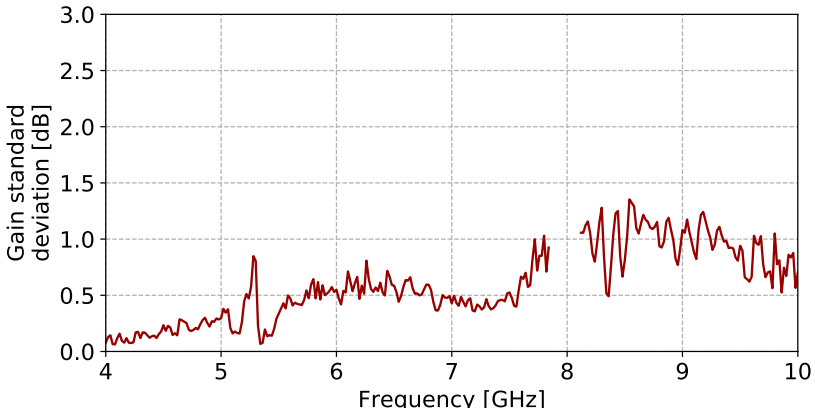

Figure 5.7: Gain variance of reversed-Kerr TWPA pumped at 8 GHz over a measurement window of 12 hours. (Measured without magnetic shielding or active feedback.)

Back to contents

6

NOISE MODELING AND CHARACTERIZATION FOR REVKERR TWPAS

The parametric amplifiers have gained wide recognition as a key element in microwave measurement setups due to their excellent noise performance. Thus, it is very important to accurately characterize the same. In this chapter, we discuss the measurement of noise added by the reversed-Kerr TWPA along with a theoretical model to describe its origins. We also present the noise performance of the whole measurement system, as this is the most relevant figure of merit for typical users, which depends upon both the noise and the gain performance of the amplifier.

6.1 DISTRIBUTED NOISE MODEL

In this section, we describe the theoretical model used for simulating TWPA noise temperature. One of the primary sources of added noise (above standard quantum limit) in an amplification chain consisting in TWPA is dielectric loss present in the device [84]. These losses arise due to the presence of a thin alumina layer, which is essential to fabricate the high capacitance needed to ensure an impedance matching between the device and the environment across the transmission line, as discussed in chapter 3. We will treat these dielectric losses as the exclusive reason for deviation from ideal performance (SQL).

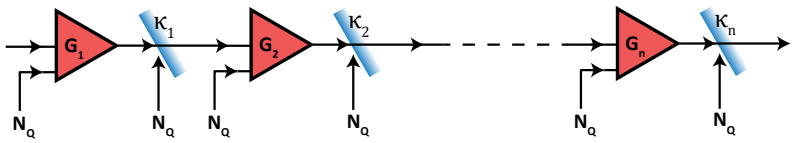

Figure 6.1: Traveling wave amplification modeled as a chain of quantum limited amplifiers with gain G_j followed by attenuators (beam-splitter) with attenuation coefficient κ_j.

We can model the TWPA as a chain consisting of small quantum-limited amplifiers with each amplifier followed by a small attenuator as depicted in Fig. 6.1. Four wave mixing amplification in such device can be described by coupled differential equations for signal and idler modes with thermal source terms accounting for losses treated as beam-splitters [95],

$$\left(\partial_x + \frac{i\Delta k}{2}\right) a_s = i\frac{k_i}{2k_s}\eta_s a_i^\dagger - \kappa_s'' a_s + \sqrt{\kappa_s''}\, a_s^{(N_Q)}, \tag{6.1}$$

$$\left(\partial_x - \frac{i\Delta k}{2}\right) a_i^\dagger = -i\frac{k_s}{2k_i}\eta_i a_s - \kappa_i'' a_i^\dagger + \sqrt{\kappa_i''}\, a_i^{\dagger(N_Q)}, \tag{6.2}$$

where $a_s^{(N_Q)}$ and $a_i^{(N_Q)}$ are noise input from the beam splitters at signal and idler modes, respectively. Similar to Eq. 5.7, we can express this in matrix form,

$$\hat{A}'(x) = \Phi\hat{A}(x) + A_0, \tag{6.3}$$

where, $\hat{A} = [a_s, a_i^\dagger]^T$, $A_0 = [\sqrt{\kappa_s''}\, a_s^{(\text{loss})}, \sqrt{\kappa_i''}\, a_i^{\dagger(\text{loss})}]^T$ and Φ is defined in Eq. 5.8. The discretized solution of the differential equation 6.3 can be expressed as,

$$\hat{A}(x) = S(x)\hat{A}(0) + \frac{1}{2\pi}\sum_x^N S(N-x)\begin{bmatrix}\sqrt{\kappa_s''}\, a_s^{(\text{loss})} \\ \sqrt{\kappa_i''}\, a_i^{\dagger(\text{loss})}\end{bmatrix}, \tag{6.4}$$

where N is the number of discretized cells in the device and $S(x)$ is the solution matrix obtained in eq. (5.9), without source terms. See appendix A.5 for derivation of Eq. 6.4. This distributed model is necessary to simulate the TWPA noise using the measured losses; however, a simplified model described next can be used to experimentally extract the noise.

We assert that it is crucial to include both signal and idler modes in the noise model whenever a broadband noise source is used for noise calibration; otherwise, the added noise could be misinterpreted to be better than the actual value by up to a factor of two [38, 97], an example depicted in Fig 6.6.

We model the TWPA as an amplifier with power gain $\widetilde{G}$ at signal/idler frequency (without accounting for losses), followed

Back to contents

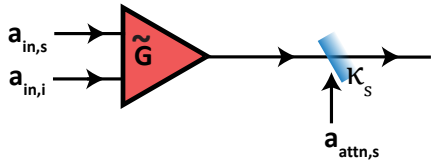

Figure 6.2: Traveling wave amplification modeled as a chain of quantum limited amplifiers with gain $\widetilde{G}$ followed by attenuators (beam-splitter) with attenuation coefficient κ.

by an attenuator with power attenuation $\kappa_{s/i}$, such that $\widetilde{G}\kappa$ is the measured gain, as depicted in Fig. 6.2. An incident field $a_{\mathrm{in,s}}$ at signal frequency, generates an amplified response $\sqrt{\widetilde{G}}\, a_{\mathrm{in,s}}$ at signal and a secondary response $\sqrt{\widetilde{G}-1}\, a^{\dagger}_{\mathrm{in,s}}$ at idler frequency. Conversely, an incident field $a_{\mathrm{in,i}}$ at idler frequency, generates an amplified response $\sqrt{\widetilde{G}}\, a_{\mathrm{in,i}}$ at idler frequency and a secondary response $\sqrt{\widetilde{G}-1}\, a^{\dagger}_{\mathrm{in,i}}$ at signal frequency. Hence, the output field at signal frequency from the amplifier section can be expressed as,

$$\bar{a}_{\mathrm{out,s}} = \sqrt{\widetilde{G}}\, a_{\mathrm{in,s}} + \sqrt{\widetilde{G}-1}\, a^{\dagger}_{\mathrm{in,i}}\,. \tag{6.5}$$

This feeds into the attenuator, at its output we get,

$$a_{\mathrm{out,s}} = \sqrt{\widetilde{G}\,\kappa_{\mathrm{S}}}\, a_{\mathrm{in,s}} + \sqrt{\widetilde{G}\,\kappa_{\mathrm{s}}}\, a^{\dagger}_{\mathrm{in,i}} + \sqrt{(1-\kappa_{\mathrm{s}})}\, a^{\dagger}_{\mathrm{attn,s}}, \tag{6.6}$$

where a_{attn} is the field originated from the attenuator (second input field in the beam-splitter model). Here we used high gain limit, i.e. $\widetilde{G} \approx \widetilde{G}-1$. It should be noted that κ_{s} is not the measured attenuation of the device, but only a modeling equivalence. Fig. 6.3 depicts noise temperature of the TWPA simulated using various models to highlight the need of distributed model described in Eq. 6.4.

6.2 NOISE MEASUREMENT SETUP

We use a technique commonly referred to as the Y-factor method to measure the noise performance of the amplifiers [98, 99]. This involves injecting two or more known noise powers at the input

Back to contents

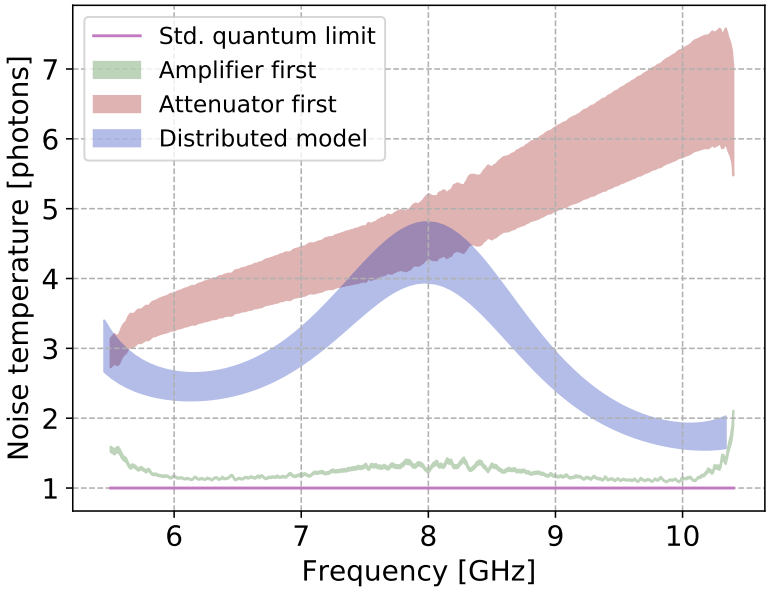

Figure 6.3: Comparison of noise temperature of the device simulated using various models using the measured loss and gain. The green range depicts the device as an amplifier followed by an attenuator. The red range depicts the device as an attenuator followed by an amplifier. And finally, the blue range depicts the noise simulated using a distributed loss model. The width of the simulations originates from uncertainty in loss measurements.

Back to contents

of the amplifier and inferring added noise by measuring the output. We used a thermal noise source (designed in-house) to generate white noise. The noise source is constructed by attaching a cryogenic compatible RF termination to a small copper plate, with weak thermal anchoring to the dilution stage of the cryostat as depicted in Fig. 6.4 panel (a).

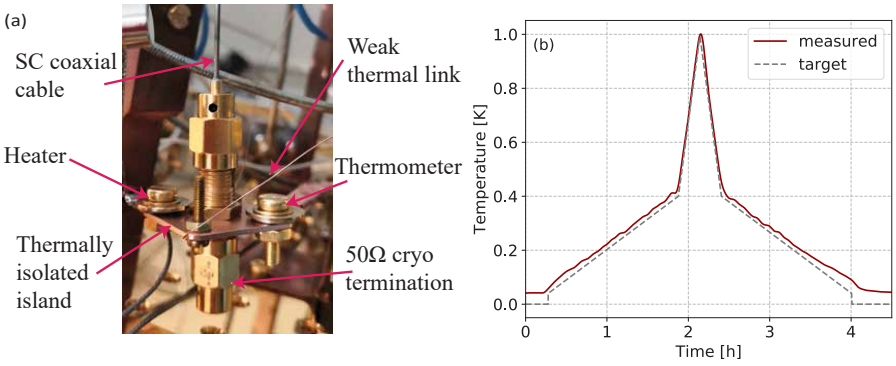

Figure 6.4: (a) The thermal noise source used for performing calibration. It consisted of a thermally isolated plate (island) with a weak thermal anchoring to the base plate of the dilution refrigerator, a heater, and a thermometer to control and measure its temperature. A 50 Ω microwave termination was mounted to this plate, and connected to the setup with a superconducting cable. (b) A typical thermal cycle of the noise source.

The resistor in the termination generates broadband thermal white noise dictated by its temperature,

$$N_{\text{source}}(\omega, T_{\text{source}}) = \frac{\hbar\omega}{2} \coth\left(\frac{\hbar\omega}{2k_B T_{\text{source}}}\right), \tag{6.7}$$

where $N_{\text{source}}(\omega, T_{\text{source}})$ is the noise emitted by the thermal noise source at frequency ω, when heated to temperature T_{source}. The noise source contains a heater and a thermometer to facilitate control over its temperature. The noise generated by the resistor is fed to the coupled port of the directional coupler (Fig. 5.1) with a superconducting coaxial cable to maintain thermal isolation. The weak thermal anchoring was designed to keep the thermal load of the noise source (heated up to 1K) well below the cooling capacity of the dilution cycle to avoid heating up other components in the measurement setup. Due to this limited

Back to contents

cooling capacity for the noise source, the warming and cooling cycle took a few hours to finish. Panel (b) in Fig. 6.4 depicts a typical thermal cycle; we performed measurements during both, ramp-up and cool-down phases to detect any hysteretic effects.

6.3 CALIBRATION OF MEASUREMENT SETUP

The Y-factor noise measurement method can determine the total (system) noise of the amplification chain. Hence, to separate the noise contribution of TWPA to the system noise, we first need to determine the noise performance of the setup without the TWPA. This can be easily accomplished by positioning the microwave switches to the bypass position before noise measurements.

To calibrate the amplification chain (excluding TWPA), we record the power spectral density (PSD) with a spectrum analyzer as a function of the temperature of the noise source over the desired frequency band. We then fit the obtained PSD to standard noise model,

$$P(\omega_s) = \{N_{\text{source}}(\omega, T_{\text{source}}) + N_{\text{out}}(\omega)\}\, G_{\text{out}}(\omega) B_w\,, \quad (6.8)$$

where, $G_{\text{out}}(\omega)$ and $N_{\text{out}}(\omega)$ are the fit parameters corresponding to the output line (excluding TWPA) gain and added noise, at frequency ω, B_w denotes measurement bandwidth, and $N_{\text{source}}(\omega, T_{\text{source}})$ is the noise emitted by the thermal noise source at frequency ω, when heated to temperature T_{source}. Fig. 6.5 depicts system noise and gain thus obtained. The system noise is mainly dominated by the contribution from the HEMT (first) amplifier.

We also use this output gain to obtain the input line attenuation by subtracting it from the round trip power transmission through the bypass, facilitating input line calibration used in chapter 5.

6.4 NOISE CALIBRATION WITH BROADBAND SOURCE

We use a broadband noise source to measure the noise performance of the parametric amplifier. Due to this broadband nature of emitted noise, the amplifier is subjected to incident photons at both signal and idler frequencies. Four-wave mixing[1] para-

[1]Same is applicable for three-wave mixing amplifiers.

Back to contents

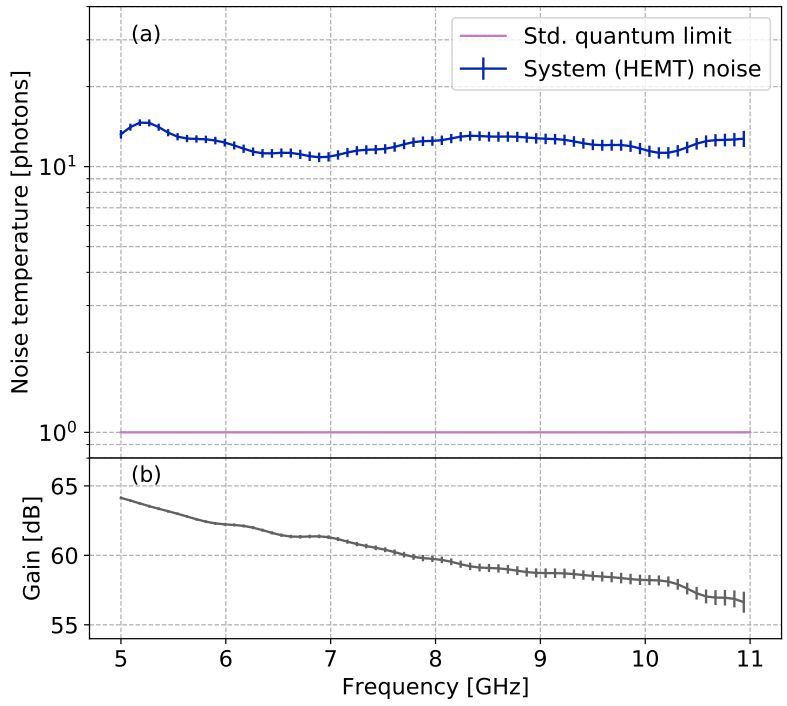

Figure 6.5: (a) Fitted noise temperature of the measurement system without TWPA (blue) compared to the standard quantum limit (SQL, purple) across amplification band in units of number of photons. (b) Corresponding gain profile (fitted).

Back to contents

metric amplifiers working in phase preserving (non-degenerate) regime couple signal and idler modes. Thus, noise incident at idler mode can result in generation of significant photons at the signal frequency and vice versa; this needs to be carefully accounted for during the noise calibration.

Using the output field from Eq. 6.6 to calculate the power spectral density and modeling a_{attn} field as the source of the added noise in the TWPA, we can express the system power output,

$$P(\omega_s) = \{N_{\text{source}}(\omega_s, T_{\text{source}})\, G_{\text{TWPA}}(\omega_s) + N_{\text{TWPA}}(\omega_s)\, G_{\text{TWPA}}(\omega_s) + N_{\text{source}}(\omega_i, T_{\text{source}})\, G_{\text{TWPA}}(\omega_i) + N_{\text{out}}(\omega_s)\}\, G_{\text{out}}(\omega_s) B_w, \tag{6.9}$$

where $N_{\text{source}}(\omega, T_{\text{source}})$ is the noise emitted by the thermal noise source at frequency ω when heated to temperature T_{source}, $G_{\text{TWPA}}(\omega)$ and $N_{\text{TWPA}}(\omega)$ correspond to the TWPA gain and input refereed added noise, $G_{\text{out}}(\omega)$ and $N_{\text{out}}(\omega)$ correspond to gain and added noise of the output line without TWPA (as measured in previous section), at frequency ω; B_w denotes measurement bandwidth.

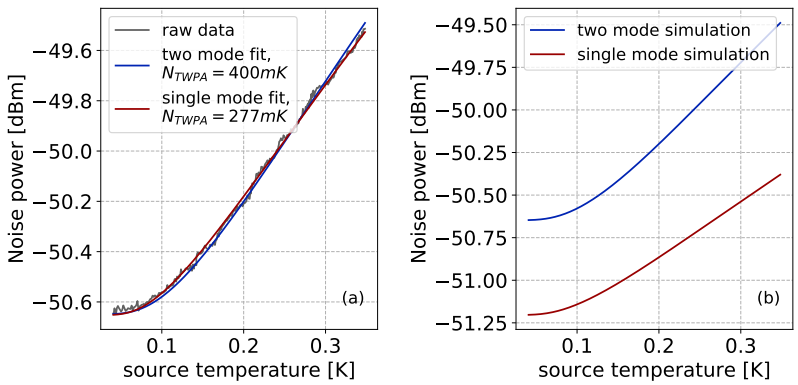

Figure 6.6: (c) Comparison between output noise power fitted to noise models including and excluding idler mode noise input. Ignoring idler mode inaccurately leads to lower noise temperature estimates. (d) Comparison of simulated noise output for the noise models including and excluding idler mode with identical TWPA noise temperature.

To further emphasize the importance of accounting for both signal and idler modes for noise calibration with broadband

Back to contents

noise source, we depict a comparison of noise temperature data at TWPA gain peak fitted to the simple single mode model, i.e. ignoring third term in Eq. 6.9 (giving $N_{\text{TWPA}} = 277$ mK) and signal-idler two mode model (giving $N_{\text{TWPA}} = 400$ mK). in Fig. 6.6. Although both the models seem to fit the data, the simple single-mode model would give an underestimated noise temperature. This error arises as the gain is misinterpreted to be higher than the actual value when only the signal mode is considered in noise fitting. Panel (b) in Fig. 6.6 depicts a comparison of simulated system output noise at the same frequency with the simple single-mode model and signal-idler two-mode model.

6.5 REVKERR TWPA NOISE PERFORMANCE

To characterize the performance of the reversed-Kerr TWPA, we pumped it at 8 GHz and recorded the input noise (thermal source) dependent PSD with a spectrum analyzer. We used this data to obtain the system noise with TWPA turned on, by fitting it to Eq. 6.8; and TWPA noise by fitting it to the signal-idler two-mode model in equation (6.9). Due to the broadband nature of the noise source and high bandwidth of the amplifier, the power emitted by noise sources reaches close to the saturation power of the amplifier for temperatures above 0.5 K. To avoid any artifacts of amplifier saturation, we limit the temperature range of the noise fit to 400 mK. The results thus obtained are shown in panel (a) of Fig. 6.7 along with the standard quantum limit for non-degenerate amplification. In panel (b), we also depict the corresponding TWPA gain. At gain peaks, the TWPA noise (blue curve) is around twice the standard quantum limit (purple line). The difference between the TWPA noise (blue curve) and the system noise (green curve) arises due to finite gain of the TWPA.

We also plot the theoretical simulation of the noise obtained by numerically solving equation (6.4). We assume good device thermalisation to 20 mK, i.e. $\langle\{a_s^{(\text{loss})}, a_s^{\dagger(\text{loss})}\}\rangle = 1/2$. As these losses are power dependent (section 5.3), we plot the theoretical simulation results as the band between low power ($\sim$1 photon) and high power losses ($\sim$100 photons). Good quantitative agreement between the measured noise and theoretical model treating losses as the source of extra noise indicates that the deviation from the standard quantum limit is primarily due to the dielectric losses present in the device. Hence, a promising avenue for improvement of noise performance can be substituting

Back to contents

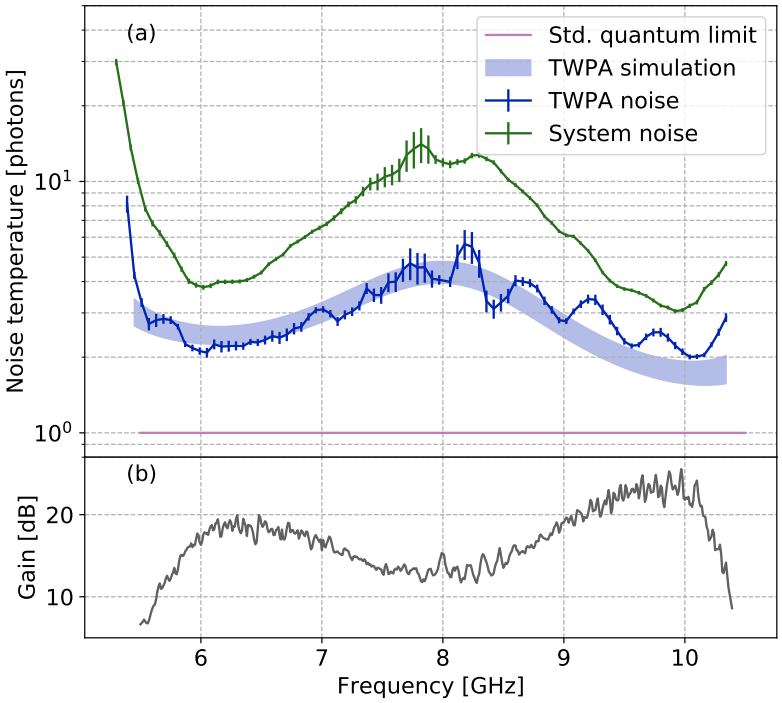

Figure 6.7: (a) Noise temperature of the system, i.e. amplification chain including TWPA (green) and the reversed-Kerr TWPA itself (blue) compared to the standard quantum limit (SQL, purple) across amplification band in units of number of photons. The device is pumped at 8 GHz and tuned to external magnetic flux $\Phi_{ext}/\Phi_o = 0.5$. The blue shadow area indicates the result of the theoretical simulations considering power dependent losses. (b) Corresponding gain profile (measured).

Back to contents

alumina with a low loss dielectric. (See chapter 9 and appendix A.1 for more details on possible avenues for improvement of noise performance.)

Back to contents

Part III

NON-CLASSICAL RADIATION

7

BROADBAND ENTANGLEMENT GENERATION

In preceding chapters, we discussed how Josephson junction based nonlinear meta-materials can be used to realize excellent broadband microwave amplifiers. Now we will depart from the use case as an amplifier to discuss how such nonlinearities can also be efficiently deployed to generate quantum (non-classical) states of microwave radiation.

These non-classical states of light have emerged as useful tools for enhancing precision measurements A broadband source of entangled radiation in microwave finds a wide array of applications ranging from potential novel implementations for quantum sensing [40, 41], quantum-enhanced detection [42], quantum teleportation with propagating waves [43] to the emerging field of quantum information with continuous variables [44–46]. Recently, methods of quantum illumination employing two-mode entangled radiation to improve the efficacy of target detection have been proposed [100–102], further widening the applications of broadband entanglement sources.

In this chapter, we will start the discussion with the squeezing of light, the potential of Josephson junction based nonlinear meta-material for generation of broadband two-mode squeezed state of microwave radiation, and finally describe a simple theoretical description for the same.

7.1 COHERENT AND SQUEEZED STATES OF LIGHT

A quantum state of light field can be described by its state variables, position (x) and momentum (p). The product of standard deviation of these conjugate variables follows the Heisenberg's uncertainty principle,

$$\Delta x \Delta p = \frac{\hbar}{2}. \tag{7.1}$$

A coherent quantum state corresponds to equal distribution of uncertainty in position and momentum quadrature (in natural units) and often exhibits dynamics closely resembling the

behavior of its classical counterpart. Deviation from this equality of uncertainties results in squeezing (and elongation) of the phase space of the state, as depicted in Fig. 7.1. This results in states exhibiting distinctly quantum behavior. The concept of squeezing the quadrature of a single-mode can be extended to multiple modes. Squeezing a two-mode state involves generating quantum correlations in the uncertainty distribution in four-dimensional phase space. This is equivalent to generation of entanglement between the two modes. (It should be noted that this does not distort the stochastic 4-sphere[1].) The squeezed state can be categorized as displaced (bright) squeezed light, when the state being squeezed is populated, resulting in radiation with a non-zero mean-field, and squeezed vacuum, when the ground state is squeezed, resulting in zero mean-field.

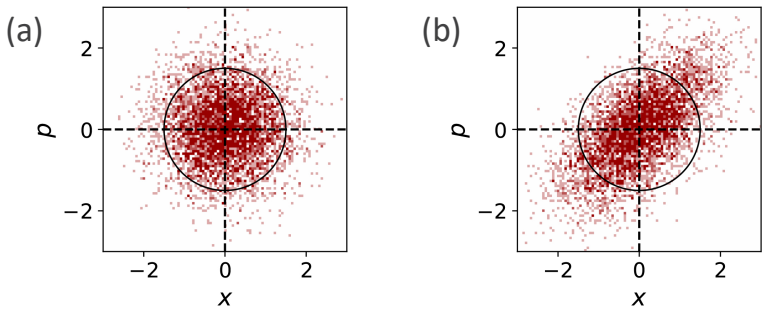

Figure 7.1: Histogram comparing (a) thermal and (b) squeezed phase space; in arbitrary units. Squeezing leads to reduction of variance in squeezing direction and increase in anti-squeezing direction, as can be seem by comparison of phase space distribution with a reference circle. This phenomenon can be implemented to reduce variance below the vacuum limit in squeezing direction.

Generation of single and two mode squeezing of microwave light has been demonstrated in resonant (narrow-band) Josephson parametric amplifiers based on resonant structures [47–54], semi infinite transmission lines via Dynamical Casimir Effect [55–57] and surface acoustic wave hybrid systems [58]. The use of Josephson junction based nonlinear meta-materials for the generation of squeezed states would have the advantage of large instantaneous bandwidth, high power, and easy customization of underlying nonlinearities, taking a significant leap towards practical application in quantum sensing and information pro-

[1] symmetry of the four dimensional phase space distribution.

Back to contents

cessing.

To present a proof-of-principle for this concept, we focus on the demonstration of two-mode vacuum squeezed radiation generation, paving the way towards the generation of complex multimode squeezing with Josephson meta-materials.

7.2 TWO-MODE SQUEEZING IN JJ META-MATERIAL

The nonlinear meta-material can exhibit both three-wave and four-wave mixing interactions. We will focus mainly on the four-wave mixing process for the generation of two-mode vacuum squeezing; however, the same can be accomplished using the three-wave mixing process. The four-wave mixing interaction term has the form,

$$H_{4\mathrm{WM}} \sim g_4(a_\mathrm{p} + a_\mathrm{p}^\dagger)^2(a_\mathrm{s} + a_\mathrm{s}^\dagger)(a_\mathrm{i} + a_\mathrm{i}^\dagger), \tag{7.2}$$

where $a_{\mathrm{p/s/i}}$ are pump/signal/idler mode operators, and g_4 is the interaction strength. We can use rotating wave approximation along with strong (classical) pump and perfect phase matching ($\Delta k \approx 0$),

$$\begin{aligned} H_{4\mathrm{WM}} &\sim g_4(a_\mathrm{p}^2 a_\mathrm{s}^\dagger a_\mathrm{i}^\dagger + a_\mathrm{p}^{\dagger 2} a_\mathrm{s} a_\mathrm{i}), \\ &\sim g_4(|A_p|^2 a_\mathrm{s}^\dagger a_\mathrm{i}^\dagger e^{2i\phi_p} + \mathrm{h.c.}), \end{aligned} \tag{7.3}$$

where $|A_p|$ is the pump amplitude and ϕ_p is phase of the pump. This interaction term can be mapped to two-mode squeezing operator,

$$\hat{S} = \exp\left(re^{i\phi} a_\mathrm{s}^\dagger a_\mathrm{i}^\dagger + \mathrm{h.c.}\right), \tag{7.4}$$

with squeezing parameter $re^{i\phi}$, where r is related to the linear gain (G_{power} in Eq. 4.13), $G = \cosh^2 r$, and ϕ is related to the phase of the pump [103, 104]. The output and input fields can be calculated using the scattering relations,

$$\begin{aligned} \hat{a}_{\mathrm{s,TMS}} &= \hat{S}^\dagger \hat{a}_{\mathrm{s,in}} \hat{S} = \cosh r\, \hat{a}_{\mathrm{s,in}} + e^{i\phi} \sinh r\, \hat{a}_{\mathrm{i,in}}^\dagger, \\ \hat{a}_{\mathrm{i,TMS}} &= \hat{S}^\dagger \hat{a}_{\mathrm{i,in}} \hat{S} = \cosh r\, \hat{a}_{\mathrm{i,in}} + e^{i\phi} \sinh r\, \hat{a}_{\mathrm{s,in}}^\dagger, \end{aligned} \tag{7.5}$$

The resulting two mode entangled state (in fock space) can be determined by application of the two-mode squeezing operator to vacuum,

Back to contents

$$|TMS\rangle = \hat{S}\,|0\rangle_s\,|0\rangle_i = \frac{1}{\cosh r}\sum_n e^{in\phi}\tanh r^n\,|n\rangle_s\,|n\rangle_i\,, \quad (7.6)$$

with the average number of photons related to the gain,

$$\begin{aligned}\bar{n} = \langle TMS|\,\hat{a}^\dagger_{\mathrm{s,TMS}}\hat{a}_{\mathrm{s,TMS}}\,|TMS\rangle &= \langle TMS|\,\hat{a}^\dagger_{\mathrm{i,TMS}}\hat{a}_{\mathrm{i,TMS}}\,|TMS\rangle \\ &= \sinh^2 r = G-1. \quad (7.7)\end{aligned}$$

The presence of losses can degrade the generation of entangled two-mode states in the meta-material, and it is necessary to account for them in the model for accurate simulations. We account for the losses with a beam splitter model as depicted in Fig. 7.2. The output field can be expressed as,

$$\begin{aligned}\hat{a}_{\mathrm{s}} &= \sqrt{\varepsilon_s}\hat{a}_{\mathrm{s,TMS}} + \sqrt{1-\varepsilon_s}\hat{a}_{\mathrm{s,N_Q}}, \\ \hat{a}_{\mathrm{i}} &= \sqrt{\varepsilon_i}\hat{a}_{\mathrm{i,TMS}} + \sqrt{1-\varepsilon_i}\hat{a}_{\mathrm{i,N_Q}}, \\ \varepsilon_s &= e^{-2\kappa''_s L}, \qquad \varepsilon_i = e^{-2\kappa''_i L},\end{aligned} \quad (7.8)$$

where $\hat{a}_{\mathrm{s,N_Q}}$ and $\hat{a}_{\mathrm{i,N_Q}}$ are noise input from the beam splitter at signal and idler modes, κ'' imaginary component of wavevector and L length of the device. We use this simplified loss model instead of the distributed loss model (discussed in section 6.1) because, in practice, the uncertainty in the measurement system calibration dominates the error bars. The asymmetry in losses present at signal and idler modes can further degrade the squeezing performance of the device [59].

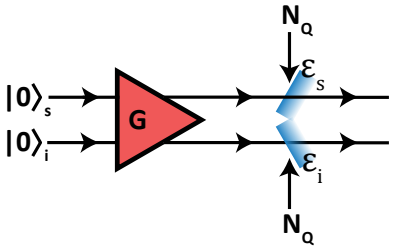

Figure 7.2: Squeezer with gain G followed by a beam splitter accounting for losses experienced by traveling modes at in signal and idler frequencies.

The (non-zero) covariances of output fields can be determined using Eq. 7.8,

Back to contents

$$\langle \hat{a}^{\dagger}_{(\mathrm{s,i})} \hat{a}_{(\mathrm{s,i})} \rangle \approx \varepsilon_{(s,i)} \sinh^2 r, \quad \langle \hat{a}_{(\mathrm{s,i})} \hat{a}^{\dagger}_{(\mathrm{s,i})} \rangle \approx \varepsilon_{(s,i)} \cosh^2 r, \tag{7.9}$$

$$\begin{aligned} \langle \hat{a}_{\mathrm{s}} \hat{a}_{\mathrm{i}} \rangle = \langle \hat{a}_{\mathrm{i}} \hat{a}_{\mathrm{s}} \rangle &\approx \frac{e^{i\phi}}{2} \sqrt{\varepsilon_s \varepsilon_i} \sinh 2r, \\ \langle \hat{a}^{\dagger}_{\mathrm{s}} \hat{a}^{\dagger}_{\mathrm{i}} \rangle = \langle \hat{a}^{\dagger}_{\mathrm{i}} \hat{a}^{\dagger}_{\mathrm{s}} \rangle &\approx \frac{e^{-i\phi}}{2} \sqrt{\varepsilon_s \varepsilon_i} \sinh 2r. \end{aligned} \tag{7.10}$$

The two mode squeezing appears as correlation between position and momentum quadratures of the signal and idler mode defined as,

$$\hat{x}_{s,i} = \frac{1}{2} \left(\hat{a}_{s,i} + \hat{a}^{\dagger}_{s,i} \right), \qquad \hat{p}_{s,i} = \frac{1}{2i} \left(\hat{a}_{s,i} - \hat{a}^{\dagger}_{s,i} \right). \tag{7.11}$$

The two mode squeezed state can be described by the four quadrature variables, x_s, x_i, p_s and p_i. Fig. 7.3 depicts the simulated distribution of the six combinations of these quadrature variables when the device is operated at 1.2 dB of gain and accounting for 1 dB of internal losses. The plots were obtained with 5000 data points for each quadrature variable with a null pump phase (ϕ). Panel (a) depicts the thermal distribution of the quadratures when the pump is off (gain $G = 1$) and (b) depicts the quadratures when the pump is turned on. The effect of the four-wave mixing process generating entangled pairs of photons shows in the correlation of position and momentum of the two modes, resulting in squeezing of the quadratures. Finally, panel (c) shows a comparison of quadrature distributions, the first four plots indicate expansion of quadrature volume due to gain, and the last two plots show asymmetric expansion, the signature of quadrature squeezing.

The amount of squeezing, or correlations of signal and idler modes, depends on the gain of the device. Fig. 7.4 shows the evolution of the squeezing as the gain of the device is increased by pumping it harder, from 1.2 dB in panel (a), 3 dB in panel (b), and to 5 dB in panel (c). The simulations were performed assuming a constant internal loss of 1 dB, with 5000 data points for each quadrature variable.

The squeezing appears as correlation between quadratures of the two modes, hence it is convenient to define collective quadratures for ease of quantification,

Back to contents

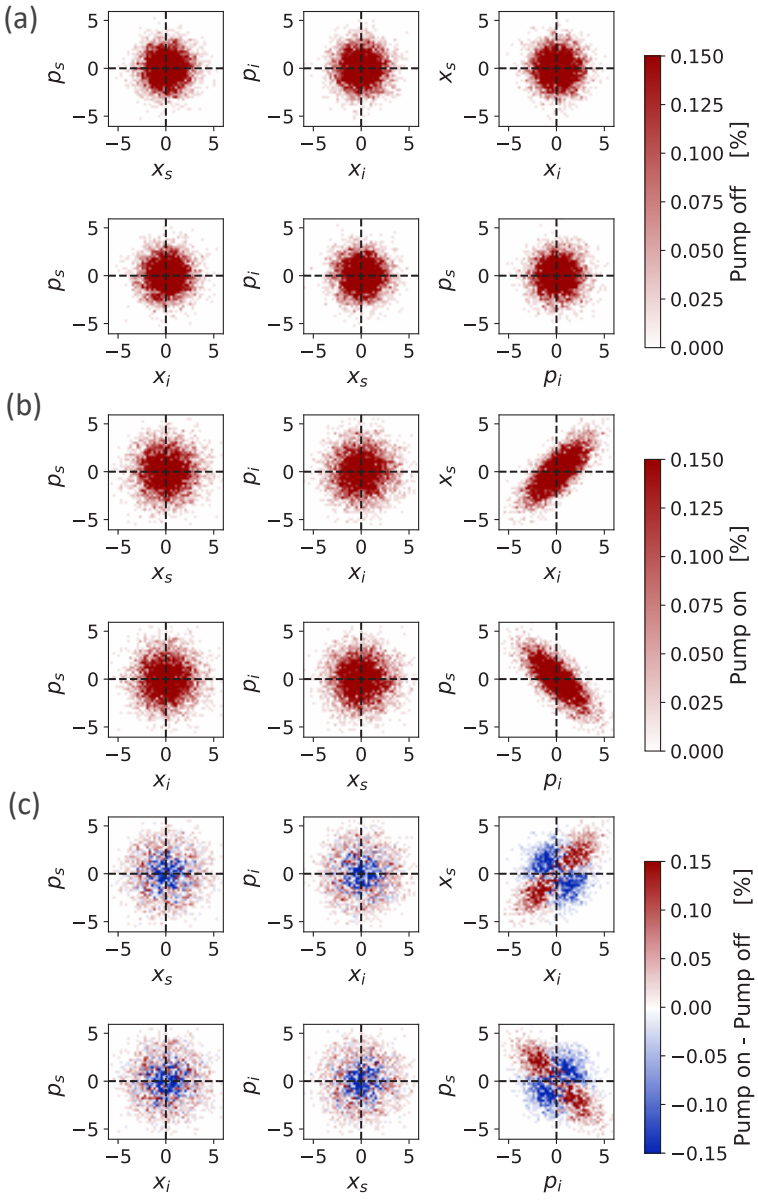

Figure 7.3: Simulated phase space distribution (2-dimensional histogram plots) at the output of the device for 5000 on/off events, (a) when the pump is off, (b) device operated at 1.2 dB gain with 1 dB of internal losses, and (c) differential distributions of the squeezed modes, i.e. difference between pump on and pump off histograms ; in units of square root of number of photons.

Back to contents

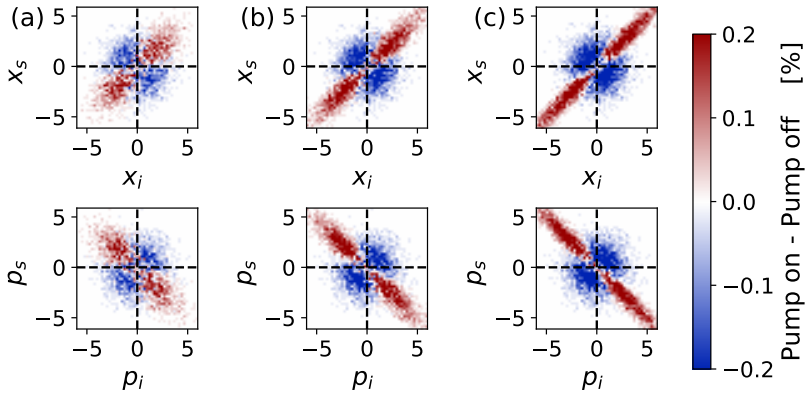

Figure 7.4: Evolution of differential quadrature distributions as a function of the device gain (a) 1.2 dB, (b) 3 dB and (c) 5 dB with 1 dB of internal losses; in units of square root of number of photons.

$$\begin{aligned} \hat{x}_+ &= (\hat{x}_s + \hat{x}_i)\ , \qquad \hat{x}_- = (\hat{x}_s - \hat{x}_i)\ , \\ \hat{p}_+ &= (\hat{p}_s + \hat{p}_i)\ , \qquad \hat{p}_- = (\hat{p}_s - \hat{p}_i)\ . \end{aligned} \tag{7.12}$$

The variance of the collective quadratures can be expressed as,

$$\begin{aligned} \langle \hat{x^2}_+ \rangle &= \frac{1}{2}\left[\varepsilon(\cosh 2r + \sinh 2r \cos\phi) + 1 - \varepsilon\right], \\ \langle \hat{p^2}_+ \rangle &= \frac{1}{2}\left[\varepsilon(\cosh 2r - \sinh 2r \cos\phi) + 1 - \varepsilon\right], \end{aligned} \tag{7.13}$$

where ε is the transmission coefficient for the two modes, assumed to be symmetric ($\varepsilon = \varepsilon_s = \varepsilon_i$), and ϕ is related to the pump phase. Comparing this to the variance of the ordinary vacuum (1/2), we can evaluate squeezing (or anti-squeezing) in decibel units,

$$Sq_{\langle x_+^2 \rangle} = 10 \log_{10}\left(\frac{\langle x_+^2 \rangle}{0.5}\right). \tag{7.14}$$

Back to contents

Fig. 7.5 depicts the evolution of the quadrature variance in panel (a), along with their squeezing and anti-squeezing relative to an ordinary vacuum state.

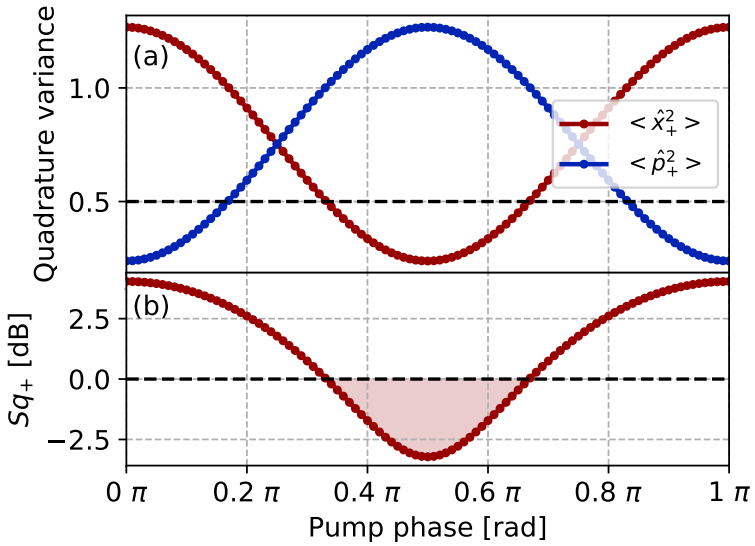

Figure 7.5: Evolution of variance of collective quadratures (a), and squeezing of the quadrature (b) as a function of the pump phase. The device is simulated with 1.2 dB of gain and accounting for 1 dB of internal losses.

7.3 QUANTIFYING THE ENTANGLEMENT

The two modes of the squeezed state described in the previous section have correlations; however, squeezing is not a measure of entanglement, i.e., the quantum nature of the correlations. In this section, we will discuss the quantification of the quantum entanglement between the two correlated modes.

The two-mode squeezed state is a Gaussian state and can be characterized by its representation with covariance matrix [48]. The elements of the 4x4 covariance matrix have form,

$$\Sigma_{mn} = 4\left(\frac{1}{2}\langle R_m R_n + R_n R_m\rangle - \langle R_m\rangle\langle R_n\rangle\right) \tag{7.15}$$

where R is the quadrature 4-vector, $R = (\hat{x}_s, \hat{p}_s, \hat{x}_i, \hat{p}_i)$. The covariance matrix can be expressed as,

Back to contents

$$\mathbf{\Sigma} = \begin{pmatrix} A & C \\ C & B \end{pmatrix}, \tag{7.16}$$

with,

$$A = \begin{pmatrix} \varepsilon_s \cosh 2r + (1-\varepsilon_s) & 0 \\ 0 & \varepsilon_s \cosh 2r + (1-\varepsilon_s) \end{pmatrix}, \tag{7.17}$$

$$B = \begin{pmatrix} \varepsilon_i \cosh 2r + (1-\varepsilon_i) & 0 \\ 0 & \varepsilon_i \cosh 2r + (1-\varepsilon_i) \end{pmatrix}, \tag{7.18}$$

$$C = \begin{pmatrix} \sqrt{\varepsilon_s\,\varepsilon_i} \sinh 2r & 0 \\ 0 & \sqrt{\varepsilon_s\,\varepsilon_i} \sinh 2r \end{pmatrix}. \tag{7.19}$$

Here we set the pump phase to zero, as it only rotates the direction of squeezing without affecting the magnitude. The normalization for the quadrature variables adopted in the above representation of covariance matrix maps ordinary vacuum states to identity matrix $\mathbb{1}_4$.

The logarithmic negativity is commonly used for quantifying the entanglement of bipartite states and can be expressed as [105],

$$E_{\mathcal{N}} = \text{Max}\left[-\ln\left(\nu_-\right), 0\right], \tag{7.20}$$

where ν_- is the simplectic eigenvalue defined as,

$$\nu_- = \sqrt{\frac{\Delta\mathbf{\Sigma} - \sqrt{(\Delta\mathbf{\Sigma})^2 - 4\,\text{det}\mathbf{\Sigma}}}{2}}, \tag{7.21}$$
$$\Delta\mathbf{\Sigma} = \text{det}A + \text{det}B - 2\,\text{det}C\,.$$

Assuming symmetric transmission ($\varepsilon = \varepsilon_s = \varepsilon_i$) the logarithmic negativity can be computed,

$$E_{\mathcal{N}} = -\ln\left[e^{-2r} + \left(1 - e^{-2r}\right)\varepsilon\right]. \tag{7.22}$$

Back to contents

The Peres–Horodecki (PPT) criterion dictates that for two states to be separable, it is necessary that the symplectic eigenvalue (ν_-) be larger than one [105]. Hence, a qualifier of non-separability or entanglement is,

$$\nu_- < 1 \qquad \text{or} \qquad E_{\mathcal{N}} > 0. \tag{7.23}$$

Fig. 7.6 depicts the evolution of logarithmic negativity as a function of the device gain, computed with 1 dB internal losses.

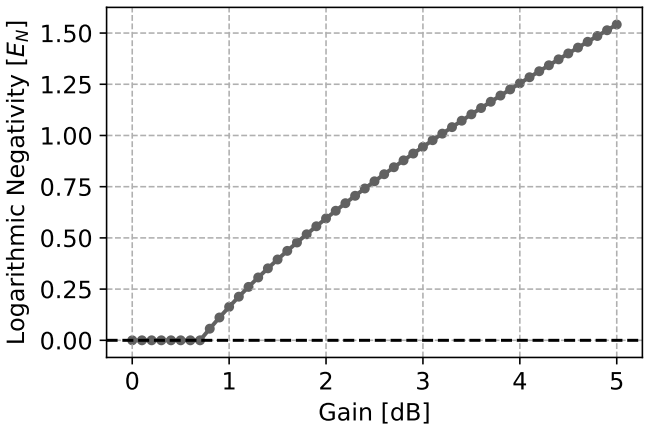

Figure 7.6: Evolution of logarithmic negativity as function of device gain, accounting for 1 dB of internal losses.

The purity of the entangled state can also be calculated from the covariance matrix,

$$\mu = \frac{1}{\sqrt{\det \Sigma}}. \tag{7.24}$$

Back to contents

8

OBSERVATION OF TWO-MODE SQUEEZING

Broadband entanglement generation in the microwave domain has recently gained traction in the scientific community as it presents a wide range of applications. Thus, a proof-of-principle experiment demonstrating its generation becomes crucial to pave the way for further developments. We will begin this chapter with the description of an optimized Josephson meta-material device designed to utilize four-wave mixing for entanglement generation, then present a broadband time-resolved measurement setup, along with its calibration, used for simultaneous measurement of the two-mode entangled microwave radiation generated by such device. And finally, we discuss the measurements, elaborating on the quantification of entanglement, followed by the stability of entanglement generation.

8.1 THE DEVICE

The Josephson meta-material device designed for use as a reversed Kerr amplifier consists of 700 SNAIL cells as described in chapter 5. This long device can provide large gain, however, it also carries significant internal losses. For a proof-of-principle demonstration of two-mode squeezing, very high gain is not required, and large losses can be very detrimental [59]. Following the simple simulations described in chapter 7, we reduced the length of the device to 250 SNAIL cells to limit its internal loss to around 1 dB. Such shorter device can exhibit gain up to 10 dB, which is sufficient to observe squeezing and quantify entanglement.

We used the methods described in chapter 5 for the linear characterization of the device. From the best fit we obtained $I_0 = 1.5\,\mu$A and $r = 0.05$, comparable with the values expected from design and fabrication. The Josephson capacitance per unit cell is $C_J = 31$ fF, while the ground capacitance per unit cell is $C_g = 550$ fF. The small deviation in these parameters from those reported for amplifier devices arises as a result of ordinary fabrication optimization. We found the internal loss of the device between 0.5 and 1 dB in the 4-6 GHz frequency range.

Form this we estimate loss tangent ($\tan \delta_0$) to be approximately 1.6×10^{-3}.

8.2 THE EXPERIMENTAL SETUP

A schematic of the experimental setup is shown in Fig 8.1. The device is anchored to the coldest plate of a dilution refrigerator (SionludiXL, introduced in chapter 5), which cools down to 20 mK. The input line contains attenuators placed at various temperature stages of the cryostat to gradually cool down the microwave environment presented by the transmission line. At the base plate (20 mK), a directional coupler is used to connect the device with a shot noise tunnel junction (SNTJ) noise source at the direct injection port and input line at the (20 dB) isolated port. Microwave switches were employed to switch between the device and a bypass for in-situ linear characterization of the device and calibration of system gain. The output line is decoupled from higher temperatures in the frequency band of interest using isolators to avoid attenuation and maintain a higher signal-to-noise ratio (SNR). The first amplifier in the measurement setup, a high electron mobility transistor (HEMT) amplifier, rests at the 4K stage of the cryostat and is followed by low noise amplifiers at room temperature. A superconducting coil is mounted to the device holder allowing control over magnetic flux threading the SNAILs.

The thermal noise source used for amplifier characterization (chapter 6) takes several hours for a calibration cycle due to the slow thermalization needed to minimize its impact on the rest of the cryogenic setup. An SNTJ, on the other hand, can be operated at a much faster rate as its output noise level is controlled by applying a voltage across it. Thus, we made a conscious choice to replace the high-performance thermal noise source with an SNTJ noise source to allow real-time system calibration[1]. The SNTJ was provided by our collaborators at NIST, Boulder, USA. A low noise DC line with filtering was installed to control the noise emitted by SNTJ by applying a voltage across it, as depicted in Fig. 8.1.

[1] In our setup, we could perform amplifier calibration in a few minutes with an SNTJ, in contrast to a thermal source that required several hours for a thermal cycle.

Back to contents

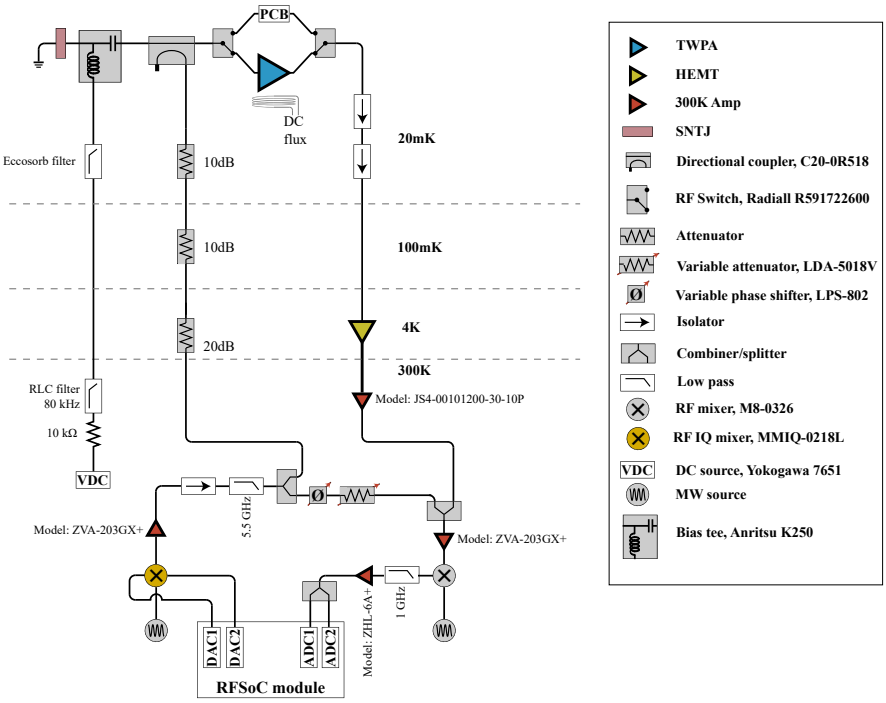

Figure 8.1: A schematic of the experimental setup.

Room temperature measurement setup

The presence of the pump tone leads to broadband generation of entangled pairs of photons across the bandwidth of the device. We need to simultaneously record two frequencies forming the signal-idler pair on either side of the pump, as depicted in Fig. 8.2 (a). A typical time-domain measurement sequence for the experiment is depicted in Fig. 8.2 (b). One measurement cycle consists of two states of the device, with and without the presence of the pump tone. The pump-off measurement provides the noise background of the measurement system.

The pump pulse is generated using an IQ mixer fed with a local oscillator from a standard RF source (f_{LO}), and I and Q pulses are generated using an FPGA module at an intermediate frequency ($f_{\text{pump-IF}}$). We used the lower side-band of the IQ mixer,

$$f_{\text{pump}} = f_{\mathrm{LO}} - f_{\text{pump-IF}}. \tag{8.1}$$

The output from the device contains significant power in pump mode, which can blind the sensitive detection chain needed to detect low-power entangled signal and idler modes.

Back to contents

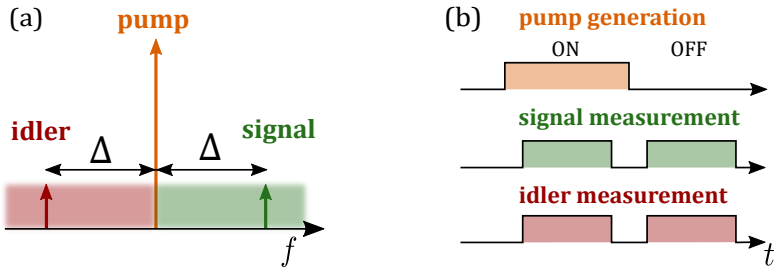

Figure 8.2: (a) Generation of signal idler pairs across the bandwidth of the device due to presence of the pump. (b) A schematic of the pumping and measurement sequence.

We implemented an interferometric setup to avoid this problem, as depicted in Fig. 8.1. The output from the IQ mixer is split into two parts, one going towards the device and the other passing through a digitally controlled phase shifter followed by an attenuator before recombination with the output of the cryostat.

Two-step demodulation of the microwave output is implemented for the measurement. [106]. The amplified output from the device is down-converted with a lower side-band (LSB) mixer fed with a local oscillator at frequency f_{LO}. This converts it to an intermediate frequency band with f_{pump} in the middle. We split the output of the LSB mixer into two paths[2], digitize with two analog to digital converters (ADCs), and finally digitally down convert from the intermediate frequency to the quadratures.

At the heart of this measurement setup is the FPGA module consisting in Xilinx RF System-on-Chip (RFSoC) platform. The RFSoC platform includes a Field Programmable Gate Array (FPGA) along with 8 Analog to Digital Converters (ADCs) and 8 Digital to Analog Converters (DACs) operating at 2 GS/s sampling rate. The RF front-end hardware and the firmware for the module were developed at the electronic workshop of Institute Neel. We limit the measurement frequency at the ADCs below 500 MHz to acquire at least four data points per cycle (with a 2

[2]We need to split the output into two paths due to limitation of our present FPGA firmware, which does not allow multi-frequency digital down-conversion at a single ADC.

Back to contents

Gs/s acquisition rate).

The gain of the device (G) can also be measured using the same setup. For this, we need to inject a weak tone at the signal frequency ($f_s = f_p + \Delta$) along with the strong tone at the pump frequency f_p. Which can be easily accomplished by including a weak signal intermediate frequency ($f_{\text{signal-IF}}$) component along with the pump intermediate frequency ($f_{\text{pump-IF}}$) pulses generated with DACs,

$$f_{\text{signal}} = f_{\text{LO}} - f_{\text{signal-IF}}. \tag{8.2}$$

The output power at the signal frequency can then be measured (by using the two-step demodulation described above) when the pump is on and when it is off, allowing extraction of the device gain.

More details of the RFSoC module are presented in appendix A.8. Calibration and optimization of the passive microwave components are described in appendix A.7.

8.3 SYSTEM GAIN CALIBRATION

Accurate calibration of the system gain (G_{sys}, without the device) is crucial for the reconstruction of the generated entangled quantum states. For gain measurement, we move the RF switch depicted in Fig. 8.1 to the reference (PCB) position, directly exposing the amplification chain to the SNTJ. In the low electronic temperature regime ($k_B T_e < \hbar\omega$),

$$\begin{aligned} N_{\text{source}}(\omega, V) = \frac{1}{2}\Bigg[&\frac{eV + \hbar\omega}{2k_B} \coth\left(\frac{eV + \hbar\omega}{2k_B T_e}\right) \\ &+ \frac{eV - \hbar\omega}{2k_B} \coth\left(\frac{eV - \hbar\omega}{2k_B T_e}\right)\Bigg] \end{aligned} \tag{8.3}$$

where $N_{\text{source}}(\omega, V)$ is the noise emitted to a matched load by the noise source at frequency ω, when voltage V is applied across it, and T_e is the electronic temperature of the junction. To calibrate the amplification chain, we record the power spectral density (PSD) as a function of the voltage applied to the noise source over the desired frequency band. We then fit the obtained PSD to standard noise model,

Back to contents

$$P(\omega_s) = [N_{\text{source}}(\omega, V) + N_{\text{out}}(\omega)]\, G_{\text{out}}(\omega) B_w\,, \tag{8.4}$$

where, $G_{\text{out}}(\omega)$, $N_{\text{out}}(\omega)$ and electronic temperature of the SNTJ are the fit parameters corresponding to the output line gain and added noise at frequency ω and B_w denotes measurement bandwidth. Fig. 8.3 depicts the recorded PSD as a function of the bias voltage and the corresponding best fit for a signal idler pair corresponding to the results presented in the next sections. The PSD was recorded with the RFSoC, using the measurement setup depicted in Fig. 8.1.

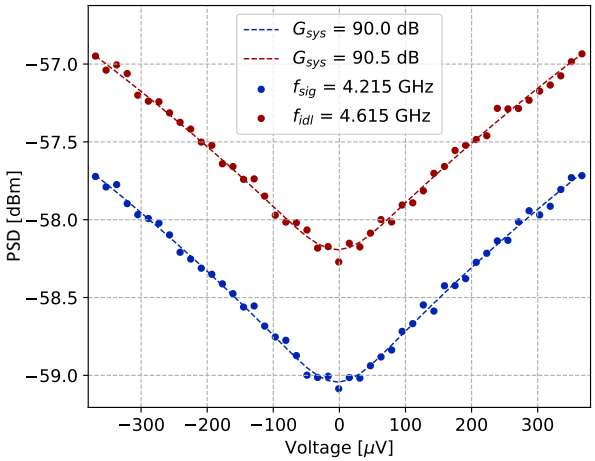

Figure 8.3: Measured PSD as a function of SNTJ voltage bias at a signal-idler pair. Best fits are shown with dashed lines. The system gain obtained by fitting is also reported in the legends.

It should be noted that the value of system gain obtained from the aforementioned method corresponds to the transmission starting from the reference plane of the SNTJ to the acquisition board (RFSoC module in Fig. 8.1). However, the normalization required for the reconstruction of squeezed states generated by the device needs to be referenced from the output of the device. Thus, it is necessary to correct for the transmission loss occurring between the SNTJ and the output of the PCB. Particularly, we need to account for insertion loss of SNTJ packaging, bias tee, directional coupler, and cryo-switch. Table 8.1 summarizes the estimated upper bound on insertion loss contributions from these components in the relevant frequency range.

Back to contents

Component	Insertion loss	Ref.
SNTJ packaging + K250 bias tee	1 dB	[107]
directional coupler C20-0R518	0.7 dB	[108]
cryo-switch Radiall R591722600	0.3 dB	[109]

Table 8.1: Upper bound on insertion loss of relevant components.

This estimation puts an upper bound of 2 dB on the total insertion loss between the SNTJ and the device. We correct the G_{sys} value obtained from the gain calibration by this upper bound loss estimation before using it for the normalization of the quadrature data. We repeated the gain calibration at regular intervals to detect any drifts or instabilities in the measurement setup.

8.4 QUADRATURE MEASUREMENT TO ENTANGLEMENT QUANTIFICATION

8.4.1 *Correlations in the quadratures*

We tune the squeezing device described in section 8.1 to the four-wave mixing flux point and pump it with a strong microwave tone at frequency f_p. This leads to generation of two-mode entangled states across the amplification band. The amplified output from the device at the signal frequency ($f_s = f_p + \Delta$) and the idler frequency ($f_i = f_p - \Delta$) is first down-converted to an intermediate frequency with the help of heterodyne setup, recorded at the ADCs of RFSoC, and finally digitally down-converted to quadrature variables at the FPGA fabric of the RFSoC module (section 8.2). These raw quadratures measured in units of volts can be converted to photons with normalization,

$$\gamma_{s,i} = \frac{\tau}{Zhf_{s,i}}, \tag{8.5}$$

where Z (50Ω) is the impedance of the microwave environment and τ is the acquisition time of the ADCs (6 μs, for the measurements presented in this chapter), as,

$$X_{s,i} = \sqrt{\gamma_{s,i}}\, X^{[V]}_{s,i} \quad , \quad P_{s,i} = \sqrt{\gamma_{s,i}}\, P^{[V]}_{s,i}. \tag{8.6}$$

Back to contents

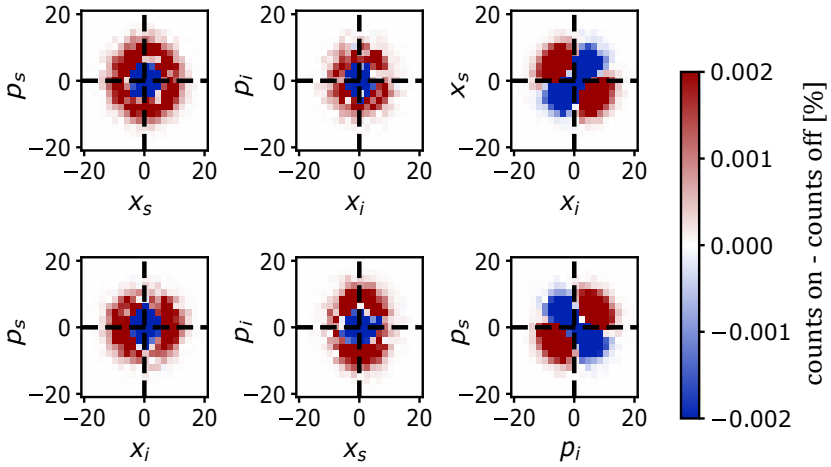

Figure 8.4: Measured quadrature phase space distribution (2-dimensional differential histogram plots: difference between pump on and pump off histograms) for 10^8 on/off acquisitions. The device was pumped at $f_p = 4.415$ GHz, and modes measured with 200 MHz detuning (Δ) from the pump. The shape of the differential quadrature distributions in the (x_i, x_s) and (p_i, p_s) phase spaces indicate presence of two-mode correlations.

Finally, we need to normalize these quadratures with the system gain (G_{sys}),

$$\bar{X}_{s,i} = \frac{X_{s,i}}{\sqrt{G_{\text{sys}}^{s,i}}} \quad , \quad \bar{P}_{s,i} = \frac{P_{s,i}}{\sqrt{G_{\text{sys}}^{s,i}}}. \tag{8.7}$$

Thus, a careful calibration of $G_{\text{sys}}^{s,i}$ is necessary for quantitative estimation of the amount of entanglement and squeezing. We use an upper bound estimation for gain (as described in section 8.3), which gives a rigorous lower bound estimation for the amount of entanglement and squeezing [64]. These quadrature variables include the thermal noise added by the amplification chain,

$$\bar{X}_{s,i} = \hat{x}_{s,i} + \hat{x}_{s,i}^{\text{th}} \quad , \quad \bar{P}_{s,i} = \hat{p}_{s,i} - \hat{p}_{s,i}^{\text{th}}, \tag{8.8}$$

where $\hat{x}_{s,i}$ and $\hat{p}_{s,i}$ are the two-mode squeezed quadratures described in Eq. 7.11. Fig. 8.4 depicts experimentally obtained quadrature histograms for detuning (Δ) of 200 MHz from the pump, constructed with 10^8 data points. The two-dimensional histograms are obtained by subtracting the histograms with

Back to contents

pump-off from the corresponding histograms with pump-on.

Back to contents

8.4.2 *Reconstructing covariance matrix*

The covariance matrices can be expressed, when the device is pumped as,

$$\Sigma_{\text{on}} = \Sigma_{\text{TMS}} + \Sigma_{\text{thermal}}, \tag{8.9}$$

and when the pump is off as,

$$\Sigma_{\text{off}} = \Sigma_{|0\rangle} + \Sigma_{\text{thermal}}, \tag{8.10}$$

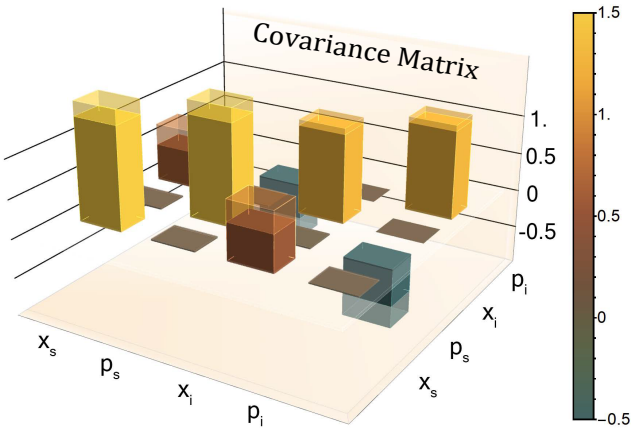

Figure 8.5: Covariance matrix reconstructed from the quadratures depicted in Fig. 8.4. Primary source of uncertainty on these covariances is uncertainty in system gain calibration. It is indicated by shaded regions, estimated using error limits on the system gain calibration. The logarithmic negativity ($E_{\mathcal{N}}$) calculated from the covariance matrix was found to be 0.4 ± 0.1, which asserts entanglement generation, i.e. quantum nature of observed correlations.

where Σ_{TMS} is the covariance matrix representing the two-mode squeezed state (Eq. 7.16) at the output of the device, $\Sigma_{|0\rangle}$ is the covariance matrix of the two ground states and is equal to identity matrix $\mathbb{1}_4$, and,

$$\Sigma_{\text{thermal}} = 2\,\text{diag}(\sigma^2_{x_s}, \sigma^2_{p_s}, \sigma^2_{x_i}, \sigma^2_{p_i}), \tag{8.11}$$

with σ^2 representing variance of the corresponding quadrature variable. The covariance matrix of the two-mode squeezed state can be thus extracted as,

Back to contents

$$\Sigma_{\text{TMS}} = \Sigma_{\text{on}} - \Sigma_{\text{off}} + \mathbb{1}_4. \tag{8.12}$$

The inferred covariance matrix is depicted in Fig 8.5. The presence of non-vanishing off-diagonal elements indicates two-mode squeezing correlations between signal and idler, verifying a necessary condition for the demonstration of entanglement generation. This entanglement can be quantified by calculating the logarithmic negativity using the reconstructed covariance matrix of the squeezed state (Eq. 7.20).

8.4.3 *Quantifying squeezing*

The collective quadrature can be expressed as,

$$\begin{aligned} \hat{x}_+ &= (\hat{x}_s + \hat{x}_i)\ , \qquad & \hat{x}_- &= (\hat{x}_s - \hat{x}_i)\ , \\ \hat{p}_+ &= (\hat{p}_s + \hat{p}_i)\ , \qquad & \hat{p}_- &= (\hat{p}_s - \hat{p}_i)\ . \end{aligned} \tag{8.13}$$

Comparing this to the variance of the ordinary vacuum (1/2), we can evaluate squeezing (or anti-squeezing) in decibel units,

$$Sq_{\langle x_+^2 \rangle} = 10 \log_{10} \left(\frac{\langle x_+^2 \rangle}{0.5} \right). \tag{8.14}$$

Fig. 8.6 depicts the pump phase-dependence of the generated two-mode squeezing. By varying the pump input phase, we observe the expected periodicity of the collective quadrature variances, panel (a), and consequently of the squeezing Sq_+, panel (b). In panel (c), the experimentally obtained logarithmic negativity $E_{\mathcal{N}}$ is reported. We stress that this is a conservative lower bound estimation (an upper bound estimation for G_{sys} is considered, giving a lower bound estimation of the amount of entanglement). The gray shadow area indicates the logarithmic negativity predicted by a simple two-mode squeezing model, which takes into account the TWPA gain and the estimated losses (Eq. 7.22).

Back to contents

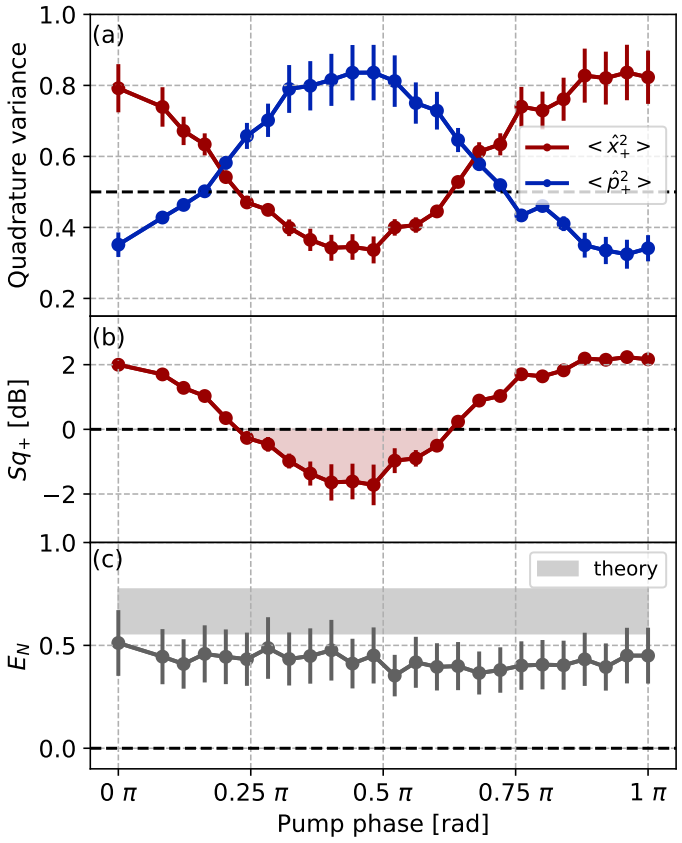

Figure 8.6: Collective quadrature variance (a), squeezing (b), and logarithmic negativity (c) as a function of the input pump phase. The device was pumped at $f_p = 4.415$ GHz, and the modes were measured with 200 MHz detuning (Δ) from the pump, with 10^7 quadrature points for each pump phase. The dashed lines indicate the reference vacuum state. Squeezing below this vacuum limit is highlighted with a shadow area in panel (b). The gray shadow area in panel (c) indicates the logarithmic negativity predicted by a simple two-mode squeezing model, which takes into account the TWPA gain and the estimated losses (Eq. 7.22).

Back to contents

8.4.4 *Broadband nature of the entanglement generation*

A key advantage in generating two-mode squeezing with traveling wave meta-materials is their broadband nature; when the pump drives the device, all the pairs of signal and idler modes within the bandwidth of several GHz get entangled. The entanglement of formation is defined as [48, 110],

$$E_F = c_+ \log_2 c_+ - c_- \log_2 c_-, \tag{8.15}$$

where,

$$c_\pm = \frac{(2^{-E_N/2} \pm 2^{E_N/2})^2}{4} \tag{8.16}$$

The broadband nature of the generated entangled states can be quantified using the rate of entangled bits generation, defined as E_F multiplied by the bandwidth. The bandwidth of the squeezing device under discussion is in the GHz range; however, we could only verify entanglement between signal and idler separated by a maximum of $2\Delta = 400$ MHz, a limitation posed by the adopted acquisition system. Using this bandwidth, we obtain a lower bound of 53 ± 20 Mebit/s (mega entangled bits per second) on the rate of entanglement generation, which is comparable with the previous state-of-the-art [57]. Fig. 8.7 depicts squeezing and logarithmic negativity as a function of detuning (Δ); we observe consistent performance across the observable bandwidth.

8.4.5 *Stability of the entanglement generation*

We verified the stability of the generated entanglement over time by performing 50 repetitions of the measurement of a set of 2×10^6 quadrature points over a total time of roughly one hour. Fig 8.8 depicts the obtained histogram distribution of the logarithmic negativity. This demonstrates that the generated entanglement is stable over a time scale of hours.

We optimized the pump power to get the maximum entanglement (maximum logarithmic negativity). This is reached for a linear gain $G = 1.30 \pm 0.05$, corresponding to a squeezing parameter $r = \operatorname{arcosh}(\sqrt{G}) = 0.50 \pm 0.04$. We experimentally observe that, for higher values of G, the inferred logarithmic

Back to contents

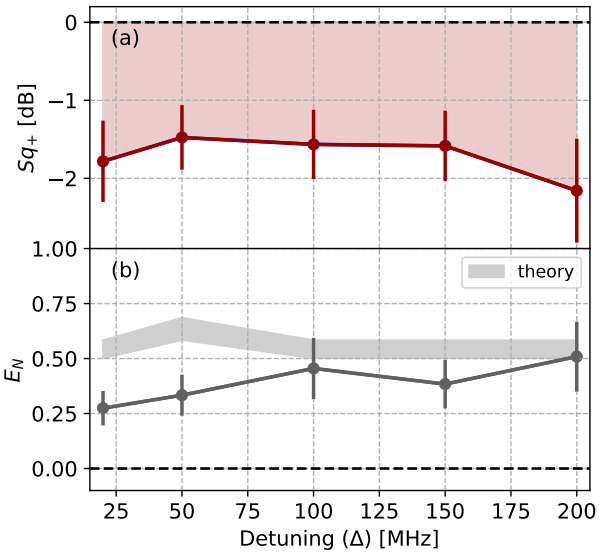

Figure 8.7: Two-mode squeezing (a) and logarithmic negativity (b) as a function of detuning (Δ). The device was pumped at $f_p = 4.415$ GHz, with 10^7 quadrature points measured for each detuning. Dashed lines indicate the vacuum state reference.

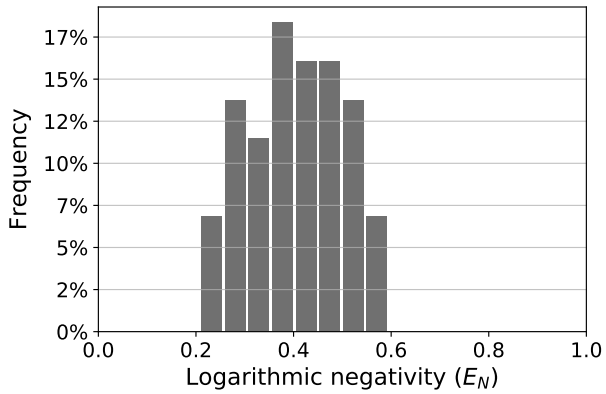

Figure 8.8: Histogram of 50 repeated entanglement measurements, each obtained from a set of 2×10^6 repeated on/off quadrature acquisitions. The device was pumped at $f_p = 4.415$ GHz, and modes measured with 200 MHz detuning (Δ) from the pump.

Back to contents

negativity and squeezing are reduced. Similar behavior has been observed in resonant Josephson parametric amplifiers [111] and semi-infinite transmission lines [57] due to the activation of spurious higher-order and wave-mixing processes. The role of such spurious processes in limiting the amount of generated squeezing in nonlinear meta-materials is currently under investigation and is briefly discussed in the prospective.

Back to contents

9 CONCLUSIONS AND PROSPECTIVES

9.1 CONCLUSIONS

Josephson junctions have emerged as a prime candidate for constructing nonlinear devices as they offer easy engineering of nonlinear properties with potentially lossless performance. For this reason, they can be used to construct traveling wave nonlinear metamaterials. Such nonlinear meta-materials have been identified as a very promising platform for superconducting quantum science & technologies and a wide range of experiments in the framework of microwave quantum optics. Their distinguishing potential resides in the ability to engineer them at sub-wavelength scales, which can allow complete control over wave dispersion and nonlinear interactions.

The work discussed in this thesis was started with the aim of developing Josephson junction based meta-material with in-situ tunability of second-order and third-order (Kerr) nonlinearities and demonstrating its efficacy as a versatile platform for microwave quantum optics experiments and applications.

We optimized the Josephson junction composites SNAILs, well-known in the superconducting circuits community, for the specific use case of building blocks for an impedance-matched nonlinear meta-material. Key optimizations include flux dependence of nonlinearities, suppression of unwanted processes, minimizing stray linear inductance, and impedance calibration to match the 50 Ω environment (Ch 2). These optimized devices were fabricated by utilizing, and building upon, the inverted fabrication, i.e., a top ground technique previously developed at the institute for easily customizable fabrication of impedance-matched nonlinear transmission lines (Ch 3).

The strong third-order (Kerr) nonlinearity exhibited by the device can be tuned from positive to negative values. To demonstrate the efficacy of this phenomenon, we have shown a use case of the meta-material as a TWPA with a new phase-matching mechanism: reversed Kerr phase matching, which utilizes the

sign reversal of the Kerr nonlinearity to correct for the dispersion curvature of such devices arising due to finite plasma frequency. The meta-material operated as reversed Kerr TWPA exhibits up to 4 GHz wide combined amplification band with 8 GHz dynamic band tunability, -98 dBm saturation (1 dB compression point) around 20 dB gain, and amplifier added noise close to the standard quantum limit. The absence of any gaps in the transmission can provide a continuous amplification band with significantly lower gain ripples in contrast to the previously demonstrated TWPAs with dispersion engineering. This engineering of the dispersion for phase matching constrains(fixes) the pump frequency by design. Use of Kerr reversal for phase matching provides in-situ tunability of the amplification band over an unprecedented range (gain larger than 15 dB is observed in the entire 4-12 GHz range) by simply changing the pump frequency.(Ch 4, 5, 6).

To demonstrate the versatility of the presented meta-materials and further emphasize their potential in the general framework of nonlinear microwave quantum optics, we investigated the generation of entanglement. Due to their large bandwidth, these devices have been identified as very promising for the generation of two-mode squeezing and broadband entanglement. With a device optimized for the generation of broadband entanglement, we observed entanglement between two modes separated by up to 400 MHz. The measured logarithmic negativity was between 0.27 and 0.51 and the collective quadrature squeezing below the vacuum limit between 1.5 and 2.1 dB (Ch 7, 8).

Although the discussions in the thesis are open-ended with a range of unanswered curiosities and potential applications to be explored, we are confident that the presented proof-of-principle results are sufficient to convince the readers of the vast potential of Josephson junction based nonlinear meta-materials in the framework of microwave quantum optics. In the next section, we highlight some of the ongoing efforts to better understand the nonlinear physics at the heart of these devices, exploring novel applications and improvement of the device performances in the aforementioned demonstrations.

Back to contents

9.2 PROSPECTIVES

9.2.1 *Three-wave mixing amplification*

The wave-mixing process utilized for amplification determines its pumping scheme. For four-wave mixing amplification demonstrated in the thesis, the pump frequency lies in the middle of the amplification band. This presents difficulties in separating the pump from the amplified signal field, causing potential detrimental effects and increasing the complexity of the measurement setup, motivating implementation of three-wave mixing amplification. Josephson TWPAs so far have only been demonstrated with the four-wave mixing scheme. The meta-materials we presented can be optimized to exhibit second-order nonlinearity, leading to three-wave mixing processes. Key challenges in realizing such an amplifier include suppression of unwanted three and four-wave mixing processes, which can be more efficient than parametric amplification. We have made significant progress in this direction by utilizing dispersion engineering for the suppression of unwanted wave mixing processes; however, this ongoing work is beyond the scope of this thesis.

9.2.2 *Effect of higher order processes on Squeezing*

For the results presented in chapter 8, we optimized the pump power to get the maximum entanglement (maximum logarithmic negativity). Which was reached for a linear gain $G = 1.30 \pm 0.05$, corresponding to a squeezing parameter $r = \text{arcosh}(\sqrt{G}) = 0.50 \pm 0.04$. We experimentally observe that, for higher values of gain (G), the inferred logarithmic negativity and squeezing are reduced. In Fig 9.1 we show an example of the experiment in which we measure gain of the TWPA, squeezing and logarithmic negativity as a function of the pump power incident at the device.

In collaboration with Sina Böhling and Anja Metelmann (KIT, Germany), we are investigating the higher-order processes which lead to the observed degradation of the quantum states with efforts to construct an analytical model. Engineering suppression of these spurious processes can lead to improvement in squeezing performance.

Back to contents

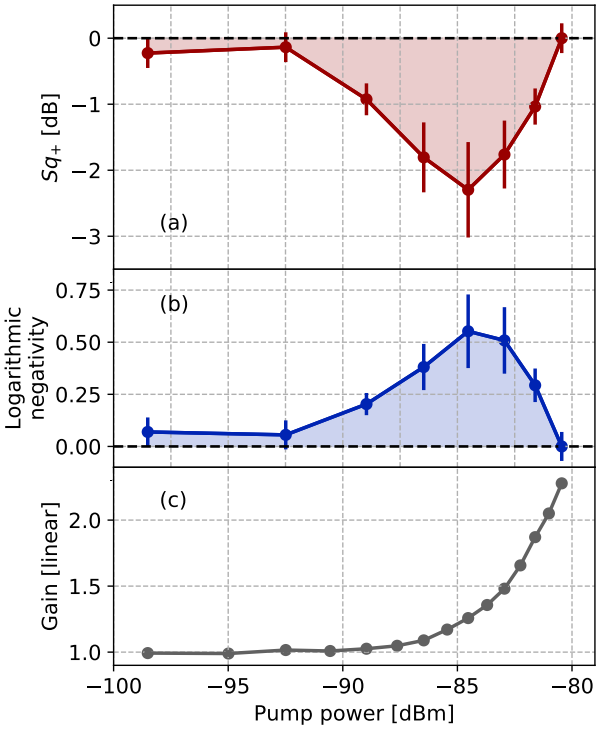

Figure 9.1: Squeezing (a), logarithmic negativity (b) and TWPA gain (c) as a function of the input pump power at the device. The squeezing and logarithmic negativity are obtained for detuning Δ = 200 MHz, $N_{\text{rep}} = 10^7$ and pump frequency $f_p = 4.415$ GHz.

9.2.3 *Modeling nonlinear behavior at high drive powers*

As evident from the previous discussions, spurious nonlinear interactions in meta-materials often lead to detrimental effects. Understanding drive-activated nonlinear processes is particularly important in applications where the meta-material is strongly driven, e.g., parametric amplification. Recently, a perturbative approach for analytically characterizing such unwanted interactions in resonant devices was presented, accounting for nonlinear AC Stark shift, drive-activated Kerr nonlinearity, and higher-order effects from the expansion of the Josephson potential [112]. We plan to pursue a similar analysis for nonlinear traveling wave meta-materials with the help of the authors of the above-cited study. In the group, the master thesis of Anuj Aggarwal (Spring 2021) was aimed towards understanding the residual spurious nonlinear processes and their drive strength dependence in traveling wave meta-materials optimized for

Back to contents

four-wave mixing amplification using WRSpice simulation tool [113].

9.2.4 *Non-destructive photon counting*

Broadband and non-destructive single-photon detectors could allow the counting of traveling microwave photons, paving the way for a wide range of new possibilities, including single-photon measurement and control in c-QED, photon-based quantum computing, precision sensing, and the detection of dark matter. Realizing a high performance broadband photon detector operating in microwave regime turns out to be a challenging task [114–119]. However, recent advances in Josephson junction based meta-materials have led to proposals of realistic implementations of non-destructive broadband photon counters [8]. These detectors utilize distributed nonlinear coupling to produce displacement in the probe field. This broadband approach can bypass two key limitations of resonant counterparts related to the quantum Zeno effect (continuous strong measurement can prevent absorption in detection cavity and displacement of the probe cavity) [120] and bandwidth-efficiency trade-offs (increasing bandwidth reduces effective interaction time, reducing efficiency) [8]. In the group, Giulio Cappelli and Gwenael Legal are currently investigating the implementation of such devices with two approaches: optimized nonlinear couplers, coupling meta-material with a probe [8], and topologically localized states in the meta-materials [121], to be populated with a probe to detect the presence of a weak field.

9.2.5 *Non-reciprocal meta-materials*

The JJ meta-materials we presented have no inherent directionality, i.e., they allow propagation of waves in both forward and backward directions. This does not present a hurdle in demonstrating amplification, as generally, the signal gets amplified only in the direction of pump propagation. However, a careful analysis of wave propagation in nonlinear materials shows that under certain conditions, modes with opposite wave vectors can also be coupled, leading to backward gain [11, 62]. Considering practical applications, this can be very detrimental to sensitive experiments and necessitates the use of bulky isolators in the setup. The development of a truly directional meta-material, with attenuation in the opposite direction, would be a

Back to contents

remarkable advancement in the field. Directional amplification in narrow-band resonant-JPAs has been successfully achieved via reservoir engineering, and multi-mode parametric interaction [122–124]. Directional isolation in Josephson transmission lines has been demonstrated by frequency conversion[125], and recently adiabatic mode conversion has also been proposed [126].

9.2.6 *Improving amplification performance*

Reaching quantum-limited noise performance in TWPAs is certainly one of the major open challenges. So far, the system noise of microwave detection chains that employ a TWPA as a first-stage amplifier has been reported to be at best two times larger than SQL [30]. For the meta-material presented in this thesis, the main hurdle in reaching quantum-limited noise performance is the presence of significant losses in the top dielectric (alumina), which leads to attenuation of propagating waves. Enhancing the quality of the dielectric is one of the main strategies to reduce losses. Dielectrics with a low number of defects, such as amorphous silicon [127] or silicon nitride [128] reported loss tangent between 10^{-6} and 10^{-5} and are promising candidates for reducing losses. Complete removal of the dielectric material and the use of vacuum gap capacitors[129] is also proposed as a strategy to drastically reduce dielectric losses. In the group, the master thesis of Ekaterina Al-Tavil (Spring 2019) [130] and Georg Monninger (Spring 2022, ongoing) are aimed at quantifying these losses, exploring better dielectrics, and improving fabrication processes to reduce dielectric losses. We briefly discuss the progress of these ongoing efforts towards optimizing dielectric performance in appendix A.1. Reduction of dielectric losses will also pave the way for implementing Josephson TWPAs at higher frequencies ($>$ 10 GHz).

In the absence of dominating losses in the meta-material, spurious higher-order processes can limit the performance of the amplification. Thus it is also important to minimize any spurious wave-mixing in the amplifier. Recently, Floquet-mode TWPAs were proposed, which encode the signals in the Floquet modes of the meta-material, which can prevent leakage of information to spurious modes and pave the way for broadband quantum-limited amplification [131]. Suppression of spurious

Back to contents

wave-mixing can also be implemented with appropriate dispersion engineering.

Optimization of the microwave packaging used for experiments discussed in this thesis is also desirable, as the current design has parasitic resonance in the amplification band. In the group, Luca Planat (a collaboration with Silent Waves) is developing the next generation of packaging for TWPAs with key improvements to the microwave connectors and geometry optimizations to the packaging to avoid any parasitic resonances near the amplification band.

Back to contents

Part IV

APPENDIX

A

APPENDIX

A.1 IMPROVING DIELECTRIC LOSSES

Silicon nitride and hydrogenated amorphous silicon are promising low-loss candidates for replacing aluminum oxide [96]. Their performance was compared to the aluminum oxide by measuring transmission through devices fabricated with them. To minimize spurious effects, these test devices were designed with unit cells containing a single Josephson junction. Aluminum oxide was deposited using atomic layer deposition (ALD), and silicon nitride and hydrogenated amorphous silicon were deposited using plasma-enhanced chemical vapor deposition (PECVD). We observed approximately factor two improvement in loss tangent of silicon nitride and hydrogenated amorphous silicon in comparison to aluminum oxide.

A.2 SIMULATION OF IMPEDANCE MISMATCH AND GAIN RIPPLES

The primary origin of gain ripples in Josephson meta-materials is their improper impedance matching with the microwave environment [132]. Fig. 4.6 depicts simulated characteristic impedance of a transmission line with and without modulation for dispersion engineering along with the gap in the transmission opened by this modulation; peak to peak gain ripple caused by this impedance mismatch in a TWPA with 20 dB forward gain is also depicted. These simulations were performed using ABCD matrix treatment of the transmission line [133]. The modulation was applied with a 10 percent amplitude on inductances and capacitances in the telegrapher model of transmission line with cell inductance of 240 pH and device length equivalent to the one used for amplification results presented in chapter 5 and 6.

The peak to peak gain ripples were obtained by comparing the constructive and destructive interference between forward propagating wave (ζ_0) and first order reflection correction (ζ_1) [132],

$$\begin{aligned} \zeta_0 &= \sqrt{G}(1-\Gamma_1)(1-\Gamma_2)A_{in}, \\ \zeta_1 &= G\Gamma_1\Gamma_2(1-\Gamma_1)(1-\Gamma_2)A_{in}, \end{aligned} \tag{A.1}$$

where G is the linear power gain, A_{in} is the input amplitude, Γ_1 and Γ_2 are reflection coefficients at input and output interface respectively.

A.3 REVERSE KERR AND DISPERSION PHASE MATCHING

A simulated comparison between reversed Kerr phase matching and traditional dispersion engineered phase matching along with the expected gain profile is depicted in Fig. A.1. Panel (a) shows $\Delta k_{\text{dispersion}}$ (blue), Δk_{Kerr} (red) and the total phase mismatch (green, sum of the two) as a function of separation of signal frequency from pump frequency. Due to reversed sign of the Kerr phase modulation, total phase mismatch vanishes at two signal frequencies, symmetrically on either side of the pump frequency; panel (b) depicts simulated gain for such phase mismatch; one can notice that the gain maxima correspond to the frequencies with optimal phase matching. Panel (c) and (d) depict the same for a dispersion engineered TWPA [11]. In this case, $\Delta k_{\text{dispersion}}$ takes a negative sign due to the presence of an engineered band gap near pump frequency.

A.4 LOSSLESS GAIN SIMULATION

A comparison between gain simulation using a lossless model (dotted curves) and the complete theory (dashed curves) is depicted in Fig. A.2. It is crucial to include the transmission losses of the device into the gain modeling for accurate quantitative simulation of the gain.

A.5 SIMULATING TWPA NOISE

Here we describe the solution for Eq. 6.3 in chapter 6. It has a form,

$$\hat{A}'(x) = \Phi\hat{A}(x) + A_0. \tag{A.2}$$

Back to contents

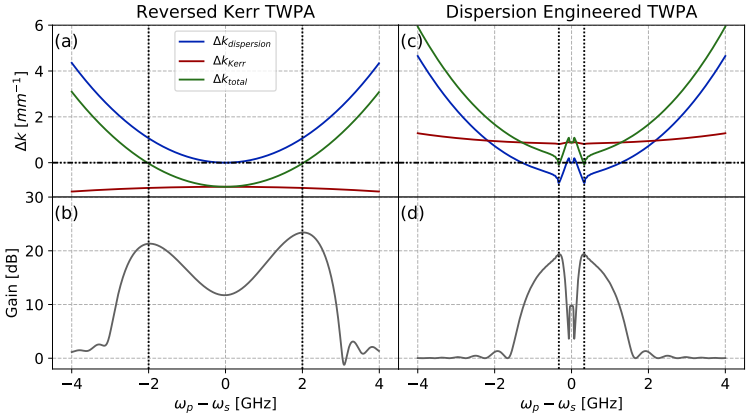

Figure A.1: Simulations of reversed Kerr phase matching and gain (a and b) compared with traditional dispersion engineering phase matching and gain (c and d). The represented Δk values are phase mismatches at the output of the devices. The simulations are performed for reversed Kerr device nominally identical to the one presented in chapters 5 and 6 and an equivalent dispersion engineered device.

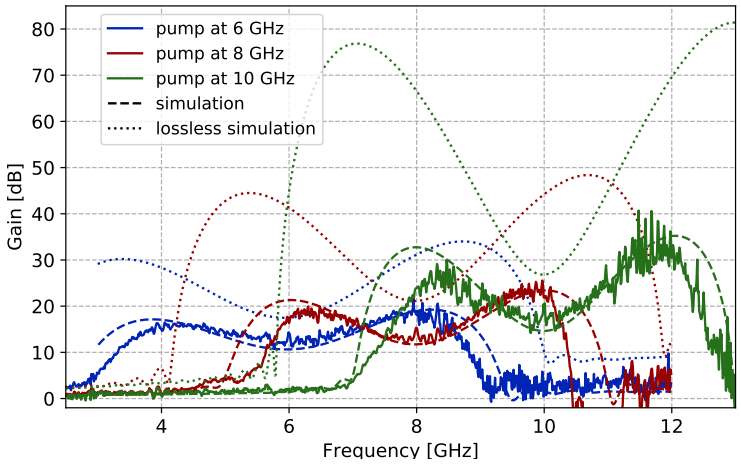

Figure A.2: Comparison between gain simulation using losseless model (dotted curves), and complete theory (dashed curves). Experimental data are indicated with continuous curves. It is crucial to include the transmission losses of the device into the gain modeling for accurate quantitative simulation of the gain.

Back to contents

We attempt ansatz of the form,

$$\hat{A}(x) = e^{\Phi x} f(x), \tag{A.3}$$

where f is some unknown general function of x. Differentiating Eq. A.3 w.r.t. x,

$$\hat{A}'(x) = \Phi e^{\Phi x} f(x) + e^{\Phi x} f'(x) \tag{A.4}$$

$$= \Phi \hat{A}(x) + e^{\Phi x} f'(x). \tag{A.5}$$

Comparing to Eq. A.2,

$$f'(x) = e^{-\Phi x} A_0 \tag{A.6}$$

$$\Rightarrow \quad f(x) = \int_0^x e^{-\Phi x'} A_0 dx' + C, \tag{A.7}$$

where C is a constant of integral defined by boundary condition. Using above expression in Eq. A.3,

$$\hat{A}(x) = e^{\Phi x} C + \int_0^x e^{\Phi(x-x')} A_0 dx'. \tag{A.8}$$

Using the initial boundary condition ($x = 0$), we get,

$$C = \hat{A}(0). \tag{A.9}$$

And,

$$\hat{A}(x) = e^{\Phi x} \hat{A}(0) + \int_0^x e^{\Phi(x-x')} A_0 dx'. \tag{A.10}$$

Eq. 6.3 is the discretized form of above equation.

A.6 GAIN SIMULATION FOR SQUEEZING DEVICE

We depict a comparison between measured and simulated gain for the device used in the squeezing experiment. The simulation was performed using the TWPA gain model discussed in chapter 5 by using device parameters determined by design and linear characterization. We highlight that this simulation does not utilize any fitting parameters and can be used for a wide range of nonlinear metamaterials.

The python classes used for these simulations are available at GitHub repository JJ metamaterial simulation [134].

Back to contents

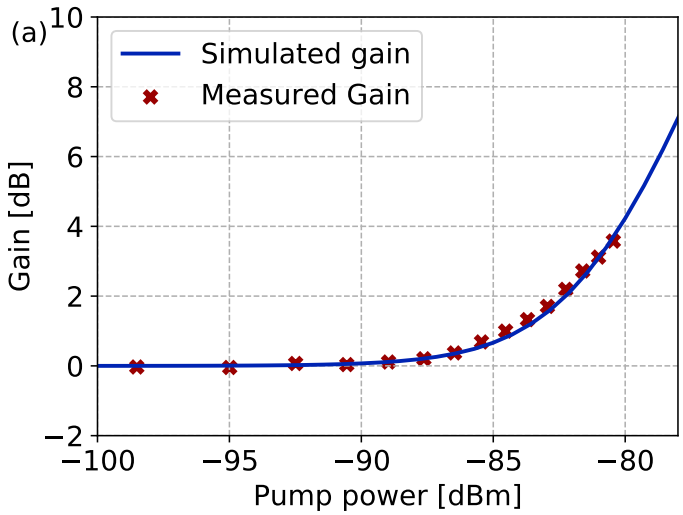

Figure A.3: Comparison of measured and simulated gain for the device used in the squeezing experiment.

A.7 MIXER CALIBRATION

We use IQ mixers in the squeezing experiment to up-convert intermediate frequency (IF) pulses generated by the RFSoC module to the operational band of the device, as discussed in chapter 8. These RF mixers can be essential tools for fast pulse generation and measurement for experiments in the microwave domain. However, a careful calibration of spurious leakage tones is imperative for sensitive experiments, like the observation of squeezing. Two primary sources of concern are leakage of the local oscillator (LO) fed to the mixer, and the presence of spurious (unused) side-band [133].

The LO leakage can be controlled by applying a DC shift to the I and Q channels. We implemented an automatic two-dimensional I/Q shift optimizer with multiple iterations to ensure LO leakage power orders of magnitude lower (typically 40 dB) than the intended tones. Spurious side-band can be minimized by calibrating the phase difference between I and Q channels. We implemented an automatic two-dimensional I/Q phase optimizer with multiple iterations to ensure side-band power orders of magnitude lower (typically 35 dB) than the intended tones.

Back to contents

For optimal efficacy of the experimental setup and to detect the presence of any drifts, we used aforementioned calibrations of the IQ mixers before each measurement run.

A.8 THE RFSOC MODULE AND ITS INTEGRATION IN THE MEASUREMENT SETUP

The RFSoC module consists in a field programmable gate array (FPGA) fabric interfaced to eight analog to digital converters (ADCs), eight digital to analog converters (DACs), and an ARM processor, as depicted in A.4. The ARM processor is programmed to host an SCPI server, which is used to communicate data and instructions to the module over TCP/IP.

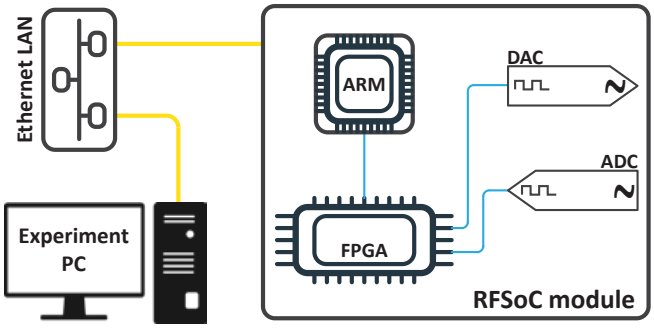

Figure A.4: Schematic representing RFSoC module and its integration in the measurement setup. The RFSoC module communicates with the experiment PC over Ethernet LAN. An ARM processor on the RFSoC module communicates with FPGA controlling the ADCs and the DACs.

The ADCs and DACs are equipped with RF front-ends suitable for microwave experiments, designed at the electronic workshop of Institute Neel. They operate at 2 Gsps sampling rate with an operating voltage range between -1 to 1 V. The ADCs sample the data at 12-bit resolution, i.e., with 0.5 mV hardware precision. And the DACs generate the waveform at 14-bit resolution, i.e., with 0.12 mV hardware precision.

The instructions for generating a waveform output at DAC or recording a signal at the ADC are first compiled on a PC as a sequence of instructions along with the necessary raw waveform data. For this, we use QCoDes, a Python-based experiment control and data acquisition framework. Fig. A.5 depicts a sim-

Back to contents

plified GUI developed to visualize the events in the sequence. The instruction sequence and data are then communicated to the SCPI server hosted on the ARM processor located in the RFSoC module over TCP/IP. The SCPI server forwards these instructions to the FPGA, which controls the operation of ADCs and DACs.

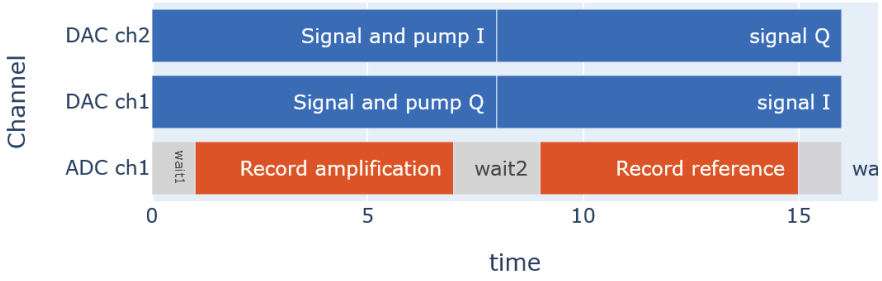

Figure A.5: Simplified RFSoC pulse sequencer GUI depicting pulses used for gain measurement. Firstly, both pump and signal tones are applied to the device and response is recorded. Then, only signal tone is applied to record transmission through the setup. Difference of these two quantities is the amplification due to the device.

When the ADCs record incoming signal, the data is forwarded to the SCPI servers and stored in a buffer memory, waiting to be transferred to the experiment control PC. In a typical squeezing measurement run, the ADCs record around two million quadrature (IQ) points per minute. This translates to a data rate of around 80 Mbps, and the buffer memory of the SCPI server runs out in a few seconds. Slowing down the repetition rate is not optimal, as it can make measurements susceptible to slow drifts in the experimental setup, on top of increasing the runtime. Hence, selecting and implementing a fast data transfer protocol was instrumental to efficiently running the measurements.

A.9 THE MICROWAVE SWITCHES AND THEIR CONTROLLER

The cryogenic measurement setup used for experiments discussed in this thesis was equipped with microwave switches mounted at the base (20 mK) plate of the cryostat. These switches allowed measurement of multiple devices and their comparison with reference device (dummy PCSs) in a single cool-down cycle. They were also instrumental in keeping the measurement

Back to contents

running during most of the COVID pandemic. Apart from these conveniences, the use of microwave switches can also help in reducing the energy consumption of the measurement setup.

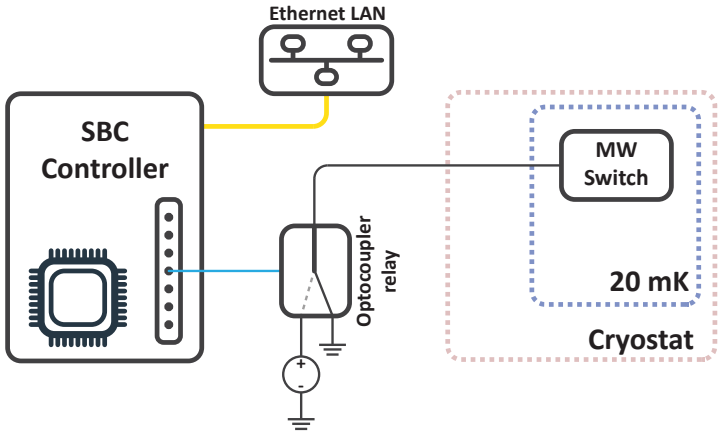

Figure A.6: Schematic of control wiring of a microwave switch, installed at base plate of the cryostat. An SBC controller connected to the Ethernet LAN sends digital switching pulses to a mechanical optocoupler relay. By default, the DC wire connected to the microwave switch is grounded; on receipt of a signal from the SBC controller, the optocoupler relay changes the connection to provide desired voltage to the microwave switch.

Fig A.6 depicts the microwave switch control schematic. Raspberry Pi, a small single-board computer (SBC) equipped with numerous general-purpose input/output (GPIO) pins, was programmed with a TCP/IP server to control the optocoupler relays. By switching the connection on the optocoupler relays, a pulse can be applied to the microwave switch. Mechanical optocoupler relays were selected (instead of solid-state devices) for this purpose to ensure complete isolation of the cryostat circuitry, avoiding any spurious heating due to leakage currents. Utilizing the millisecond control on the duration of switching pulses offered by the Raspberry Pi controller, the thermal load on the cryostat could be minimized. A typical switch operation involving two microwave switches (on either side of the device under measurement) cryostat heating of 100-150 mK was observed starting from the steady-state around 20 mK.

Contrary to popular belief, we did not observe any discernible issues arising due to the use of the microwave switches in the

Back to contents

measurement setup, counting several hundred switching operations over the past couple of years.

Back to contents

SUPERCONDUCTING CIRCUITS GROUP
@ NEEL INSTITUTE


SOAN PAPIN
SOAN PAPIN

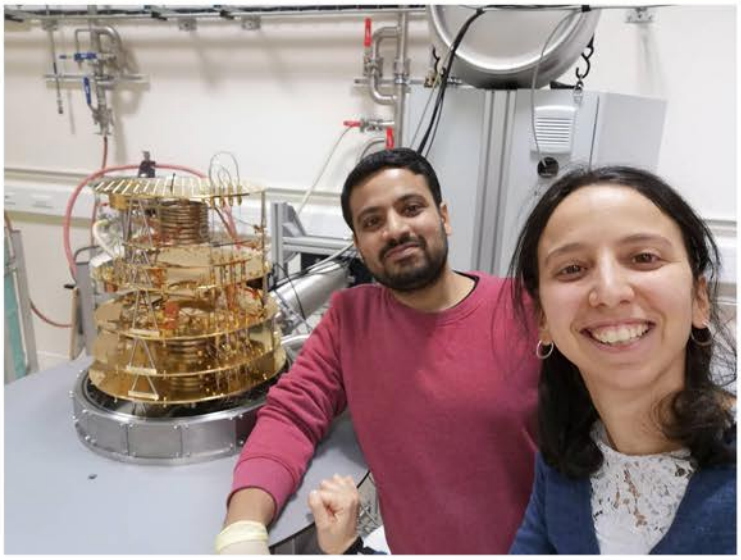

BIBLIOGRAPHY

BIBLIOGRAPHY

1. Trepanier, M., Zhang, D., Filippenko, L. V., Koshelets, V. P. & Anlage, S. M. Tunable superconducting Josephson dielectric metamaterial. *AIP Advances* **9,** 105320 (Oct. 2019).
2. Lapine, M., Shadrivov, I. V. & Kivshar, Y. S. *Colloquium* : Nonlinear metamaterials. *Reviews of Modern Physics* **86,** 1093–1123 (Sept. 12, 2014).
3. Jung, P., Ustinov, A. V. & Anlage, S. M. Progress in superconducting metamaterials. *Superconductor Science and Technology* **27,** 073001 (July 1, 2014).
4. Soukoulis, C. M. & Wegener, M. Past achievements and future challenges in the development of three-dimensional photonic metamaterials. *Nature Photonics* **5,** 523–530 (Sept. 2011).
5. Liu, Y. & Houck, A. A. Quantum electrodynamics near a photonic bandgap. *Nature Physics,* 1 –6 (Aug. 2016).
6. Mirhosseini, M. *et al.* Superconducting metamaterials for waveguide quantum electrodynamics. *Nature Communications* **9,** 3706. eprint: 1802.01708 (2018).
7. Kim, E. *et al.* Quantum Electrodynamics in a Topological Waveguide. *Physical Review X* **11,** 011015. eprint: 2005.03802 (2021).
8. Grimsmo, A. L. *et al. Quantum metamaterial for nondestructive microwave photon counting* 2020. arXiv: 2005.06483 [quant-ph].
9. Macklin, C. *et al.* A near – quantum-limited Josephson traveling-wave parametric amplifier. *Science* **350,** 307 (2015).
10. White, T. C. *et al.* Traveling wave parametric amplifier with Josephson junctions using minimal resonator phase matching. English. *Applied Physics Letters* **106,** 242601 (June 2015).
11. Planat, L. *et al.* Photonic-Crystal Josephson Traveling-Wave Parametric Amplifier. *Physical Review X* **10** (2020).
12. Macha, P, Oelsner, G, Reiner, J. M. & Marthaler, M. Implementation of a quantum metamaterial using superconducting qubits. *Nature Communications* **5,** 5146 (2014).

13. Grimsmo, A. L. & Blais, A. Squeezing and quantum state engineering with Josephson travelling wave ampli fi ers. *npj Quantum Information* **3,** 20 (2017).

14. Léger, S. *et al.* Observation of quantum many-body effects due to zero point fluctuations in superconducting circuits. *Nature Communications* **10,** 5259 (Dec. 2019).

15. Jung, P., Ustinov, A. V. & Anlage, S. M. Progress in superconducting metamaterials. *Superconductor Science and Technology* **27,** 73001 (2014).

16. Anlage, S. M. The physics and applications of superconducting metamaterials. *Journal of Optics* **13,** 024001 (Feb. 1, 2011).

17. Lazarides, N. & Tsironis, G. Superconducting metamaterials. *Physics Reports* **752,** 1–67 (Aug. 2018).

18. Bell, M. T. & Samolov, A. Traveling-Wave Parametric Amplifier Based on a Chain of Coupled Asymmetric SQUIDs. *Phys. Rev. Applied* **4** (2015).

19. Frattini, N. E. *et al.* 3-wave mixing Josephson dipole element. *Appl. Phys. Lett* **110,** 1–5 (2017).

20. Frattini, N. E., Sivak, V. V., Lingenfelter, A, Shankar, S & Devoret, M. H. Optimizing the Nonlinearity and Dissipation of a SNAIL Parametric Amplifier for Dynamic Range. *Physical Review Applied* **10,** 1 (2018).

21. Aumentado, J. Superconducting Parametric Amplifiers: The State of the Art in Josephson Parametric Amplifiers. *IEEE Microwave Magazine* **21,** 45–59 (2020).

22. Zimmer, H. Parametric amplification of microwaves in superconduting Josephson tunnel junctions. *Appl. Phys. Lett* **10,** 193 (1967).

23. Yurke, B. *et al.* Observation of 4.2-K equilibrium-noise squeezing via a Josephson-parametric amplifier. *Phys. Rev. Lett.* **60,** 764–767 (9 1988).

24. Caves, C. M. Quantum limits on noise in linear amplifiers. *Phys. Rev. D* **26,** 1817–1839 (8 1982).

25. Movshovich, R. *et al.* Observation of zero-point noise squeezing via a Josephson-parametric amplifier. *Phys. Rev. Lett.* **65,** 1419–1422 (12 1990).

Back to contents

26. Castellanos-Beltran, M. A., Irwin, K. D., Hilton, G. C., Vale, L. R. & Lehnert, K. W. Amplification and squeezing of quantum noise with a tunable Josephson metamaterial. *Nature Physics* **4,** 929–931 (2008).

27. Bergeal, N. *et al.* Phase-preserving amplification near the quantum limit with a Josephson ring modulator. *Nature* **465,** 64–68 (2010).

28. Blais, A., Grimsmo, A. L., Girvin, S. M. & Wallraff, A. Circuit Quantum Electrodynamics. *arXiv.org*. arXiv: 2005.12667v1 [quant-ph] (May 2020).

29. Ho Eom, B., Day, P. K., Leduc, H. G. & Zmuidzinas, J. A wideband, low-noise superconducting amplifier with high dynamic range. *Nature Physics* **8,** 623–627. arXiv: 1201.2392 (2012).

30. Esposito, M., Ranadive, A., Planat, L. & Roch, N. Perspective on traveling wave microwave parametric amplifiers. *Applied Physics Letters* **119,** 120501. eprint: https://doi.org/10.1063/5.0064892 (2021).

31. Heinsoo, J. *et al.* Rapid High-fidelity Multiplexed Readout of Superconducting Qubits. *Phys. Rev. Applied* **10,** 034040 (3 2018).

32. Kundu, S. *et al.* Multiplexed readout of four qubits in 3D circuit QED architecture using a broadband Josephson parametric amplifier. *Applied Physics Letters* **114,** 172601. eprint: https://doi.org/10.1063/1.5089729 (2019).

33. Burkard, G., Gullans, M. J., Mi, X. & Petta, J. R. Superconductor–semiconductor hybrid-circuit quantum electrodynamics. *Nature Reviews Physics* **2,** 129–140 (2020).

34. Zobrist, N. *et al.* Wide-band parametric amplifier readout and resolution of optical microwave kinetic inductance detectors. English. *Applied Physics Letters* **115,** 042601 (July 2019).

35. Caldwell, A. *et al.* Dielectric Haloscopes: A New Way to Detect Axion Dark Matter. *Phys. Rev. Lett.* **118,** 091801 (9 2017).

36. Bartram, C. *et al.* Dark Matter Axion Search Using a Josephson Traveling Wave Parametric Amplifier. arXiv: 2110.10262 [hep-ex] (2021).

37. Boyd, R. W. *Nonlinear Optics* 3rd (Academic Press, Inc., 2008).

Back to contents

38. Malnou, M. *et al.* Three-Wave Mixing Kinetic Inductance Traveling-Wave Amplifier with Near-Quantum-Limited Noise Performance. *PRX Quantum* **2,** 010302 (1 2021).

39. O'Brien, K., Macklin, C., Siddiqi, I. & Zhang, X. Resonant phase matching of josephson junction traveling wave parametric amplifiers. *Physical Review Letters* **113,** 1–5. arXiv: 1406.2346 (2014).

40. Degen, C. L., Reinhard, F. & Cappellaro, P. Quantum sensing. *Rev. Mod. Phys.* **89,** 035002 (3 2017).

41. Danilin, S. & Weides, M. Quantum sensing with superconducting circuits. arXiv: 2103.11022 (2021).

42. Backes, K. M. *et al.* A quantum enhanced search for dark matter axions. *Nature* **590,** 238–242 (2021).

43. Fedorov, K. G. *et al.* Experimental quantum teleportation of propagating microwaves. arXiv: 2103.04155 (2021).

44. Braunstein, S. L. & van Loock, P. Quantum information with continuous variables. *Reviews of Modern Physics* **77,** 513 (2005).

45. Weedbrook, C. *et al.* Gaussian quantum information. *Reviews of Modern Physics* **84,** 621–669 (2012).

46. Hillmann, T. *et al.* Universal Gate Set for Continuous-Variable Quantum Computation with Microwave Circuits. *Physical Review Letters* **125** (2020).

47. Eichler, C. *et al.* Observation of two-mode squeezing in the microwave frequency domain. *Physical Review Letters* **107,** 1–5 (2011).

48. Flurin, E., Roch, N., Mallet, F., Devoret, M. H. & Huard, B. Generating entangled microwave radiation over two transmission lines. *Physical Review Letters* **109,** 1–5 (2012).

49. E. Flurin, N. Roch, J. D. Pillet, F. Mallet, B. H. *et al.* Superconducting Quantum Node for Entanglement and Storage of Microwave Radiation. *Physical Review Letters* **114,** 1–5 (2015).

50. Menzel, E. P. *et al.* Path entanglement of continuous-variable quantum microwaves. *Physical Review Letters* **109,** 1–4 (2012).

51. Ku, H. S. *et al.* Generating and verifying entangled itinerant microwave fields with efficient and independent measurements. *Physical Review A* **91,** 42305 (2015).

Back to contents

52. Fedorov, K. G. *et al.* Displacement of Propagating Squeezed Microwave States. *Phys. Rev. Lett.* **117** (2016).

53. Fedorov, K. G. *et al.* Finite-time quantum entanglement in propagating squeezed microwaves. *Scientific Reports* **8,** 1–6 (2018).

54. Westig, M. *et al.* Emission of Nonclassical Radiation by Inelastic Cooper Pair Tunneling. *Physical Review Letters* **119** (2017).

55. Forgues, J. C., Lupien, C. & Reulet, B. Experimental violation of bell-like inequalities by electronic shot noise. *Physical Review Letters* **114,** 130403 (2015).

56. Wilson, C. M. *et al.* Observation of the dynamical Casimir effect in a superconducting circuit. *Nature* **479,** 376–379 (2011).

57. Schneider, B. H. *et al.* Observation of Broadband Entanglement in Microwave Radiation from a Single Time-Varying Boundary Condition. *Physical Review Letters* **124,** 140503 (2020).

58. Andersson, G. *et al.* Squeezing and Multimode Entanglement of Surface Acoustic Wave Phonons. *PRX Quantum* **3,** 010312 (1 2022).

59. Houde, M, Govia, L. C. G. & Clerk, A. A. Loss Asymmetries in Quantum Traveling-Wave Parametric Amplifiers. *Physical Review Applied* **10,** 1 (2019).

60. Zhao, S. & Withington, S. Quantum analysis of second-order effects in superconducting travelling-wave parametric amplifiers. *Journal of Physics D: Applied Physics* **54,** 365303 (2021).

61. Shu, S. *et al.* Nonlinearity and wide-band parametric amplification in a (Nb,Ti)N microstrip transmission line. *Physical Review Research* **3,** 023184 (2021).

62. Peng, K. *et al.* Near-Ideal Quantum Efficiency with a Floquet Mode Traveling Wave Parametric Amplfier. arXiv: 2104.08269 (2021).

63. Ranadive, A. *et al.* A reversed Kerr traveling wave parametric amplifier. *arXiv:2101.05815v2.* arXiv: 2101.05815v2 (2021).

64. Esposito, M. *et al.* Observation of two-mode squeezing in a traveling wave parametric amplifier. *arXiv:2111.03696 [quant-ph].* arXiv: 2111.03696 (Nov. 5, 2021).

Back to contents

65. Ranadive, A. *et al.* Kerr reversal in Josephson meta-material and traveling wave parametric amplification. *Nature Communications* **13,** 1737 (2022).

66. Butseraen, G. *et al. A gate-tunable graphene Josephson parametric amplifier* Apr. 5, 2022. arXiv: 2204.02175[cond-mat,physics:quant-ph].

67. Braggio, C. *et al. An Haloscope Amplification Chain based on a Travelling Wave Parametric Amplifier* May 4, 2022. arXiv: 2205.02053[physics].

68. Knirck, S. *et al.* Simulating MADMAX in 3D: requirements for dielectric axion haloscopes. *Journal of Cosmology and Astroparticle Physics* **2021,** 034 (Oct. 1, 2021).

69. Likharev. *Dynamics of Josephson junctions and circuits (1986).djvu* ().

70. Clarke, J. & Braginski, A. I. *The SQUID Handbook Vol 1 (2004)* ().

71. Zorin, A. B. Josephson Traveling-Wave Parametric Amplifier with Three-Wave Mixing. *Physical Review Applied* **6,** 1–8. arXiv: 1602.02650 (2016).

72. Planat, L. *et al.* Fabrication and Characterization of Aluminum SQUID Transmission Lines. *Physical Review Applied* **12,** 064017 (Dec. 6, 2019).

73. Zorin, A. B. Quasi-phasematching in a poled traveling-wave Josephson parametric amplifier with three-wave mixing. *arXiv:2101.11697 [cond-mat, physics:physics].* arXiv: 2101.11697 (Jan. 27, 2021).

74. Armstrong, J. A., Blgemeergen, N, Ducuing, J & Pershan, P. S. Interactions between Light Waves in a Nonlinear Dielectric*. *Physical Review* **127** (1962).

75. Whiteley, S. Josephson junctions in SPICE3. *IEEE Transactions on Magnetics* **27,** 2902–2905 (Mar. 1991).

76. Dixon, T. *et al.* Capturing Complex Behaviour in Josephson Travelling Wave Parametric Amplifiers. *arXiv.org.* arXiv: 1912.05349v1 [cond-mat.supr-con] (Dec. 2019).

77. Zorin, A. Josephson Traveling-Wave Parametric Amplifier with Three-Wave Mixing. *Physical Review Applied* **6,** 034006 (Sept. 12, 2016).

78. Bell, M. & Samolov, A. Traveling-Wave Parametric Amplifier Based on a Chain of Coupled Asymmetric SQUIDs. *Physical Review Applied* **4,** 024014 (Aug. 21, 2015).

Back to contents

79. Frattini, N. E. *et al.* 3-wave mixing Josephson dipole element. *Applied Physics Letters* **110,** 222603 (May 29, 2017).

80. Dolan, G. J. Offset masks for lift-off photoprocessing. *Applied Physics Letters* **31,** 337–339 (Sept. 1, 1977).

81. Lecocq, F. *et al.* Novel E-beam lithography technique for in-situ junction fabrication: the controlled undercut. *Nanotechnology* **22,** 315302. arXiv: 1101.4576 (Aug. 5, 2011).

82. Puertas Martínez, J. *et al.* A tunable Josephson platform to explore many-body quantum optics in circuit-QED. *npj Quantum Information* **5,** 19 (Dec. 2019).

83. Cord, B. *et al.* Limiting factors in sub-10 nm scanning-electron-beam lithography. *Journal of Vacuum Science & Technology B: Microelectronics and Nanometer Structures* **27,** 2616 (2009).

84. Planat, L. *et al.* Fabrication and Characterization of Aluminum SQUID Transmission Lines. *Phys. Rev. Applied* **12,** 064017 (6 2019).

85. Claudon, J. *Oscillations cohérentes dans un circuit quantique supraconducteur: le SQUID dc* PhD thesis (2006).

86. Aumentado, J. Superconducting Parametric Amplifiers: The State of the Art in Josephson Parametric Amplifiers. *IEEE Microwave Magazine* **21,** 45–59 (Aug. 2020).

87. Esposito, M., Ranadive, A., Planat, L. & Roch, N. Perspective on traveling wave microwave parametric amplifiers. *Applied Physics Letters* **119,** 120501 (Sept. 20, 2021).

88. Roy, T. *et al.* Broadband parametric amplification with impedance engineering: Beyond the gain-bandwidth product. *Applied Physics Letters* **107,** 262601 (Dec. 28, 2015).

89. Planat, L. *et al.* Understanding the saturation power of Josephson Parametric Amplifiers made from SQUIDs arrays. *Physical Review Applied* **11,** 034014. arXiv: 1809.08476 (Mar. 6, 2019).

90. Yaakobi, O., Friedland, L., Macklin, C. & Siddiqi, I. Erratum: Parametric amplification in Josephson junction embedded transmission lines [Phys. Rev. B **87** , 144301 (2013)]. *Physical Review B* **88,** 219904 (Dec. 11, 2013).

91. Yaakobi, O., Friedland, L., Macklin, C. & Siddiqi, I. Parametric amplification in Josephson junction embedded transmission lines. *Physical Review B* **87,** 144301 (Apr. 1, 2013).

Back to contents

92. Yaakobi, O., Friedland, L., Macklin, C. & Siddiqi, I. Parametric amplification in Josephson junction embedded transmission lines. *Physical Review B - Condensed Matter and Materials Physics* **87,** 1–9. arXiv: arXiv:1308.2951v1 (2013).

93. White, T. C. *et al.* Traveling wave parametric amplifier with Josephson junctions using minimal resonator phase matching. *Applied Physics Letters* **106,** 242601 (June 15, 2015).

94. Planat, L. *Resonant and traveling-wave parametric amplification near the quantum limit* PhD thesis ().

95. Houde, M., Govia, L. & Clerk, A. Loss Asymmetries in Quantum Traveling-Wave Parametric Amplifiers. *Physical Review Applied* **12,** 034054 (Sept. 26, 2019).

96. O'Connell, A. D. *et al.* Microwave dielectric loss at single photon energies and millikelvin temperatures. *Applied Physics Letters* **92,** 112903 (Mar. 17, 2008).

97. Renger, M. *et al.* Beyond the standard quantum limit of parametric amplification. *arXiv:2011.00914 [cond-mat, physics:quant-ph].* arXiv: 2011.00914 (Nov. 11, 2020).

98. Fernandez, J. E. A Noise-Temperature Measurement System Using a Cryogenic Attenuator. *HARD LINE* **135,** 1–9.

99. Su-Wei Chang, Aumentado, J., Wei-Ting Wong & Bardin, J. C. *Noise measurement of cryogenic low noise amplifiers using a tunnel-junction shot-noise source* in *2016 IEEE MTT-S International Microwave Symposium (IMS)* 2016 IEEE/MTT-S International Microwave Symposium (IMS) (IEEE, San Francisco, CA, May 2016), 1–4.

100. Lloyd, S. Enhanced Sensitivity of Photodetection via Quantum Illumination. *Science* **321,** 1463–1465 (Sept. 12, 2008).

101. Tan, S.-H. *et al.* Quantum Illumination with Gaussian States. *Physical Review Letters* **101,** 253601 (Dec. 18, 2008).

102. Fasolo, L. *et al.* Josephson Travelling Wave Parametric Amplifiers as Non-Classical Light Source for Microwave Quantum Illumination. arXiv: 2106.00522 (2021).

103. New, G. *Introduction to Nonlinear Optics* (Cambridge University Press, 2011).

104. Flurin, E. The Josephson mixer: a swiss army knife for microwave quantum optics, 251.

Back to contents

105. Adesso, G. & Illuminati, F. Gaussian measures of entanglement versus negativities: Ordering of two-mode Gaussian states. *Physical Review A* **72** (2005).

106. Lang, C. *Quantum Microwave Radiation and its Interference Characterized by Correlation Function Measurements in Circuit Quantum Electrodynamics* PhD thesis (ETH Zurich, 2014), 1689–1699.

107. Chang, S. W., Aumentado, J., Wong, W. T. & Bardin, J. C. Noise measurement of cryogenic low noise amplifiers using a tunnel-junction shot-noise source. *IEEE MTT-S International Microwave Symposium Digest* **2016-Augus** (2016).

108. *Technical data sheet: C20-0R518 Directional Coupler (Stripline)*

109. *Technical data sheet: Coaxial Subminiature Multiport Switches R591722600*

110. Giedke, G., Wolf, M. M., Krüger, O., Werner, R. F. & Cirac, J. I. Entanglement of Formation for Symmetric Gaussian States. *Physical Review Letters* **91** (2003).

111. Boutin, S. *et al.* Effect of Higher-Order Nonlinearities on Amplification and Squeezing in Josephson Parametric Amplifiers. *Phys. Rev. Applied* **8,** 1–22. arXiv: 1708.00020 (2017).

112. Petrescu, A., Royer, B. & Blais, A. *Accurate theory for drive-activated nonlinear processes in the SNAIL parametric amplifier* in. **2021.** Conference Name: APS March Meeting Abstracts ADS Bibcode: 2021APS..MARY32013P (Jan. 1, 2021), Y32.013.

113. Aggarwal, A. MA thesis (Université Grenoble Alpes, 2021).

114. Sathyamoorthy, S. R. *et al.* Quantum Nondemolition Detection of a Propagating Microwave Photon. *Physical Review Letters* **112,** 093601 (Mar. 3, 2014).

115. Dassonneville, R., Assouly, R., Peronnin, T., Rouchon, P. & Huard, B. Number-Resolved Photocounter for Propagating Microwave Mode. *Physical Review Applied* **14,** 044022 (Oct. 14, 2020).

116. Fan, B., Milburn, G. J. & Stace, T. M. Non-absorbing high-efficiency counter for itinerant microwave photons. *Research in Optical Sciences*, 3 (2014).

117. Leppäkangas, J. *et al.* Multiplying and detecting propagating microwave photons using inelastic Cooper-pair tunneling. *Physical Review A* **97,** 013855 (Jan. 31, 2018).

Back to contents

118. Kono, S., Koshino, K., Tabuchi, Y., Noguchi, A. & Nakamura, Y. Quantum non-demolition detection of an itinerant microwave photon. *Nature Physics* **14,** 546–549 (June 2018).

119. Besse, J. C. *et al.* Single-Shot Quantum Nondemolition Detection of Individual Itinerant Microwave Photons. *Physical Review X* **8,** 21003. arXiv: 1711.11569 (2018).

120. Helmer, F., Mariantoni, M., Solano, E. & Marquardt, F. Quantum nondemolition photon detection in circuit QED and the quantum Zeno effect. *Physical Review A* **79,** 052115 (May 20, 2009).

121. Batra, N. & Sheet, G. Understanding Basic Concepts of Topological Insulators Through Su-Schrieffer-Heeger (SSH) Model. *Resonance* **25,** 765–786. arXiv: 1906.08435 (June 2020).

122. Metelmann, A. & Clerk, A. A. Nonreciprocal photon transmission and amplification via reservoir engineering. *Physical Review X* **5.** arXiv: 1502.07274 (2015).

123. Sliwa, K. M. *et al.* Reconfigurable josephson circulator/directional amplifier. *Physical Review X* **5.** arXiv: 1503.00209 (2015).

124. Lecocq, F. *et al.* Nonreciprocal Microwave Signal Processing with a Field-Programmable Josephson Amplifier. *Physical Review Applied* **7,** 1–17. arXiv: 1612.01438 (2017).

125. Ranzani, L. *et al.* Wideband Isolation by Frequency Conversion in a Josephson-Junction Transmission Line. *Physical Review Applied* **8,** 1–7 (2017).

126. Naghiloo, M., Peng, K., Ye, Y., Cunningham, G. & O'Brien, K. P. Broadband Microwave Isolation with Adiabatic Mode Conversion in Coupled Superconducting Transmission Lines. arXiv: 2103.07793 (2021).

127. O'Connell, A. D. *et al.* Microwave dielectric loss at single photon energies and millikelvin temperatures. *Applied Physics Letters* **92,** 112903. arXiv: 0802.2404 (2008).

128. Paik, H. & Osborn, K. D. Reducing quantum-regime dielectric loss of silicon nitride for superconducting quantum circuits. *Applied Physics Letters* **96,** 2008–2011. arXiv: 0908.2948 (2010).

Back to contents

129. Boussaha, F. *et al.* Development of TiN Vacuum-Gap Capacitor Lumped-Element Kinetic Inductance Detectors. *Journal of Low Temperature Physics* **199,** 994–1003 (2020).

130. Al-Tavil, E. MA thesis (Université Grenoble Alpes, 2019).

131. Peng, K. *et al.* Floquet-Mode Traveling-Wave Parametric Amplifiers. *PRX Quantum* **3,** 020306 (Apr. 8, 2022).

132. Planat, L. *Resonant and traveling-wave parametric amplification near the quantum limit* PhD thesis (UGA Grenoble, 2020).

133. Pozar, D. M. *Microwave Engineering* fourth edi (John Wiley & Sons, Inc., 2010).

134. Ranadive, A., Esposito, M., Planat, L. & Roch, N. github: JJ metamaterial simulation. *GitHub.*

Back to contents

Metamaterials are artificially designed materials to exhibit properties not available in natural materials by engineering the constituting elements at sub-wavelength scales, enabling unique interactions of matter with electromagnetic waves or coupling modes of electromagnetic waves. Examples of such novel optics phenomenons include negative index of refraction, cloaking, and super-resolution imaging. The study of superconducting metamaterials operating in the microwave frequency domain has recently generated significant interest in the framework of quantum technologies due to a wide range of direct applications, e.g., exploration of novel quantum optics phenomena, non-destructive quantum sensing, quantum-limited amplification, quantum information processing, and quantum illumination. In contrast to their normal metal and semiconducting counterparts, superconducting metamaterials offer some unique advantages. The most relevant of these for Josephson junction based metamaterials are low losses, flux quantization, and Josephson effects. The Josephson effect in a superconducting loop can also be exploited to exact more control over the nonlinearities of the meta-material.

We present Josephson junction based metamaterials with in-situ tunability of second and third-order (Kerr) nonlinearities. We optimized the Josephson junction composites SNAILs, well-known in the superconducting circuits community, for the specific use case of building blocks for an impedance-matched nonlinear meta-material. In such devices, the strong third-order (Kerr) nonlinearity can be tuned from positive to negative values. To demonstrate the efficacy of this phenomenon, we have shown a use case of the meta-material as a TWPA with a new phase-matching mechanism: reversed Kerr phase matching, which utilizes the sign reversal of the Kerr nonlinearity to correct for the dispersion curvature of such devices arising due to the finite plasma frequency. We also present the generation of entanglement to demonstrate the versatility of these meta-materials and further emphasize their potential in the general framework of nonlinear microwave quantum optics.